ABSTRACT

Title of dissertation: MANIPULATION OF THE QUANTUM
MOTION OF TRAPPED ATOMIC IONS
VIA STIMULATED RAMAN TRANSITIONS

Kenneth Earl Wright II
Doctor of Philosophy, 2017

Dissertation directed by: Professor Christopher Monroe
Department of Physics

Trapped ions have been a staple resource of quantum simulation for the past decade. By taking advantage of the spin motion coupling provided by the Coulomb interaction, trapped ions have been used to study quantum phase transitions of highly frustrated spins, many body localization, as well as discrete time crystals. However, all of these simulations involve decoupling the ion motion from spin at the end of the experimental procedure. Here we present progress towards driving bosonic interference between occupied phonon modes.

This thesis details a tool box for manipulating the motional states of a chain of trapped ions. Taking advantage of spin motion interaction of tightly trapped chains of $^{171}\mathrm{Yb}^{+}$ ions with two photon Raman transition, we show how to prepare a specific number state of a given normal mode of motion. This is achieved without traditional individual addressing but instead by using composite pulse sequences and ion transport. This involves a stage of quantum state distillation, and we also show preservation of phonon and spin coherence after this distillation step. This

Fock state preparation sets the stage to observe bosonic interference of different phonon modes.

We use stimulated Raman transitions to create a parametric drive; this drive will couple different normal modes of motion. To observe the bosonic nature of the phonons, we preform a Hong-Ou-Mandel (HOM) interference experiment on two singly occupied normal modes. We use the same spin motion coupling to read out the spin states of individual ions as a witness for this interaction. We also describe a process to use stimulated rapid adiabatic passage (STIRAP) to read out normal mode occupation. The toolbox presented here will be useful for future experiments towards boson sampling using trapped ions.

MANIPULATION OF THE QUANTUM MOTION OF TRAPPED ATOMIC IONS VIA STIMULATED RAMAN TRANSITIONS

by

Kenneth Earl Wright II

Dissertation submitted to the Faculty of the Graduate School of the
University of Maryland, College Park in partial fulfillment
of the requirements for the degree of
Doctor of Philosophy
2017

Advisory Committee:
Professor Chris Monroe, Chair/Advisor
Professor Gretchen Campbell
Professor Andrew Childs
Professor Luis Orozco
Professor James Williams

Dedication

to

Monica Gutierrez Galan,

Sally Morris, James Morris, and Kenneth Wright Sr

Table of Contents

Dedication iv

Acknowledgments iv

List of Figures v

1 Introduction 1

2 Ion Trapping 5
  2.1 Paul Traps 5
    2.1.1 Ion trap theory 6
    2.1.2 Macro-fabricated traps 10
    2.1.3 Micro-fabricated traps 12
  2.2 Normal Modes 16
  2.3 Yb Ions 19
    2.3.1 Ionization 20
    2.3.2 Doppler Cooling 22
    2.3.3 Spin Sate Initialization and Readout 26

3 Experimental Apparatus 29
  3.1 Vacuum Chamber 29
    3.1.1 External Chamber Components 30
    3.1.2 Internal Chamber Components 32
  3.2 Optics 35
    3.2.1 Cooling and Trapping Beam Paths 35
    3.2.2 Imaging system 42
    3.2.3 Raman Beam Path 45
  3.3 Control Electronics 49
    3.3.1 Timing Control 49
    3.3.2 Trapping Voltage Control 51
      3.3.2.1 DC Voltages 52
      3.3.2.2 RF Voltage 54
    3.3.3 Stabilization 56

3.4 Ball Grid Array Trap 58

4 Coherent Operations 62
4.1 Raman Interaction 62
4.1.1 Pulsed Raman Interaction 71
4.1.2 Yb Ion Coupling 72
4.1.3 Raman Coupling with Normal Modes 76
4.1.4 STIRAP 82

5 Phonon Toolbox 86
5.1 Sideband Cooling 87
5.1.1 Heating Rates 89
5.2 Individual Addressing 91
5.2.1 Transport 92
5.2.2 Composite pulse sequences 94
5.3 Phonon State Initialization and Distillation 100
5.4 Readout 108

6 Phonon Interference 111
6.1 Hong-Ou-Mandel Photon Example 111
6.2 Hong-Ou-Mandel Phonon Example 118
6.2.1 Results 122

7 Outlook 130
7.1 Future Improvements 130

A Laser locking 133
A.1 Wavemeter Locking 133
A.2 Locking via discharge cells 135
A.3 Transfer Cavity Locking 138

B Boson Sampling 141

Bibliography 144

List of Figures

2.1 Florescence image of eight ion image . . . 6
2.2 Linear Paul trap . . . 7
2.3 Linear Paul trap quadrapole . . . 8
2.4 Planar trap . . . 12
2.5 Surface trap pseudopotential . . . 13
2.6 Surface trap confinement in three dimensions . . . 14
2.7 Equally spaced four ion image . . . 15
2.8 Three ion normal modes . . . 19
2.9 Energy levels $^{171}\mathrm{Yb}^{+}$ . . . 21
2.10 Energy levels for neutral Yb . . . 22
2.11 Doppler cooling scheme . . . 23
2.12 Detection scheme . . . 26
2.13 Optical pumping scheme . . . 27
2.14 Optical pumping time scan . . . 28

3.1 Vacuum chamber . . . 31
3.2 Oven assembly . . . 34
3.3 399 nm optics layout . . . 36
3.4 935 nm optics layout . . . 37
3.5 369 nm optics layout . . . 38
3.6 Doppler cooling scheme, re-print . . . 39
3.7 $S_{1/2} \rightarrow P_{1/2}$ resonance curve . . . 40
3.8 Optical pumping scheme, re-print . . . 41
3.9 Atomic energy levels used for detecting the spin state of the ion . . . 42
3.10 Histograms of bright and dark ions . . . 43
3.11 Optical layout of the ion imaging system . . . 43
3.12 Spot diagrams for ions at the image place . . . 44
3.13 355 nm optics layout . . . 46
3.14 Chamber optics layout . . . 47
3.15 Raman laser layout at the trap . . . 48
3.16 Control architecture . . . 49
3.17 Butterworth filter schematic . . . 52

3.18 Butterworth filter transfer function 53
3.19 Helical resonator cross section 55
3.20 Resonator lumped element model 56
3.21 Repetition rate lock 58
3.22 BGA trap schematic 59
3.23 Spherical octagon 60

4.1 Clebsch Gordon 74
4.2 Carrier rabi flopping 77
4.3 STIRAP theory 84

5.1 Sideband asymmetry, all three modes 88
5.2 Heating rate on mode b_0 90
5.3 Sideband asymmetry after transport 93
5.4 Population transfer for composite pulse sequences 94
5.5 Spin dynamics in a field gradient with composite pulse sequences . . 95
5.6 Spin dynamics with a single pulse 96
5.7 Single pulse 97
5.8 SK1 pulse 97
5.9 Spin dynamics with an SK1 pulse sequence 98
5.10 N2 pulse 98
5.11 Spin dynamics with an N2 pulse sequence 99
5.12 Phonon preparation theory 100
5.13 Phonon preparation experiment 102
5.14 Red sideband on mode b_0 theory after preparation 103
5.15 Red sideband on mode b_0 after preparation 105
5.16 Red sideband on mode b_2 theory after preparation 106
5.17 Red sideband on mode b_2 after preparation 107
5.18 STIRAP readout scheme 109

6.1 Optical Hong-Ou-Mandel experiment 112
6.2 Phonon HOM theoretical spin dynamics 122
6.3 Phonon HOM theoretical phonon dynamics 123
6.4 Experimental HOM results 125
6.5 Blue sideband OVAD 127
6.6 Blue sideband OVAD after improvements 128

A.1 Discharge cell optics layout 135
A.2 Transfer cavity optics layout 138

Chapter 1: Introduction

The last century of physics has been one of great advancement in the understanding of macroscopic and microscopic processes. The advent of quantum theory has lead to a deep understanding of physical systems that range in scale from the inner workings of atoms to the inner workings of suns; modern society is full of advancements created through better understanding of the effects of quantum mechanics. For this alone, the importance of current quantum theory cannot be overstated.

However, to study highly complicated many body quantum dynamics that underlay important and practical applications of quantum mechanics, adequate tools still remain elusive [1]. For example the natural catalysis that chemically fixes nitrogen, is accomplished by simple bacteria and is one that, as a society, we spend a vast amount of energy resources replicating. This process in integral to creating the fertilizers necessary to grow food for the ever increasing world population. A better understanding of this process might lead to a much more efficient way to feed ourselves. This specific example is one of many that highlight the necessity for a better understanding and implementation of tools that can be used to understand complex quantum systems.

The idea of using a well understood, controlled quantum system to study a more complicated intractable quantum system goes back to Feynman [2]. To store the full quantum mechanical description for a large many body state classically would require a system to store 2^N complex amplitudes; where a quantum system would only need N well controlled quantum resources. In response to this idea, a vast field of physics has developed to try and create and manipulate quantum resources.

Trapped atomic ions have for some time been a workhorse of experimental quantum information science and quantum simulation. The reason that atomic resources are so attractive for these applications is that all ions are in principle created equal, therefore ions make for very clean quantum systems which can be used as the basis for quantum computation or quantum simulation. The resources almost exclusively used in trapped ion quantum systems are the internal degrees of freedom of the ion's electronic structure. However, this is not the only quantum resource available to us when trapping ions. The external degrees of freedom, if they can be cleanly initialized and manipulated, represent an interesting resource for quantum simulation and remain widely unstudied in the community of ion trappers.

In this thesis, I will outline a set of tools we have developed with our trapped ion system to better manipulate and initialize these external degrees of freedom. This is done with an eye towards performing a proof of principle demonstration of bosonic interference using the phonon excitations associated with a chain of trapped ions. The thesis is broken out in seven chapters,

- Chapter 2: The basic theory of RF Paul traps; differences between macro-fabricated and micro-fabricated traps. The normal modes of motion of a trapped ion chain. It will also cover the incoherent atom-light interactions which govern ionization, spin state preparation, spin readout, and Doppler cooling.

- Chapter 3: Experimental apparatus including the vacuum system, the layout of all of the optics from lasers to ions, as well as the optics used to image ion florescence. The control loops that are used to lock various frequencies and amplitudes throughout the lab are discussed, as well as a description of the control electronics used to implement experimental sequences and collect information about ion states.

- Chapter 4: Atom light interactions which we implement to drive coherent operations. Including a toy description of Raman coupling via an excited state, generalization of this model to $^{171}\mathrm{Yb}^{+}$ and mutli-ion chains. A description of an adiabatic passage via the same laser fields is also discussed.

- Chapter 5: Description of the experimental procedure that we implement to initialize and readout phonons, including data on our ability to prepare Fock states of motion through composite pulse sequences and shuttling, as well as our ability to distill these states through measurement.

- Chapter 6 : An example of photon interference and the observed Hong-Ou-Mandel dip is discussed. Drawing an analogy with photonic experiments I describe how we intend to drive beam splitter-like interactions with the phonons of our trapped ion chain.

- Chapter 7: Highlights some of the planned improvements, explaining how I think these renovations of the experiment will help us reach our experimental goals.

Chapter 2: Ion Trapping

2.1 Paul Traps

For the last two decades or more, ions have been used as cutting edge tools in the development of quantum information processors as well as quantum simulators [3–9]. One reason why ions are such a useful tool is that once confined, the atoms are generally confined for substantial periods of time, this can be as much as several days. This allows for repeated interrogation of the same ions. Another reason is that each ion is identical, and unlike many other quantum systems being considered as candidate qubits or quantum simulators, such as quantum dots or supper conducting qubits, there is very little calibration of the qubit states themselves between different experimental implementations[1].

There are two ways in which researchers trap atomic ions, Penning traps and Paul traps [10, 11]. Penning traps rely on the cyclotron motion of charged particles in a strong magnetic field to confine ions radially. Alternatively, Paul traps makes use of only electric fields to confine atoms. All the work described in this thesis will make use of Paul traps, specifically micro-fabricated linear Paul traps. I will spend

---

[1] The hyperfine splitting between the $^{171}\mathrm{Yb}^{+}$ clock states is the same for every laboratory trapping Yb.

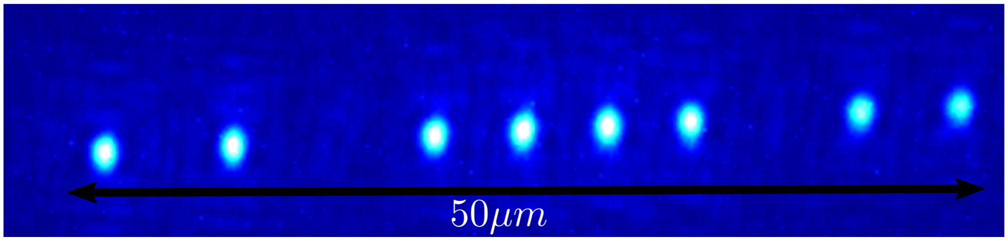

Figure 2.1: Eight ions trapped in the apparatus discussed in this thesis, the dark spaces are from ions which have been pumped to long lived dark states. These states are efficiently re-pumped with the Raman laser we employ and in general are not an issue for our experiments. This chain was constructed in a deterministic fashion moving ions between zones in a micro-fabricated trap.

the next sections on the theory background of the Paul trap, then elaborate on the distinctions between macro-fabricated and micro-fabricated traps.

2.1.1 Ion trap theory

One might naively assume that by appropriately shaping direct current (DC) potentials one would be able to create a potential minima in space that a charged ion would find confining. Unfortunately, this of course violates Earnshaw's theorem.

$$\boldsymbol{\nabla} \cdot \boldsymbol{E} = 0 \tag{2.1}$$

Which is to say that static electric fields will only have maxima or minima at locations of charge density and that in free space there can be no local maxima or minima of the field. The way ion trappers get around this is by applying oscillating electric fields. Instantaneously, these fields do not violate Earnshaw's theorem, but if the frequency of oscillation can be made large enough, such that an ion experiences a time average minima of the field, it will be trapped.

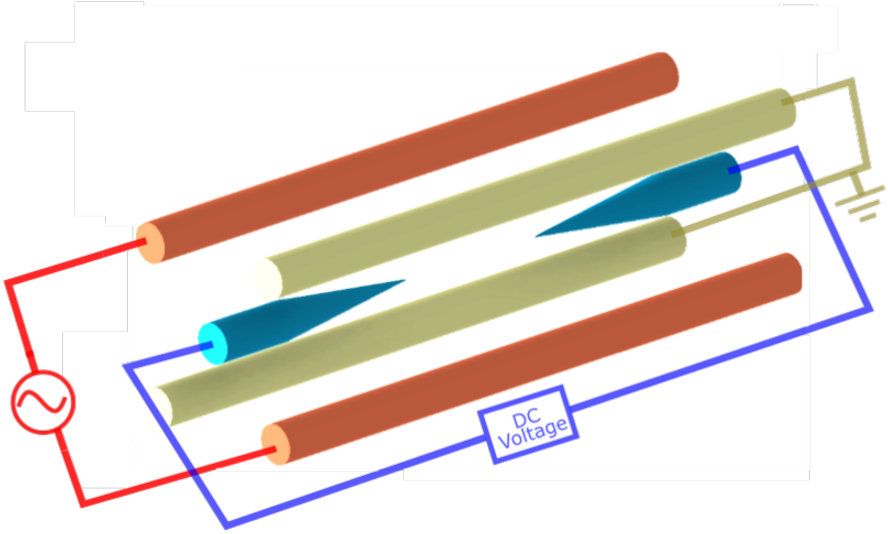

Figure 2.2: The copper colored rods here carry the RF potential, the brass colored rods act as grounds for the RF voltage and the needles in blue, which act as “end-caps”, supply a large DC field in the axial direction of the trap. With these electrodes one can achieve three dimensional confinement.

The way this is accomplished is by creating a saddle point potential between four electrodes which have spatial extent along an axial direction, $\hat{z}$. Two of these electrodes carry radio frequency power (RF) and are diagonal from each other, the other two electrodes are grounded. This sets up an oscillating qudrapole field at the center of these electrodes along the axis $\hat{z}$ of the trap. The radial escape route of an ion sitting in the center of this quadrupole is rotating as the RF electrodes oscillate between positive and negative cycles. An ion experiences a radial saddle point potential of the form [3],

$$\Phi_{x,y} = \frac{V_{RF}}{2}\cos(\Omega_{RF}t)\left(1 + \frac{x^2 - y^2}{R^2}\right) \tag{2.2}$$

Where R is the characteristic distance of the trap, for RF traps this is the

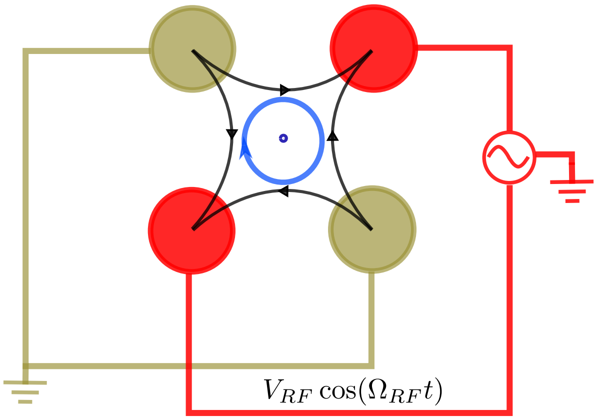

Figure 2.3: By applying oscillating RF fields between diagonal rods with grounded rods adjacent to these rods sets up an oscillating quadrapole at a point equi-distant from all the rods along $\hat{z}$. If this quadrapole oscillates fast enough trapped charges will see harmonic confinement radially from this point.

distance to the RF rail, V_{RF} and Ω_{RF} are the voltage and driving frequency of the RF. To confine ions along the $\hat{z}$ axis, so called "end-cap" electrodes are placed at the ends of the four electrodes forming the quadrapole field. By applying voltages to these electrodes one can create harmonic confinement along the axial direction of the trap. The potential takes the form,

$$\Phi_z = U_0 \left(z^2 - \frac{x^2 + y^2}{2} \right) \tag{2.3}$$

We can verify that by looking at the total potential Earnshaw's theorem is still satisfied. The total potential is give by,

$$\Phi_{total} = \frac{V_{RF}}{2} \cos(\Omega_{RF}t) \left(1 + \frac{x^2 - y^2}{R^2} \right) + U_0 \left(z^2 - \frac{x^2 + y^2}{2} \right) \tag{2.4}$$

This gives an electric field with the following form which we can evaluate to verify that Earnshaw's theorem is still satisfied with the total potential,

$$\boldsymbol{E} = -\boldsymbol{\nabla}\Phi_{total} \tag{2.5}$$

$$= V_{RF}\cos(\Omega_{RF}t)\left(\frac{y\hat{y} - x\hat{x}}{R^2}\right) + 2U_0\left(\frac{x\hat{x} + y\hat{y}}{2} - z\hat{z}\right) \tag{2.6}$$

$$\boldsymbol{\nabla}\cdot\boldsymbol{E} = \left(\frac{V_{RF}}{2} - \frac{V_{RF}}{2}\right)\cos(\Omega_{RF}t) + 2\left(\frac{U_0 + U_0}{2} - U_0\right) \tag{2.7}$$

$$= 0 \tag{2.8}$$

From this equation for the electric field we can determine the force, $\boldsymbol{F} = q\boldsymbol{E}$, and the equations of motion, $\ddot{r}_i - \frac{\boldsymbol{F}_i}{m} = 0$,

$$\ddot{x} + \left[\frac{eV_{RF}}{mR^2}\cos(\Omega_{RF}t) + \frac{-eU_0}{m}\right]x = 0 \tag{2.9}$$

$$\ddot{y} + \left[\frac{-eV_{RF}}{mR^2}\cos(\Omega_{RF}t) + \frac{-eU_0}{m}\right]y = 0 \tag{2.10}$$

$$\ddot{z} + \left[\frac{2eU_0}{m}\right]z = 0 \tag{2.11}$$

Notice that all of these equations can be cast in the form of a Mathieu equations, $\ddot{r}_i + \frac{\Omega^2}{4}\left[a_i + 2q_i\cos(\omega t)\right]r_i = 0$, where the values of the unitless parameters a_i and q_i define regions of trap stability. We can solve the Mathieu equations, and for our purposes by keeping a_i and $q_i \ll 1$, we can achieve a stable trap. The radial solutions to the Mathieu equations take the following for.

$$r_i = A_i \cos(\omega_i t + \phi_i)\left[1 + \frac{q_i}{2}\cos(\Omega_{RF} t) + \frac{q_i^2}{32}\cos(2\Omega_{RF} t)\right] \tag{2.12}$$

$$+ A_i \beta_i \frac{q_i}{2}\sin(\omega_i t + \phi_i)\sin(\Omega_{RF} t) \tag{2.13}$$

Where A_i depends on initial conditions and $\beta_i \approx (a_i + \frac{q_i^2}{2})^{1/2}$, β_i can be related to the secular frequencies ω_i by the relation $\omega_i = \beta_i \frac{\Omega_{RF}}{2}$. By defining these unitless parameters in terms of the above trap parameters, we can also relate them to the secular frequencies of the trap.

$$a_x = \frac{-4eU_0}{m\Omega_{RF}^2} \quad q_x = \frac{2eV_{RF}}{mR^2\Omega_{RF}^2} \quad \omega_x = \frac{eV_{RF}}{\sqrt{2}mR^2\Omega_{RF}} \tag{2.14}$$

$$a_y = \frac{-4eU_0}{m\Omega_{RF}^2} \quad q_y = \frac{-2eV_{RF}}{mR^2\Omega_{RF}^2} \quad \omega_y = \frac{eV_{RF}}{\sqrt{2}mR^2\Omega_{RF}} \tag{2.15}$$

$$a_z = \frac{8eU_0}{m\Omega_{RF}^2} \quad q_z = 0 \quad \omega_z = \sqrt{\frac{2eU_0}{m}} \tag{2.16}$$

By controlling these parameters, we can affect the ion spacing and frequencies of the normal modes of motion. It is important to directly fix some of these parameters because of the direct impact on mode frequency. The next subsections will discuss some of the differences between macro- and micro-fabricated ion traps.

2.1.2 Macro-fabricated traps

The more traditional traps which are still the main workhorses of most ion trapping laboratories are what are known as macro-traps. In the ion trapping laboratories at the University of Maryland we, almost exclusively, use blade traps [12–14]; where the four rods of the canonical Paul trap are formed by four thin segmented blades. Two of these blades carry RF voltage to the trap, the other two have DC potentials applied to their segments. These electrodes act as "end-caps" and this segmentation allows for some shuttling of ions. Although, these procedures are quite limited due to the small amount of segmentation. When they have segmented DC electrodes, macro-traps tend to have only a few trapping zones. These traps usually have dimensions on the scale of inches and are generally constructed by hand in a laboratory setting. The ion to trap electrode distance can be quite small, on the order of 100 μm. The greatest benefit of traps like this is that they have extremely large well depths. The typical macro-trap can have well depths of approximately 10 eV, which corresponds to a temperature of $1 \cdot 10^5$ K, these traps have been known to hold ions for weeks at a time.

The primary disadvantage of traps like this is that they are not scalable. If one really wanted to build a large scale quantum information processor, they would need thousands of ions or ion chains in separate traps coupled together [15, 16]. Holding progressively longer chains of ions in a single trap will eventually be limited by vacuum and is therefore inherently unscalable. Coupling separate traps together has promise, however if all of these traps need to be built by hand, where each trap will be different and those differences need to be calibrated away, this also seems like a no-go situation. That begin said, all of the most cutting edge work on high fidelity gates [17], quantum simulation [18], or large entangled states [7] are still performed on these traps.

2.1.3 Micro-fabricated traps

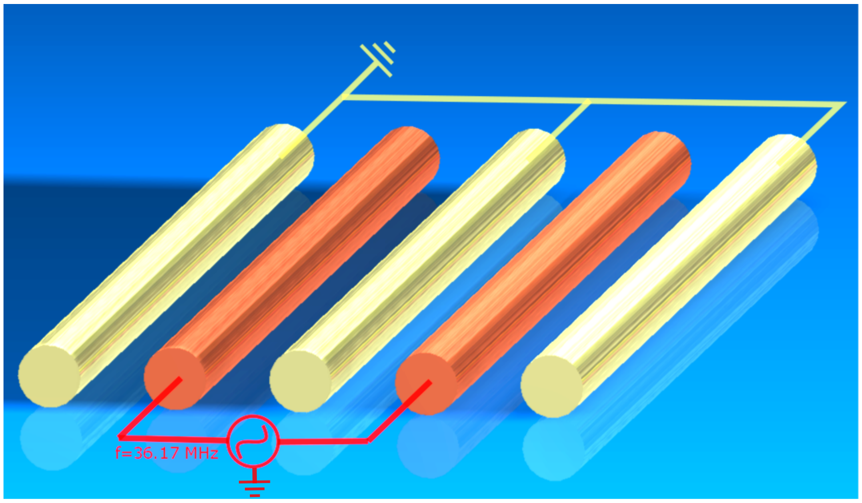

Figure 2.4: By laying out the rods of the traditional Paul trap one can make a trap where all electrodes are in one plane and the oscillating quadrapole potential lies above the plane.

In contrast to the macro-fabricated traps of the previous section, micro-fabricated traps were designed with the idea of scalability specifically in mind. For our purposes, a micro-fabricated trap will be any trap which was produced in a CMOS like foundry. In particular, this experiment has only used traps which consist of etched metal features on silicon resulting in a planar geometry[2]. The general four wire geometry we described earlier in this chapter for larger ion traps still applies to micro-fabricated traps, however the geometry of electrodes is clearly modified. Consider the same four rods as before but instead lay them out in a single plane, insert

---

[2] That is not to say that more symmetric three dimensional geometries are not considered micro-fabricated [19], only that they differ so slightly from the macro-fabricated traps that the theory of operation is essentially the same [20].

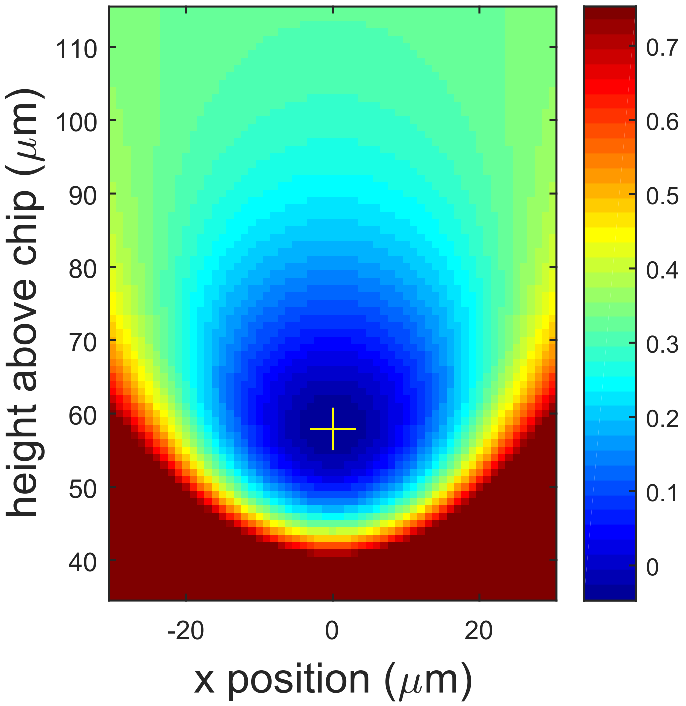

Figure 2.5: Simulation of the pseudo-potential above the micro-fabricated trap we currently are using, the color scale is in meV This null is found approximately 60 μm above the trap surface and is 60 meV deep. The orientation of the cross hairs indicates the direction of the RF principal axes.

a DC electrode between the two RF electrodes, and assume that at infinity above the surface there is a grounded plane. There will be a quadrapole potential, just as before, above this plane [21]. If we flatten out these electrodes we have a standard planar ion trap. The pseudo-potential tube is now located above the surface and extends along the electrodes. Any or all of the DC electrodes can be segmented to apply harmonic confinement along the axis.

The obvious advantage of traps formed in this way is that it allows for very small structures to be built into the trapping architecture. The electrodes themselves can take on rather exotic shapes, and although this must be taken into account when modeling the trap, there have been quite a range of novel architectures fabri-

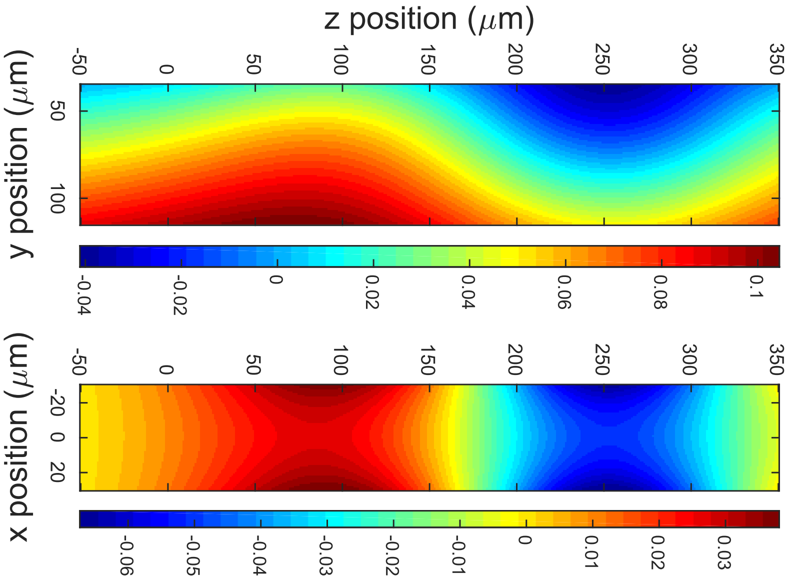

Figure 2.6: Simulations of our trapping structure showing the transverse confinement as a function of the axial position along the trap, color scale in meV. By shifting voltages on the DC electrodes this potential can be moved anywhere along the $\hat{z}$ axis.

cated into micro-fabricated ion traps. This includes slots to have laser beams pass through the trapping structure [22], mirrors both concave [23,24] and diffractive [25], junctions to send ions along different arms of crossed linear traps [26,27], as well as microwave wave guides to couple atoms to near-field microwaves [28]. The discussion of the particular trap used for these experiments is left to the next chapter. In particular, having many electrodes which are small in extent allows for fine control of the DC potential. This gives us the flexibility to adjust ion spacing as well as modify the harmonicity of the DC potential. This allows us to make ions equally spaced, or spaced widely apart to help in imaging individual ions. In general this is more difficult for macro-fabricated traps where there are a limited number of electrodes and they are far away, this in particular makes creating anharmonic DC potentials more challenging.

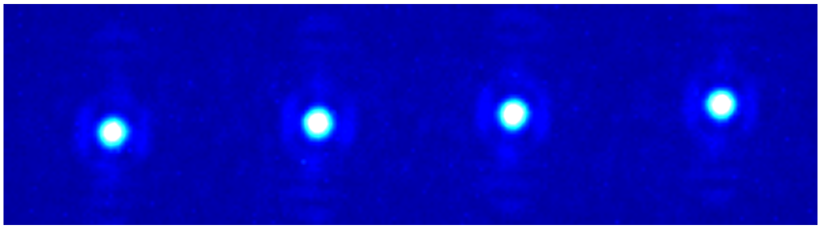

Figure 2.7: Florescence image of four equally spaced ions, achieved by adjusting the proportion of harmonic and anharmonic terms in the axial potential. The four ions are mostly imaged onto 4 circular spots onto the camera, however the residual light around these spots highlights imperfections in the imaging system.

The biggest problem for micro-fabricated traps also is that the trapping structures are so small, which limits the transverse confinement and the well depth that can be achieved, and increases the heating rate. Because the structures that form the RF electrodes are separated from adjacent ground planes by approximately 4 μm, at high enough voltage the RF will arc to ground. This process is violent and can destroy the RF electrode. This puts a hard limit on the maximum amplitude of the RF voltage that can be applied, which is directly proportional to transverse trap frequency.

The RF potential of micro-fabricated traps is generally not as symmetric as macro-fabricated traps, because of this it is harder to have a strong quadrapole field. The strength of the field can be thought of as the depth of the radial confinement. Generally these traps have well depths of $<$ 100 meV, for comparison that corresponds to a temperature of 10^3 K. This means that ions routinely can be boiled out of the trap due to collisions or general heating. The lifetime of chains in micro-fabricated traps rarely exceeds days as opposed to weeks in the their macro-fabricated counterparts.

The heating of ions is made especially worse in micro-traps because of the so called “anomalous heating rate”, which has been found to scale approximately as $1/\mathrm{R}^4$ [29], where R is the distance away from the nearest trapping surface[3]. With electrodes so close to the ions this problem has limited the acceptance of micro-fabricated traps in the community up until fairly recently.

2.2 Normal Modes

The external quantum degrees of freedom we are trying to initialize and manipulate are the excitations of the normal modes of motion of the ions. In the low excitation limit, we can think of these excitations as bosonic particles known as phonons. This thesis will describe the progress we have made in controlling the number states of these phonons. It is therefore necessary to discuss how these normal modes of motion arise in our physical system. In the previous section we derived harmonic confinement in all three dimensions resulting from voltages applied to electrodes. To determine the collective modes of motion of the ion chain we should balance this restoring potential with the Coulomb repulsion between ions. Let us consider the full Hamiltonian for an arbitrary number of ions [30]

$$\begin{aligned} H &= K + V \qquad (2.17) \\ &= \sum_i^N \sum_j^3 \frac{p_{i,j}^2}{2m} + \frac{1}{2} m \omega_{i,j}^2 q_{i,j}^2 + \sum_{i,k} \frac{e^2}{4\pi\epsilon_0} \frac{1}{d_{i,k}} \qquad (2.18) \end{aligned}$$

---

[3] To be clear this distance can be quite similar to macro-fabricated traps, however the well depth is so much lower that this heating rate can adversely effect ion lifetimes.

Where $q_{i,j}$ is the canonical position not the equilibrium position. The sum over j is a sum over the different trapping directions, i and k are sums over the ions, and $d_{i,k}$ is the distance between ions i and k. We will assume here that $\omega_{\{x,y\}} \gg \omega_z$; this ensures that ion equilibrium positions will lie in a line along the $\hat{z}$ axis of the trap. We need to calculate $\left[\frac{\partial V}{\partial q_{z,i}}\right]_{q^0_{z,i}} = 0$ to determine the equilibrium positions of the ions along this line.

$$\begin{aligned}
0 &= m\omega_z^2 z_i - \sum_{k=1}^{i-1} \frac{e^2}{4\pi\epsilon_0} \frac{1}{|z_i - z_k|^2} + \sum_{k=i+1}^{N} \frac{e^2}{4\pi\epsilon_0} \frac{1}{|z_i - z_k|^2} && (2.19) \\
&= z_i + \frac{e^2}{4\pi\epsilon_0 m\omega_z^2} \left(\sum_{k=i+1}^{N} \frac{1}{|z_i - z_k|^2} - \sum_{k=1}^{i-1} \frac{1}{|z_i - z_k|^2} \right) && (2.20) \\
&= u_i d_0 + \frac{e^2}{4\pi\epsilon_0 m\omega_z^2} \frac{1}{d_0^2} \left(\sum_{k=i+1}^{N} \frac{1}{|u_i - u_k|^2} - \sum_{k=1}^{i-1} \frac{1}{|u_i - u_k|^2} \right) && (2.21) \\
&= u_i + \sum_{k=i+1}^{N} \frac{1}{|u_i - u_k|^2} - \sum_{k=1}^{i-1} \frac{1}{|u_i - u_k|^2} && (2.22)
\end{aligned}$$

This equation can be numerically evaluated for any number of ions to determine their equilibrium positions along the axial trapping direction. We define the unitless length $u_i = \frac{z_i}{d_0}$ with the characteristic distance between ions, $d_0 = \left(\frac{e^2}{4\pi\epsilon_0 m\omega_z^2}\right)^{\frac{1}{3}}$. If we expand the potential to second order in a Taylor expansion about these equilibrium positions, in any direction, we can calculate the normal modes of motion in that direction. More formally, we write the Lagrangian,

$$\begin{aligned} \mathcal{L} &= K - U \qquad (2.23) \\ &= \sum_{i}^{N} \frac{1}{2} m \dot{\tilde{q}}_{i,j}^{2} - \sum_{i,k}^{N} \tilde{q}_{i,j} \tilde{q}_{k,j} \left[\frac{\partial^2 V}{\partial q_{i,j} \partial q_{i,k}} \right]_{\{\tilde{q}_{i,j} \tilde{q}_{k,j}\}=0} \qquad (2.24) \end{aligned}$$

where once again i and k are sums over ions and j is an index representing the direction of the motion. The $\tilde{q}_{i,j}$ are small amplitudes of motion about the ion equilibrium positions, we evaluate the second partial derivative, $\frac{\partial^2 V}{\partial q_{i,j} \partial q_{i,k}}$, where these terms are zero. If we define a matrix $A_{i,k}$ that describes the collective coupling of the ions

$$\mathcal{L} = \sum_{i}^{N} \frac{1}{2} m \dot{\tilde{q}}_{i,j}^{2} - \omega_j^2 \sum_{i,k}^{N} A_{i,k} \tilde{q}_{i,j} \tilde{q}_{k,j} \tag{2.25}$$

and has matrix elements of the form,

$$A_{i,k}^{\{j\}} = \begin{cases} \left(\frac{\omega_j}{\omega_z}\right)^2 + \sum_{l=1, l \neq k}^{N} \frac{1}{|u_k - u_l|^3} & \text{if } i = k \\ \frac{1}{|u_k - u_i|^3} & \text{if } i \neq k \text{ and } j \in x, y \\ \frac{-2}{|u_k - u_i|^3} & \text{if } i \neq k \text{ and } j \in z \end{cases} \tag{2.26}$$

We can solve for the eigenvalues of this matrix to determine the normal mode frequencies, and we can solve for the eigenvectors of the matrix to determine the relative amplitudes of normal mode motion at a given ion. In general this eigensystem must be solved numerically. For a system of three ions, which will be presented extensively later in this work, the transverse eigenvectors are found to be,

$$\boldsymbol{b}_0 = \begin{pmatrix} 1 \\ 1 \\ 1 \end{pmatrix} \quad \boldsymbol{b}_1 = \begin{pmatrix} 1 \\ 0 \\ -1 \end{pmatrix} \quad \boldsymbol{b}_2 = \begin{pmatrix} -1 \\ 2 \\ -1 \end{pmatrix} \tag{2.27}$$

We will see the relative Rabi rates will vary based on the relative amplitudes of motion when we couple the spin states of each ion in a three ion chain to these various modes of motion.

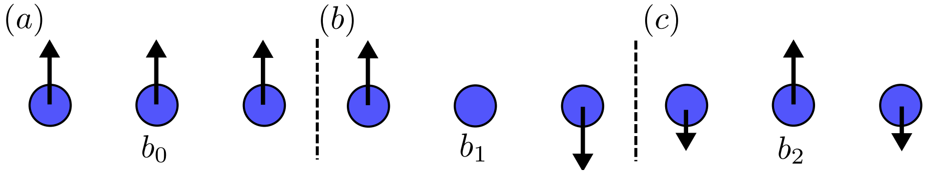

Figure 2.8: Relative amplitudes of motion of each normal mode in a three ion chain based on Eq 2.25.

2.3 Yb Ions

Choosing which ion to trap is a challenging selection, and depends highly on the type of physics to explore. In the case of our experiment, the choice of Yb was natural because of its internal structure. Ionization can be achieved through a two photon process involving two commercially available diode lasers, 399 nm and 369 nm. There is a nearly closed-cycle cooling transition on one of the same lines used to ionize. To optically pump the ion spin state into an $|F = 0, m_F = 0\rangle$ qubit state of a clock transition between long lived, magnetic field insensitive hyperfine ground states we can use the same light we use for cooling, at 369 nm. The leak in the closed cooling cycle is readily plugged with an infrared diode laser at 935 nm. These three laser constitute all the necessary light for the incoherent interrogation of $^{171}\mathrm{Yb}^{+}$. With these lasers we can cool, optically pump, and readout the ion spin state [31].

The coherent manipulation of the clock transition can be achieved in two ways, with direct microwave fields at 12.64 GHz or with a 355 nm pulsed laser. The later is routinely used in an industrial setting and is nearly turn-key. One of the only downsides to Yb is that its large mass means that transverse mode frequencies are reduced for the same RF drive frequency and voltage. This problem is pronounced in a micro-fabricated trap setting where the RF voltage is severely limited due to the size of the trapping structures. However, this disadvantage is far outweighed by the advantages provided by the internal structure of $^{171}\mathrm{Yb}^{+}$. It is routinely shown that driving coherent spin flips with Raman transitions between clock states can maintain coherence times of up to a large fraction of a minute with very minimal effort. The longest coherence times achieved between these levels are measured to be approximately 10 minutes [32]. Because this process is dependent on the beatnote between two beams we only need to care about the microwave coherence of the beatnote, at 12.64 GHz, which can be much easier to maintain than optical coherence, in the THz regime.

2.3.1 Ionization

Atoms leaving the atomic source are generally still neutral, but for the the RF quadrapole to trap them they must first carry some intrinsic charge. This can be achieved by a handful of methods; bombardment with electrons from an electron

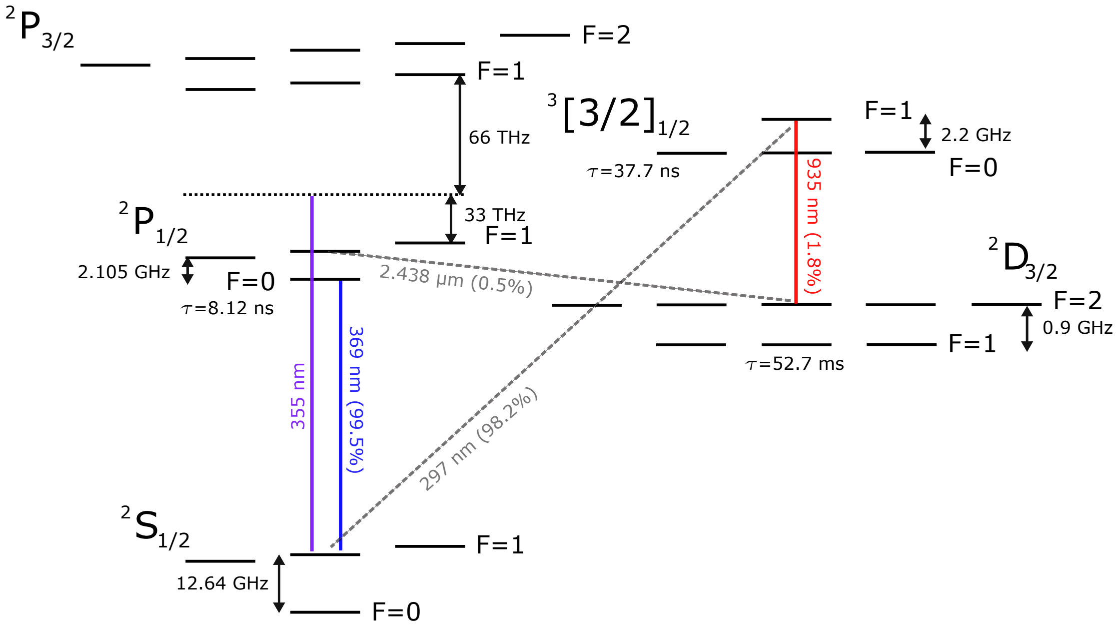

Figure 2.9: Energy levels of the internal structure of ^{171}Yb$^+$. This diagram also gives branching ratios and lifetimes for the various excited states.

gun, charge exchange from an already trapped ion, or through photo-ionization. Photo-ionization is the cleanest of these methods as it does not require electrons thrown at the trapping structure or an already trapped ion obtained through some unknown process. It also allows for isotope selectivity by making use of the isotope shifts in the photo-ionization resonances.

In Yb this ionization is particularly easy. There exists an S to P transition in the neutral atom at 399 nm, at which point the 369 nm laser which will be used for Doppler cooling can excite the P state to the continuum [33]. In our system we take care to align the 399 nm laser as perpendicular as possible to the atomic flux to minimize Doppler broadening effects and maintain the highest degree of isotope selectivity. This allows us to determine which atoms are ionized by tuning the frequency of the 399 nm laser [34]. This is important when trying to load chains,

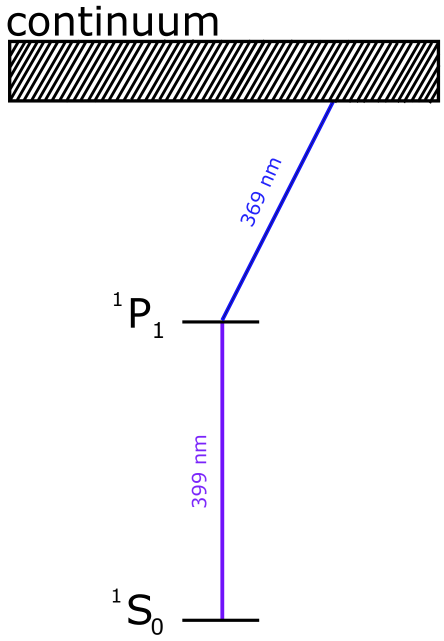

Figure 2.10: Energy levels relevant for ionization of neutral Yb.

because laser cooled ions of one isotope can sympathetically cool ions of a different isotope, therefore if all isotopes are being ionized, pollutant ions can be trapped along with the desired ^{171}Yb$^+$ ions we will use for our experiments. Although this could be used as a resource, if the loading of other ions is not controllable this can be problematic; for example the frequencies and eigenvectors of the normal modes will all change because there would be unequal masses in the chain.

2.3.2 Doppler Cooling

Atoms entering the trapping region from the atomic source have a high velocity, comparable to or greater than the trap depth. When ions are in such high orbits of the trap, collisions with background gasses can cause the ions to undergo heating from the RF drive. We therefore need to cool the ions down closer to the ground state of the trap for them to remain in the trap. This is done by Doppler cooling the ions on the nearly closed-cycle $S_{1/2}$ to $P_{1/2}$ transition.

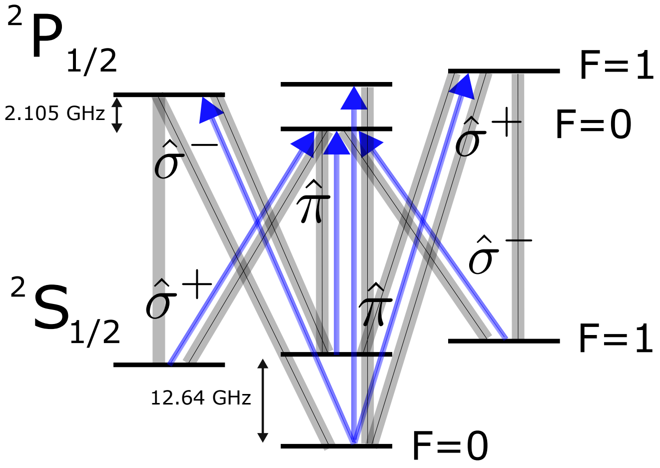

Figure 2.11: To scatter as many photons as possible we send in light with all polarization components and apply sidebands to the 369 nm light to bridge the ground and excited state hyperfine splitting. The blue arrows represent the states connected via dipole allowed transitions driven by laser light. The grey bars represent the possible spontaneous decay paths from those excited states.

The mechanism for this cooling works by detuning the addressing 369 laser red (lower frequency) of the transition. Due to the Doppler effect, atoms moving counter propagating to the laser $\boldsymbol{k}$-vector absorb photons preferentially. In so doing the ion receives an $\hbar\boldsymbol{k}$ momentum kick, associated with the photon momentum, in the direction opposite to the atom motion [35, 36]. Once the photon is absorbed, the excited state has a lifetime of $\tau = 9$ ns before the photon is re-emitted into 4π of free space. The probability to emit a $\hat{\sigma}$ or a $\hat{\pi}$ photon is equally probable, when cooling we scatter from all of the excited states. Therefore, over many scattering events this acts to dissipate the atom motion in one direction into 4π, decreasing the atom motion in a direction which overlaps with $\boldsymbol{k}$ of the laser. Because the ions are harmonically trapped, as long as the $\boldsymbol{k}$ vector has overlap with all three principle axes of the trap this will cool the ions in all three dimensions. The rate at which photons can be scattered from this transition is given by [35, 36],

$$\Gamma = \frac{\Gamma_0}{2} \frac{s}{1 + s + (\frac{2\Delta}{\Gamma_0})^2} \tag{2.28}$$

Where Γ_0 is the natural linewidth of the atomic transition, in this case $\frac{\Gamma_0}{2\pi} = 19.7$ MHz, Δ is the detuning from the transition which is generally set to $\frac{\Gamma}{2}$, and s is the saturation parameter. The saturation parameter is given as the ratio of laser intensity to the saturation intensity I_{sat}. The saturation intensity is given by [35],

$$I_{sat} = \frac{\pi h c \Gamma_0}{3\lambda^3 B} \tag{2.29}$$

The branching ratio, B is approximately 0.995 for this transition, therefore on average all but one scattering event in 200 results in the atom returning to the ${}^2S_{1/2}$ manifold. This is important because this method of cooling relies on scattering many photons.

In the case of ${}^{171}\text{Yb}^+$, this is complicated by a low lying $D_{3/2}$ state. After 200 scattering events the ions internal state can decay to this $D_{3/2}$ state which has a lifetime of 53.2 ms, long enough to sorely limit cooling and long enough for background gas collisions in chains of substantial length to have deleterious impacts on the chain lifetime. To close this leak, a re-pumping laser at 935 nm is employed to excite ion population from the $D_{3/2}$ to an excited $[3/2]_{1/2}$ bracket state which has a high branching ratio back to the $S_{1/2}$ manifold, $B = 0.982$, and a short lifetime 38 ns.

This method of cooling is limited by the linewidth of the atomic transition being used. The limit is known as the Doppler limit, in terms of average kinetic energy it is given by $E_{kinetic} = \frac{\hbar\Gamma}{4}$ [35]. Expressed as the thermal population of the harmonic oscillator modes, the average phonon occupation is given by, $\bar{n} = \frac{\Gamma}{4\omega}$. This second limit tells us that the best Doppler cooling, for our trap parameters, will still have a thermal occupation of $\bar{n} \approx 5$. To cool to the ground state, we must use sub-Doppler cooling through coherent operations[4].

The cooling is further complicated by additional Zeeman and hyperfine structure. The hyperfine structure requires additional frequency components be applied to both the re-pump and the cooling laser light to bridge the hyperfine splitting between the ground state and excited state hyperfine manifolds. For cooling, this means applying 14.7 GHz sidebands to the 369 nm light, and for the re-pumper. 3.07 GHz sidebands must be applied to the 935 nm laser[5].

Because the the ground state $S^{1/2}\ |F=1\rangle$ manifold has three-fold degeneracy and through cooling we couple these states to the $P^{1/2}\ |F=0\rangle$ excited state, which has a degeneracy of one, after several cooling cycles the ions spin state will be pumped to a coherent dark state of the ${}^2S_{1/2}$ Zeeman states. This dark state will have no excitation probability to the ${}^2P_{1/2}\ |F=0\rangle$ excited state. In fact because $J_f = J_i - 1$ there are are always two coherent dark states for any static polarization of laser light [37]. This effectively turns the ion transparent to the cooling light. To resolve this problem we apply a magnetic field, which acts to define a quanti-

---

[4] Discussed in depth in section 5.1.

[5] Described in detail in section 3.2

zation axis as well as to break the degeneracy of the Zeeman levels and destabilize the coherent dark state [37]. In out case this magnetic field is approximately 5.1 Gauss. Care must be taken not to increase this splitting beyond the linewidth of the transition so that a single addressing frequency can still drive transitions from all of the Zeeman lines.

2.3.3 Spin Sate Initialization and Readout

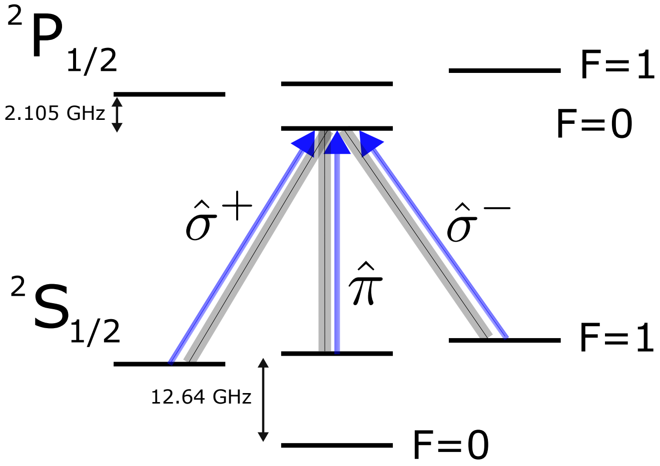

Figure 2.12: The gray line shows the possible decay paths and one can see that there is no connection to the spin down state.When detecting the spin state of the ion, we want to scatter many photons without decaying to the $|F = 0, m_f = 0\rangle$ ground state.

Generally we define our qubit using the spin state of the ion as the occupation of the the $|m_F = 0\rangle$ states in the $^2S_{1/2}$ ground state manifold, spin-down we define as $|\downarrow\rangle = |F = 0, m_F = 0\rangle$ and spin-up as $|\uparrow\rangle = |F = 1, m_F = 0\rangle$. Resonant photons can be scattered from the ions if the 369 nm laser is resonant with the transition from the $^2S^{1/2}$ $|F = 1, m_F = 0\rangle$ ground state (spin-up) to the $^2P_{1/2}$ $|F = 1, m_F = 0\rangle$ excited state. The excited state in this case can only decay to the $^2S_{1/2}$ $|F = 1\rangle$ manifold, therefore we can scatter many photons and look at histograms of collected photons to determine the population of spin-up vs. spin-down.

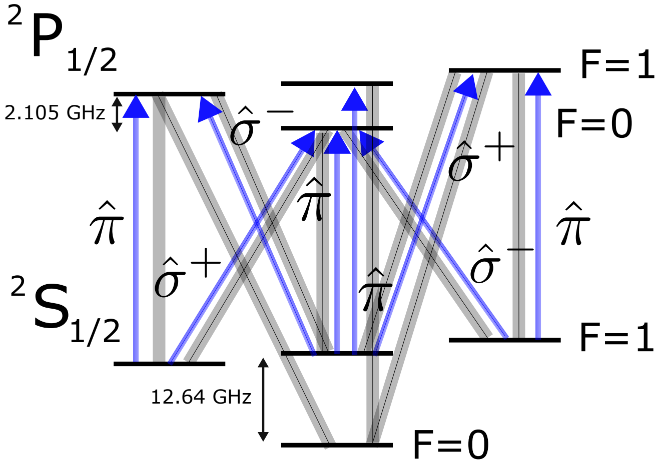

Figure 2.13: To optically pump the ions we apply sidebands to the light to connect the states joined by blue arrows, these states have decay paths shown as grey bars. Because the $|F = 0, m_f = 0\rangle$ state is not connected to the excited states via any blue arrows but the excited states can decay, via grey bars, to this state; after on average three scattering events the ion population will be pumped into this state.

To initialize these populations, we turn on a 2.105 GHz sideband on the resonant light discussed above which can decay to the spin-down state[6]. However there is no coupling out of the spin-down ground state. By turning on this sideband we can efficiently optically pump the internal degrees of freedom of the ion to $^2S_{1/2}$ $|F = 0, m_F = 0\rangle$. This allows us to start with a pure spin state. This procedure only takes three scattering events on average. The recoil momentum of a 369 nm photon is much less than the secular frequencies of the trap, therefore it takes many scattering events to introduce a quantum of excitation. This also allows us to use this technique later to reinitialize spins for sub-Doppler cooling without inducing very much heating.

---

[6] Described in detail in section 3.2.

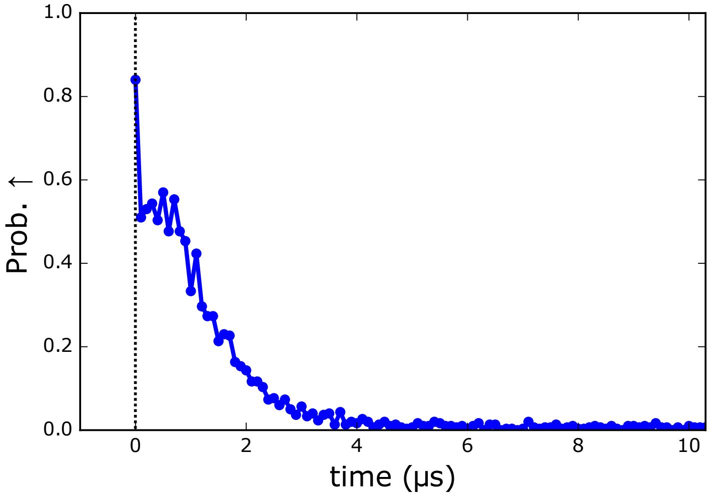

Figure 2.14: Average florescence of an ion as we gradually increase the time we pulse on the frequency sidebands for optical pumping. As this time is increased it becomes more likely that the ion will decay to the $|F = 0, m_f = 0\rangle$ state and no longer scatter any photons, this is seen in the decrease in ion florescence observed at longer times.

Chapter 3: Experimental Apparatus

The experimental apparatus can be broken down into several parts: the vacuum chamber, which is used to trap and store ions. The optics, which are used to trap and laser cool ions, as well as collect the light scattered from the ions during detection. The Raman laser, which drives coherent operations between the clock states of the ions. Finally, the electronics and control system which orchestrates the interplay of all of the dynamical process introduced by the other systems. In this chapter I will go over each of these systems and their sub-systems in detail.

3.1 Vacuum Chamber

A fundamental limitation to the number of ions in an experiment that one can achieve in a trapped ion quantum simulator or quantum information processor is fundamentally linked to the quality of the vacuum in the chamber that houses the ion trap. The longer the ion chain is, the higher the probability of collisions occurring with background gases. When there is more than one ion in the trap, re-cooling from such collisions can be extremely difficult because the ions push each other into orbits of the trap which can actually drive ion motion non-conservatively until ions begin to exit the trap. Usually when these collisions occur in large ion chains, the ion loss is catastrophic, resulting in only a single trapped ion after re-cooling.

Because of this, the trade off between the length of an experiment and the length of the ion chain being used are strongly dependent on the quality of the vacuum chamber. It is therefore paramount to achieve the best vacuum possible, vacuum pressures commonly achieved are in the low 10^{-11} Torr range. This regime is known as ultra-high vacuum (UHV), and achieving this level of vacuum requires a great deal of care when assembling the vacuum chamber. Most importantly, before any component is introduced to the vacuum side of the chamber it undergoes a rigorous cleaning procedure.

In the case of the vacuum chamber discussed in this thesis this process consisted of an ultra-sonic cleaning of all parts first in a bath of SimpleGreen and water, to remove excess greases and hydrocarbons, followed by a bath of spectroscopic grade acetone and finished with a bath of methanol. Once assembled the chamber was baked, with blank steel flanges in place of the vacuum windows, at 200°C for two weeks. At this point the chamber was cooled down to room temperature, the trap and windows were installed, and the chamber was baked again at 200°C for eight hours followed by two weeks at 180°C[1].

3.1.1 External Chamber Components

All external components are joined with metal to metal seals. In most cases this means a ConFlat (CF) seal. This seal consists of two stainless steel "knife-

---

[1] This was done to be sure that surface effects would not damage the trap. For example if there was any pinned Aluminum in the trap would not grow 'whiskers', needles of Aluminum that grow out the planar surface, these 'whiskers' can break through ground layers of the trap shorting various trapping components. This is less of a concern for the trap we are currently using.

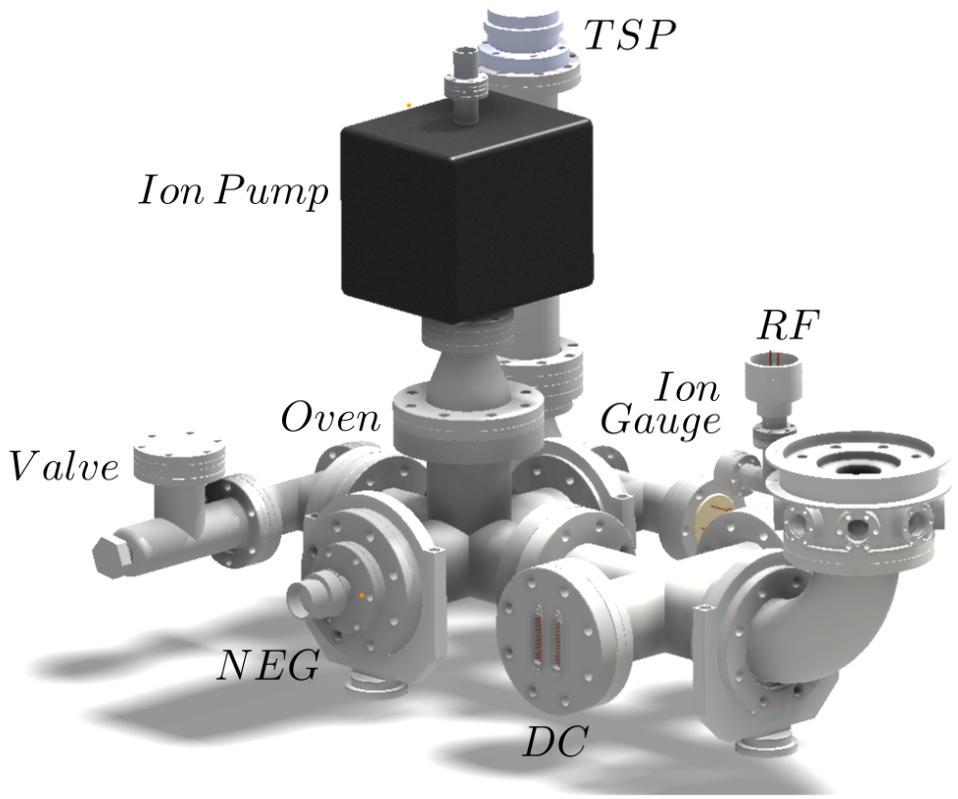

Figure 3.1: CAD model of the vacuum chamber, labeling all of the relevant external controls.

edges" on either side of the seal compressed into a copper gasket. This permanently deforms the gasket to form the seal, and the chamber consists of many of these CF components. The trap itself sits in the "spherical octagon" and all the wires necessary for controlling a micro-fabricated trap exits through the 90° elbow on the bottom 4.5" flange of the octagon. These wire are then routed out of the vacuum chamber by D-sub connectors on the 4.5" four-way cross. Each feed-through flange supports 50 wiring connections.

This four-way cross is attached to a five-wave cross that connects to all the pumps and any additional feed-throughs. On the top of the cross is a 20 l/s ion pump used to maintain the UHV conditions. On the bottom left there are connections to an NEG cartridge from SAES (CapaciTorr D 400-2). This pump is made of sintered porous Zr-V-Fe alloy disks which have high pumping rates for Hydrogen gas as well as active gases. Opposite the getter is a three-way cross which houses a nude UHV ion gauge to measure the vacuum pressure in the chamber and a Titanium sublimation pump, which works by coating the inside walls of the chamber with Titanium, which is a very good getter.

At the back of the cross there is another 2.75" tee which we use to attach a high current feedthrough for the oven connections. This tee is also used to attach an all-metal valve which we open during the bake out procedure to pump out the chamber with mechanical pumps. This is necessary when the chamber reaches atmosphere, because the internal pumps cannot handle a large gas load. When cooling down the oven during the bake out procedure we seal this value and turn on the internal pumps. The valve has a CF gasket internally which is pressed into a "knife-edge". If this is done consistently at the appropriate torque this gasket is re-sealable. The decision to make everything 4.5" in diameter was made to maximize the conductance to the internal ion pump and any external pumps used for baking the system.

3.1.2 Internal Chamber Components

All internal components are chosen to have as low of an out-gassing rate as possible, and whenever possible we refrained from using components which are comprised of organic or porous materials. Organics, like plastics, tend to have worse out-gassing rates compared with properly cleaned ceramics or metals. Porous materials can and will absorb the solvents used to clean them and then re-emit them under vacuum conditions, which will limit the ultimate vacuum pressure achieved. The internals of the vacuum chamber consist almost entirely of a wiring harness that takes the connections from the trap electrodes to outside of vacuum.

In the spherical octagon, there are two groove grabbers that secure the stainless steel wiring harness to the octagon. The trap assembly is plugged into a polyether ether ketone (PEEK) socket, which is itself mounted to the wiring harness. All of the 98 DC connections are routed out from the socket with 22 AWG kapton coated wires; the RF connections[2] are also made through this socket, however they are directly routed out of the vacuum chamber via a 1.33" feed-through on the octagon to minimize the length of the RF line. The socket is formed by two pieces of custom machined PEEK, which captures 100 gold plated sockets that are crimped to the ends of kapton wires. The PEEK has holes oriented so that a standard ceramic pin-grid array (CPGA) can plug into the captured sockets. The trap that is discussed in this thesis only has 48 DC electrodes, but this socket configuration is standard across current ion trap foundries. In principle any micro-fabricated trap currently available from GTRI, Honeywell, or Sandia can be plugged into this socket.

Besides the trap, the other major component internal to the vacuum chamber is the Yb oven. We use an isotoptically enriched source of Yb that was purchased from Oak Ridge National Labs. The oven is constructed from a tube of stainless steel; one end of the tube is crimped shut and the other end is open. There are

---

[2] The RF lines constitute a current carrying wire and the current return which is connected to the chamber at the resonator and to the ground plane of the chip.

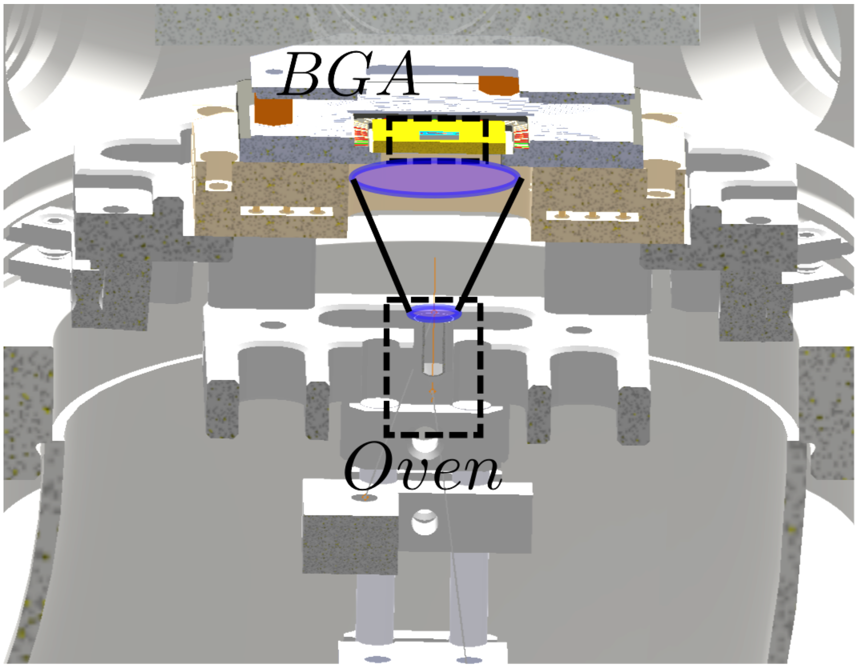

Figure 3.2: Schematic of the oven, the oven is set back from the trap by approximately 1 inch, the oven is an open aperture that sprays neutral Yb at the trap. The small slot through the trap lets a relatively collimated beam of Yb into the trapping region. The oven is supported by two stiff stainless steel wires of diameter 20 mil.

stainless steel wires spot welded to the exterior of the tube at either end, these wires are bent to hold up the oven assembly. Each wire is wound around a gold plated screw attached to a metal block; a kapton wire also attaches to the block and is routed out of the vacuum chamber via a high current feed through. These wires constitute the current and current return for the oven. When current is run through the tube, it is resistively heated and sublimated Yb can exit the opening at the top of the oven. This oven is pointed so that atom flux will be perpendicular to the trap plane and directed at a small slot cut into the trap which will allow atoms to pass through the trapping structure. The backside of the trap is coated with a grounding layer and the gaps in-between electrodes are undercut to avoid sublimated Yb from shorting the trap. This assembly is held by the stainless steel blocks which bolt around macor rods attached to the metal wiring harness, which allows the oven to be thermally and electrically isolated from the rest of the chamber.

3.2 Optics

Almost all of the available adjustable parameters in this experiment are optical. All the interrogation of atoms is done with lasers, and our ability to discern anything about the atomic quantum states is determined by collected the light which is scattered from them. Which is to say that this piece of the experimental apparatus is one is which we need the highest degree of accuracy and control. There are three main tasks for which we use optical elements: ionize and the Doppler cool[3] the ions in the trap, image the light scattered from the ions to determine information about their internal degrees of freedom[4], and finally interrogate ions with laser light to manipulate their internal degrees of freedom[5]. The following subsections will describe the physical systems that achieve these tasks.

3.2.1 Cooling and Trapping Beam Paths

The Doppler cooling and ionization light is generated by external cavity diode lasers. The 399 nm and 935 nm lasers are DL 100 Toptica lasers, and the 369 nm laser was produced by MogLabs. The final laser we have is a 780 nm DBR laser which is locked via a saturated absorption lock to a Rb spectroscopy cell. The 780 nm light provides a stable reference for a WSU-2 wavemeter from High Finesse.

---

[3] The theory of this is discussed in section 2.3.2

[4] The theory of this is discussed in section 2.3.3

[5] The theory of this is discussed in section 4.1.1

This wavemeter is then used to lock the frequencies of the other lasers.

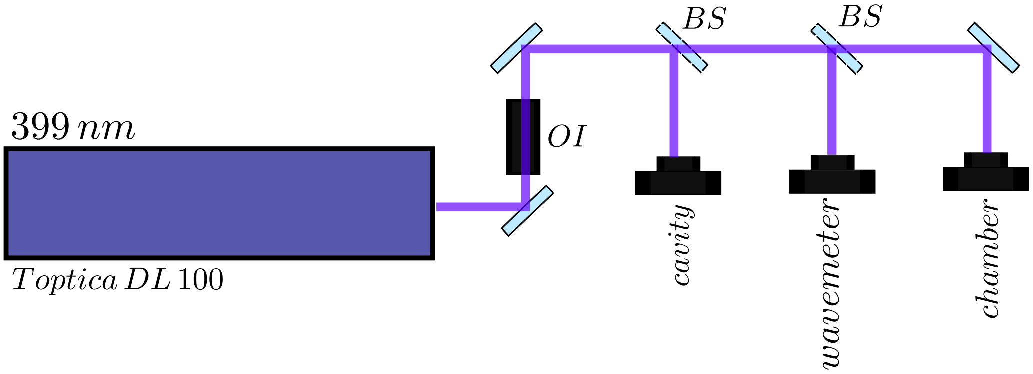

Figure 3.3: Optics for the the 399 nm laser the light is split out to a wavemeter to read the frequency, a cavity to lock the frequency, and finally to the chamber to be used as the first stage in photoionization

The 399 nm beam path is the most straight forward, and consists of an optical isolator followed by several pelical beam splitters to route the light into various fiber couplers. There is a coupler for a cavity locking setup, which in the future will be used along with the other lasers in a scanning transfer cavity lock [6]. Another coupler brings approximately 20 μW of power to the wavemeter currently being used to lock frequencies. An additional 700-900 μW of power is fiber coupled to the chamber. Once at the chamber, the beam is focused to approximately $w_0 = 70\,\mu$ m and is directed perpendicular to the axial trapping direction, $\hat{z}$. The beam is then raised 60 μm to address atoms as they pass through the loading slot and cross the trapping region.

The 935 nm laser is our $^2D_{3/2}$ state re-pump laser, and also has a relatively simple beam path. The laser passes through an optical isolator and then is split into three arms see Fig 3.4, each going to the same assemblies as the 399 nm arms,

---

[6] See Appendix A for a more detailed discussion of locking schemes.

as seen in Fig 3.3. The only difference is the light that gets directed to the chamber first passes through a 3.086 GHz free space electro optical modulator (EOM) from New Focus. This EOM introduces frequency sidebands on the light by modulating the index of refraction of an internal crystal at an applied RF driving frequency. Light passing through the crystal experiences shifts in the index of refraction at this RF oscillation frequency, this imparts a time dependent phase shift to the light, $E(t) = E_0 e^{i(\omega_0 t + \beta \cos(\omega_{RF} t)}$. If we expand this in Bessel functions we get an electric feild of the form, $E(t) = E_0 \left(J_0(\beta) e^{i\omega_0 t} + J_1(\beta) e^{i(\omega_0 + \omega_{RF})t} - J_1(\beta) e^{i(\omega_0 - \omega_{RF})t} \right)$ [38]. This imparts frequency sidebands to the light at the drive frequency with a modulation depth dependent on the applied RF voltage. This modulation allows us to use one laser to re-pump all of the possible hyperfine states coupled between the $\mathrm{D}_{3/2}$ and the $[3/2]_{1/2}$ bracket state.

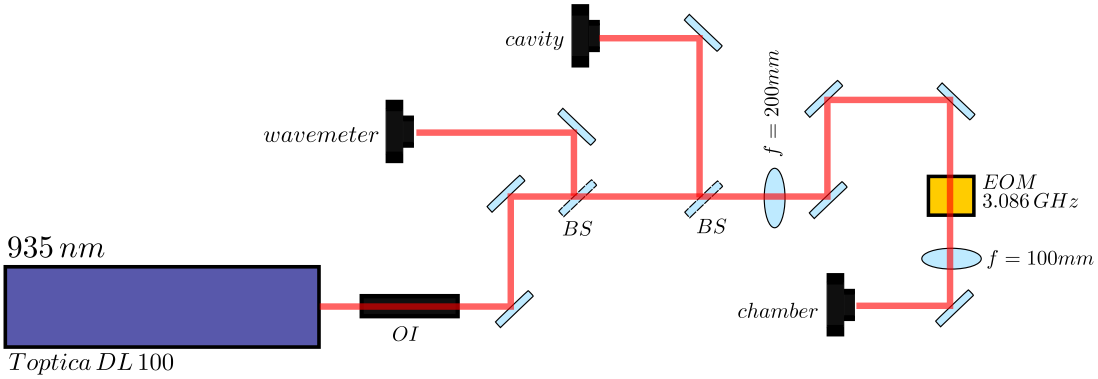

Figure 3.4: Optical setup for the 935 nm light The addition of the EOM is the only difference from the 399 nm beam path, this EOM is from NewFocus and is used to bridge the hyperfine splittings of the $D_{3/2}$ and $[3/2]_{1/2}$ states.

The final laser system is far more complicated. This is maybe unsurprising, as this is the laser used to ionize, cool, and detect the spin state of the trapped ions. The 369 nm laser is also a direct diode laser, it passes through an optical isolator at which point it is split into two paths, one that is subsequently split again to send power to both the cavity as well as the wavemeter. The amount of power sent to these paths is controlled by a waveplate and is varied to minimize the amount of power directed to these arms.

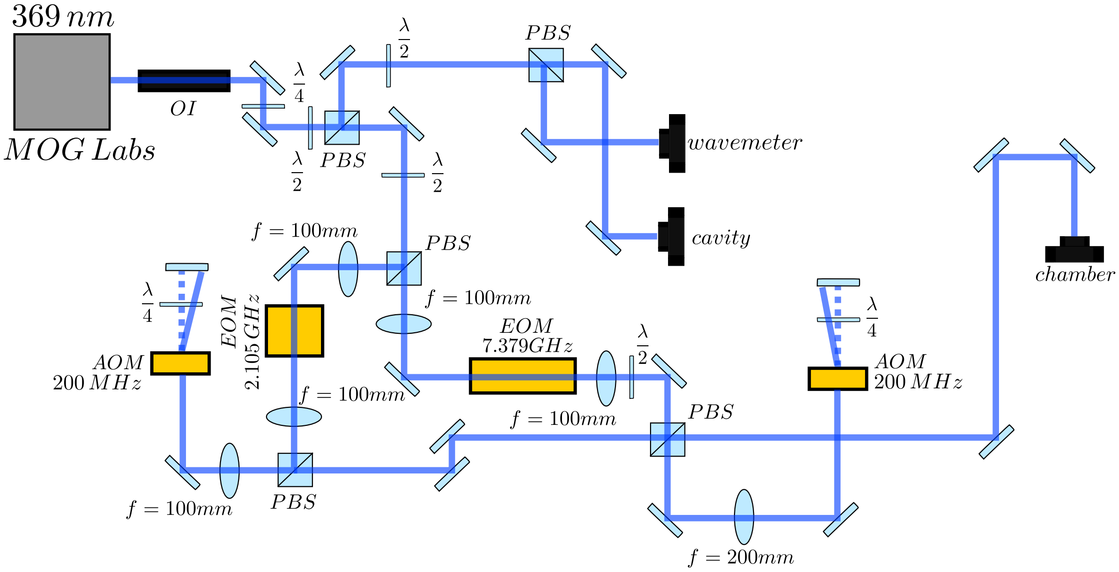

Figure 3.5: Optical setup for the 369 nm laser. The 369 beam path is the most involved, this path involves two acousto optical modulators (AOM) and two EOMs. Both AOMs are from Brimrose and the EOMs are from NewFocus. The 7.14 GHz EOM is to impart sidebands to drive all possible transitions to scatter the maximum number of photons during cooling. The 2.105 GHz EOM is used to optically pump the ions to the $|F = 0, m_f = 0\rangle$ ground state.

The remaining power is split between two arms via polarizing beam splitter. One arm passes through a 7.379 GHz free space EOM, from New Focus. This EOM provides second order frequency sidebands at 14.758 GHz, the qubit splitting, 12.65 GHz, plus the hyperfine splitting of the $^2P_{1/2}$ excited state, 2.105 GHz. This arm is our Doppler cooling arm. These sidebands allow us to scatter photons from all ground states[7]. Once light passes through this EOM, it is directed towards a double-

---

[7] Discussed further in Chapter 2

passed acousto-optical modulator (AOM). We use a double pass configuration to shift the frequency of the beam without shifting its position.

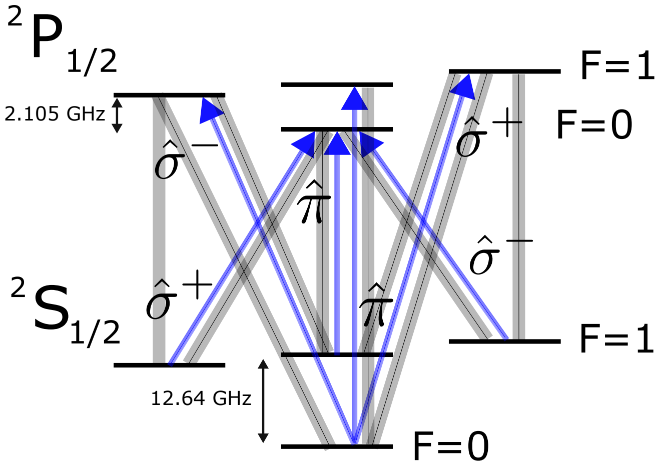

Figure 3.6: Re-print from section 2.3.2 for ease of reference. To scatter as many photons as possible we send in light with all polarization components and apply sidebands to the 369 nm light to bridge the ground and excited state hyperfine splitting. The blue arrows represent the states connected via dipole allowed transitions driven by laser light. The grey bars represent the possible spontaneous decay paths from those excited states.

The AOM works by applying a running acoustic wave to an internal crystal, whcih diffracts light as it passes through the AOM. The light will absorb the momentum, $\pm\boldsymbol{k_{acoustic}}$, shifting the propagation direction and shifting the frequency of the light to maintain energy conservation. Our 369 nm AOM systems are set up to maximize the -1 order of diffraction. This beam is then sent through a $\frac{\lambda}{4}$ waveplate and onto a mirror at normal incidence. The light then passes back through the whole assembly. The frequency of the light is shifted by twice the AOM drive frequency but is not shifted in position. We set the frequency shift such that we are red detuned from the $^2S_{1/2} \leftrightarrow^2 P_{1/2}$ transition by 10 MHz for Doppler cooling the ions. However, in the double-pass configuration we have the ability to easily tune this frequency. Once the light hits the PBS that was directing it towards the AOM the polarization has been rotated 90° by passing through the $\frac{\lambda}{4}$ waveplate twice. The beam then passes or reflects where previously it reflected or passed. This is a common place technique in atomic physics experiments where the frequency of light needs to be controlled quickly without affecting the final position of a beam.

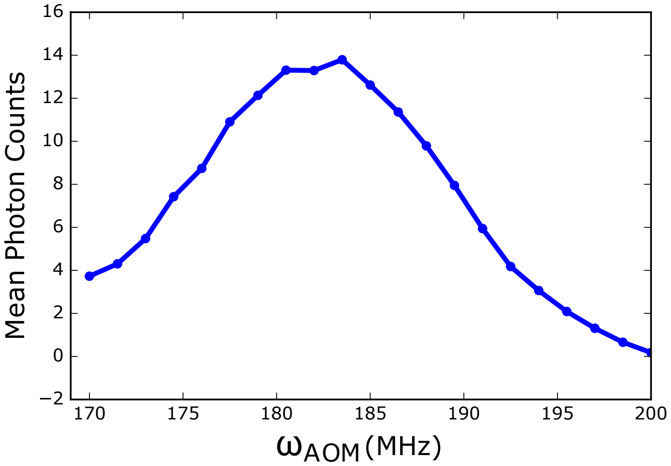

Figure 3.7: Scattered phtons from the $S_{1/2} \rightarrow P_{1/2}$ transition as a function of the AOM frequency. By scanning the frequency of the detection AOM, we can scan the $S_{1/2} \rightarrow P_{1/2}$ transition to determine where to tune the AOM frequency to maximize scattered photons.

The other arm is similarly directed onto a free space EOM from New Focus, operated at 2.105 GHz. This EOM, which we pulse on and off during the course of an experiment, applies a sideband to the light at the hyperfine splitting of the ${}^2P_{1/2}$ excited state. From this state the ion can decay to both the $|F = 1\rangle$ and $|F = 0\rangle$ ground state manifolds. This light will couple the $|F = 1\rangle$ ground state manifold to the excited ${}^2P_{1/2}$ state but does not couple the $|F = 0\rangle$ ground state to the excited state, because this state is detuned by 12.64 GHz[8]. This sideband optically pumps the ion spin state to the $|F = 0\rangle$ ground state, this is how we initialize the spin state

---

[8] Discussed in depth in section 2.3

of our ions.

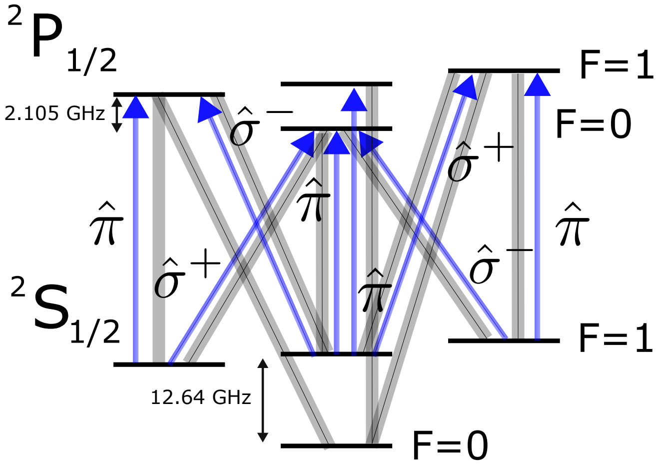

Figure 3.8: Atomic energy levels used to initialize the ion in a pure spin state we make use of the hyperfine splitting in the ground state, we can decouple it entirely from the resonate excitations of the upper hyperfine manifold. By scattering off the F=1 manifold depicted in blue, ions can decay via the grey pathways to the F=0 ground state manifold, thus pumping the ion to the $|F = 0, m_F = 0\rangle$ state.

This beam without the sideband works as our detection beam. When this sideband is off, the light is resonant with the $^2S_{1/2}\,|F = 1, m_F = 0\rangle \leftrightarrow {}^2P_{1/2}\,|F = 0, m_F = 0\rangle$ transition. The decay of this excited state has zero overlap with the $^2S_{1/2}\,|F = 0, m_F = 0\rangle$ ground state, due to angular momentum selection rules. Therefore we can scatter many photons from this spin state before it exits our qubit spin basis. This arm also passes through an AOM which we use to shift the frequency of this transition to optimize scattering. Once it has exited the AOM setup it is recombined with the cooling beam on a PBS. Both beams are then directed onto the same fiber and sent to the chamber.

Once at the chamber the light is split into two arms, each arm contains cooling, pumping, and detection light. Each arm is focused down to approximately 30 μm and is directed at 45° to the axial trapping direction, $\hat{z}$, to give an overlap with all

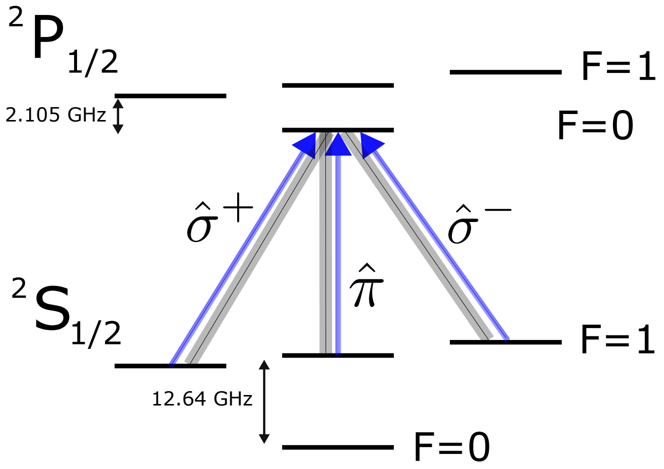

Figure 3.9: Atomic energy levels used for detecting the spin state of the ion. The gray line shows the possible decay paths and one can see that there is no connection to the spin down state.

principal axes of the trap. One arm of this light is directed towards the loading zone of the trap and the other is directed to the region where we couple the ions to the Raman laser, these regions are separated by 250 μm.

3.2.2 Imaging system

To determine the spin state of ions, as previously described, we scatter photons off of the $^2S_{1/2} \leftrightarrow {}^2P_{1/2}$ transition. We then need to collect the scattered photons, the more photons we collect the higher our confidence will be in the spin state discrimination. This is complicated by off resonant coupling to the $^2P_{1/2}\,|F=1\rangle$ manifold, which can scatter back to the $^2S_{1/2}\,|F=0\rangle$ ground state manifold. For fixed laser power and detuning, the longer we attempt to collect scattered photons, the higher the probability we will off resonantly scatter to the $^2S_{1/2}\,|F=0\rangle$ ground state. Therefore, the faster or the more photons we collect the better the discrimination will be between the spin-up and spin-down states.

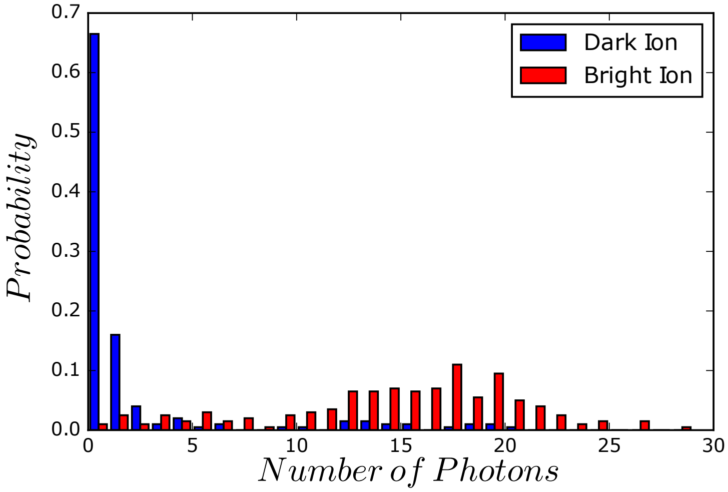

Figure 3.10: Histograms of collected photons when illuminated for 200 μs. The red bars, in which we collected 15 average photons, indicates this ion is bright. The blue bars indicates a dark ion. The intermediate photon numbers is indicative of the cross talk we see between PMT channels. This histogram was taken with multiple ions in different spin states in the trap. The shelf of low photon counts for the bright ion is indicative of off resonant pumping to the $^2S_{1/2}\,|F=0\rangle$ ground state.

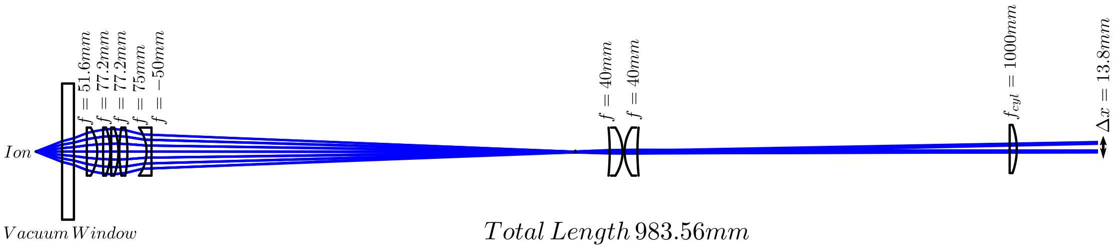

Figure 3.11: Optical layout for the ion imaging system. The first set of 5 lenses is a multi-element objective that has a working distance of approximately 25 mm and an NA of 0.4, corrected for the vacuum chamber window thickness. The intermediate image plane is focused back to either a mutli-channel PMT or a camera to image ions. The final cylindrical lens is used to correct for astigmatism in the lens stack. The distance between the two final spots shows the displacement of the images formed by two ions separated by 50 μm at the trap yielding a magnification of 276

To collect photons we employ a multi-element objective which has an NA≈ 0.4 and a working distance of $WD \approx 25.8$ mm. This objective forms an image plane 215 mm back from its last surface. This intermediate image is re-imaged with a doublet of two LBF254-040-A f = 40 mm best form lenses from Thorlabs. This doublet forms

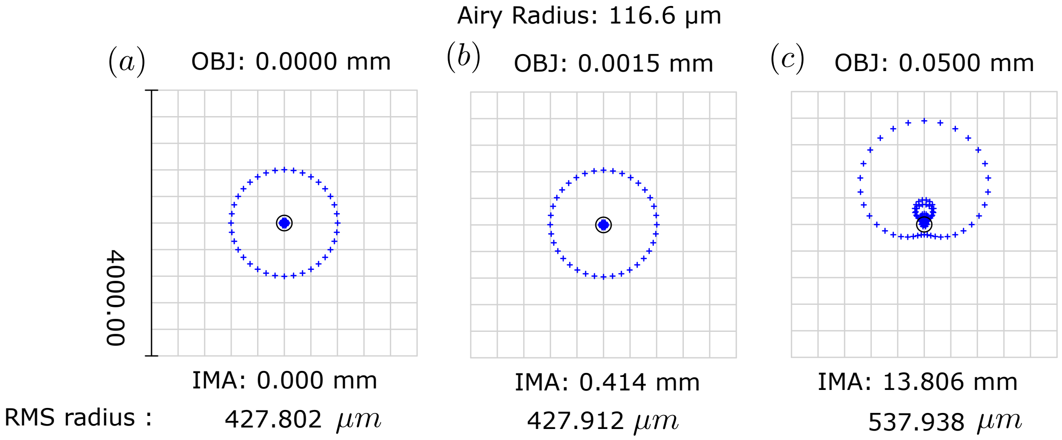

Figure 3.12: Spot diagrams for object ions separated perpendicular to the imaging axis. The purpose of this simulation is to determine what aberrations are induced by trying to image more than one position of the trap simultaneously. Diagram (a) shows the central ion, the black ring shows the Airy radius. The next spot diagram is for an ion displaced by 1.5 μm from the first ion, a close adjacent ion in the trap. The (c) image shows an ion displaced by 50 μm, the maximum distance we expect to have an ion if we trap the largest chain we can image. The other important thing to note is that the RMS radius of each spot is approximately 0.5 mm. This implies that well imaged ions should fit on a single PMT channel.

an image onto a multi-channel PMT 680 mm back. The multi-channel PMT has channels spaced by 1 mm, and the measured overall magnification of this systems is $M \approx 200$, there is a small discrepancy between the simulated and measured values[9]. This requires the ions to be spaced by at least 5 μm for individual detection, and in practice we use our ability to deform the axial potentials to space the ions out by at least 10 μm so that there is a dead channel in-between channels imaging ions. This reduces cross talk on the multi-channel PMT.

---

[9] This is measured by imaging trap features onto a scientific CMOS camera with known pixel size.

3.2.3 Raman Beam Path

The beam path for the Raman laser is the most critical, since the intensity of this beam directly affects the coherence of our qubit transitions[10]. We use a Paladin Compact pulsed NdYag laser from Coherent to generate these beams. This laser is a tripled 1064 pulsed laser, and is used commercially for photo lithography in semi-conductor fabrication facilities. Immediately out of the laser, a beam sampler directs a small portion of the light onto a fast photodiode to measure the repetition rate of the laser. We bridge the hyperfine transition by combining two pulse trains of this laser and interfering two comb teeth, generating a beatnote at the qubit splitting. This is followed by an AOM, which we use to stabilize the intensity of the laser. The non-diffracted order of this AOM is sampled by a pick-off mirror with very low reflectivity. The sampled light is then directed onto a slow photodiode to generate an error signal to feed back to the AOM power for stabilizing the amplitude of the pulse.

The beam is then split into two arms and focused down onto two AOMs. One of these AOMs is used as a feed forward control of the repetetion rate of the later[11]. The other is used to scan the frequency of the beatnote or apply multiple frequency components to this beatnote. By focusing the beam down onto these AOMs, we can use lenses afters the AOMs to image the waist formed in the AOM onto the ions. We do this so that frequency shifts do not result in beam translations at the ions. We collimate the diffracted orders out of each AOM,and pick off the +1 order

---

[10] Discussed further in Chapter 4.1.

[11] This will be discussed more fully in section 3.3.3.

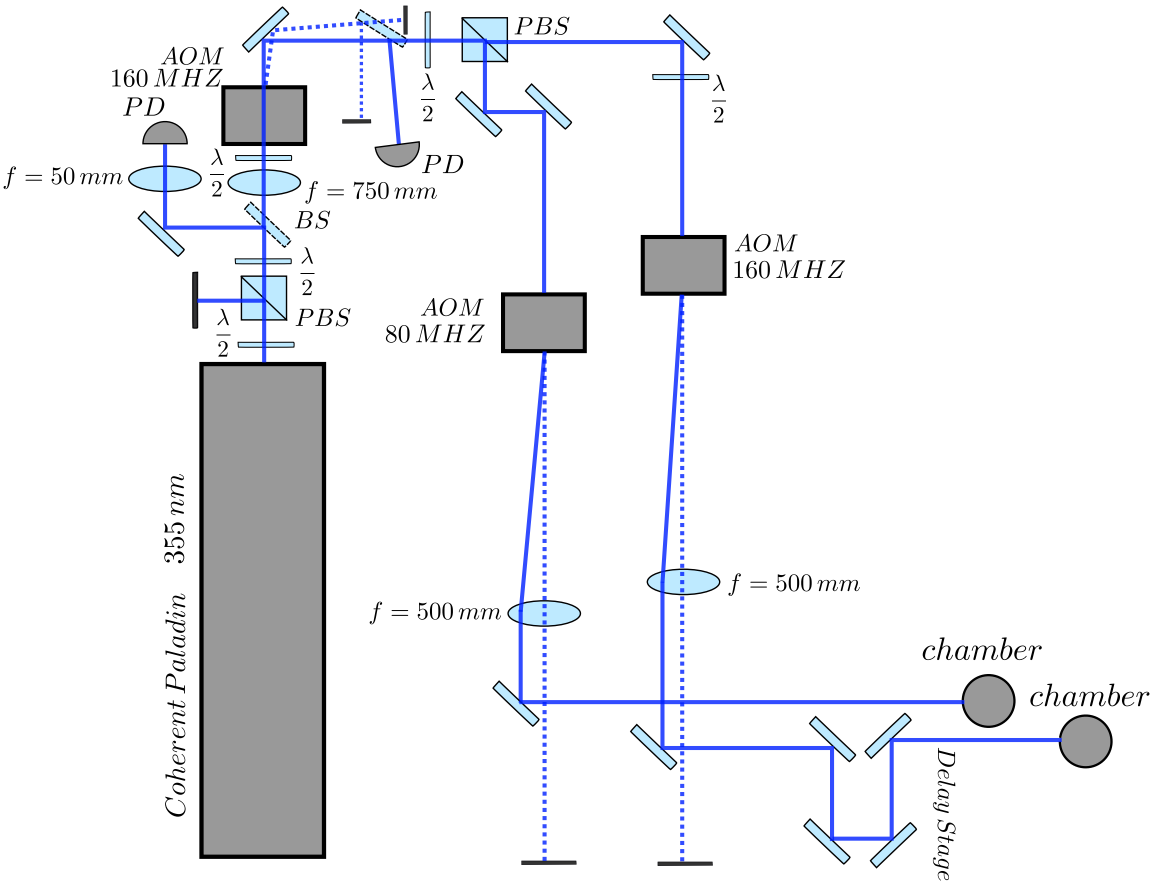

Figure 3.13: Raman beam paths to the chamber. The total path length is approximately 3 meters. The majority of this system is enclosed in beam tubes, which are in turn enclosed in a box constructed of 80/20 Allucabest panels. The reason for this is two fold: it protects people in lab from the UV light and helps prevent air currents from passing through the beam path. These air currents can cause gradients in the index of refraction in air and lead to pointing instability.

on a D-shaped mirror. One of these arms is directly sent to the chamber via a periscope, while the other arm passes through a variable delay stage. The delay stage is necessary to make sure that the pulses overlap temporally and spatially at the ion chain. Because we split the beam into two arms this delay stage acts to make the arms equal length.

Before these beams are focused down onto the ions, they pass through PBS cubes to achieve a clean horizontal polarization. At the ions, the beams are per-

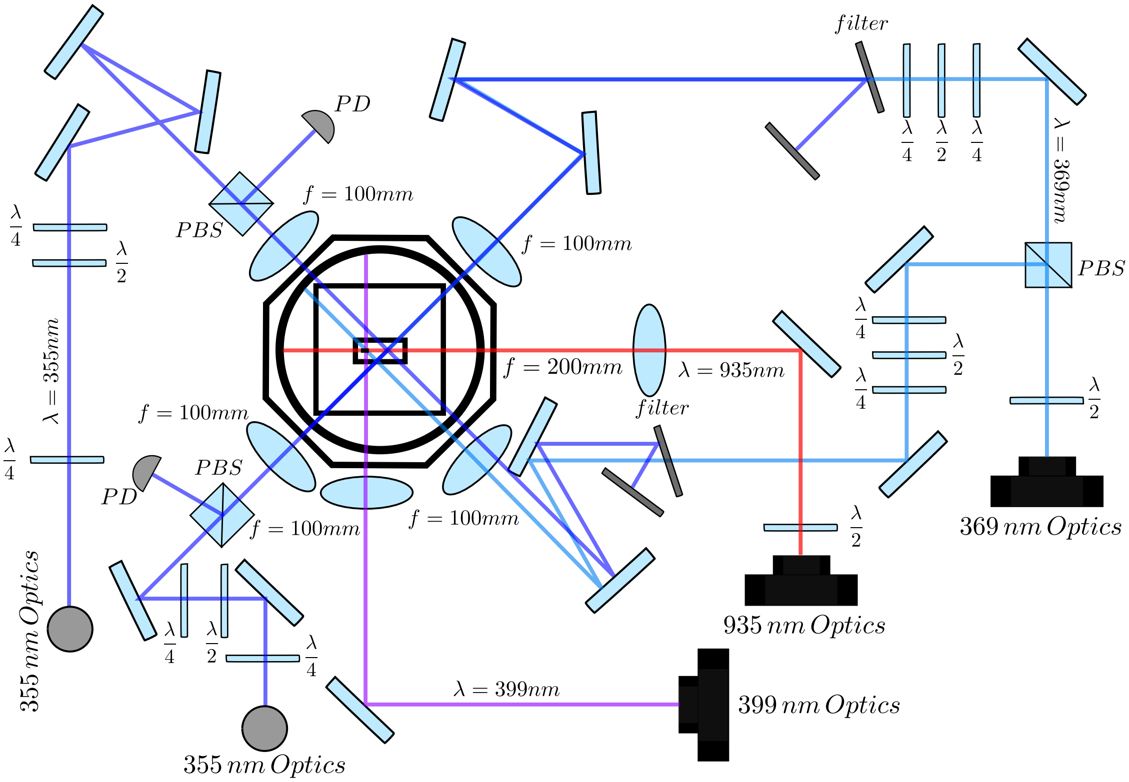

Figure 3.14: Beam paths for all of the lasers as they enter the vacuum chamber.

pendicular to each other and parallel to the trap surface. With the magnetic field defining a quantization axis pointing perpendicular to the trap surface, this satisfies the lin ⊥ lin configuration [39] of polarization needed to drive Raman transitions[12] in $^{171}\mathrm{Yb}^{+}$. Both beams are focused down with an f = 100 mm UV fused silica lens from Thorlabs, this results in beam waists of approximately 40 μm. These beams are oriented so that the $\delta\boldsymbol{k}$ of the two beams points parallel to the trap surface and along a direction perpendicular to the axial trapping direction. This lets us induce momentum transfer between the beatnote and the ion chain along only one of the transverse trapping directions[13].

Because of its commercial applications, this laser is almost entirely turn-key

---

[12] Discussed in depth in Chapter 4.1.2.

[13] Discussed in depth in section 4.1.3.

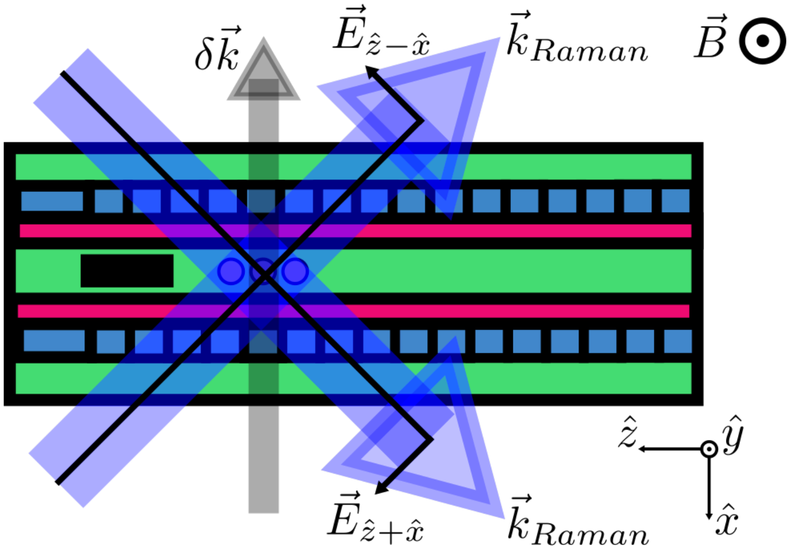

Figure 3.15: The direction of the ***k*** vectors of the Raman beams at the trap, with the relevant directions of the trap axes and magnetic field axes also defined.

and there is very little that the user has in the way of control. Unsurprisingly this is insufficient for our purposes. In particular, the cavity that generates the pulse train is totally inaccessible, and changes length over time which changes the spectrum of the frequency comb emitted. The repetition rates of these lasers is typically in the 80 MHz or 120 MHz range, where the exact frequency is variable laser to laser. To bridge the hyperfine splitting at 12.64 GHz, we must interfere two comb teeth separated by approximately 105 comb lines. That means 10 kHz shifts of the repetition rate change our beatnote frequency by MHz. Because we have no control over the length of this cavity, we must feed forward to a frequency modulator after the laser. I will discuss this stabilization circuit in depth in section 3.3.3.

3.3 Control Electronics

The final piece of the experimental apparatus not discussed so far are the control electronics. These can be broken down into electronics used to control the timing of operations in an experiment, the control over the DC and RF trapping voltages, and the electronics used to stabilize all the various parameters in the experiment which are not passively stable enough for our purposes.

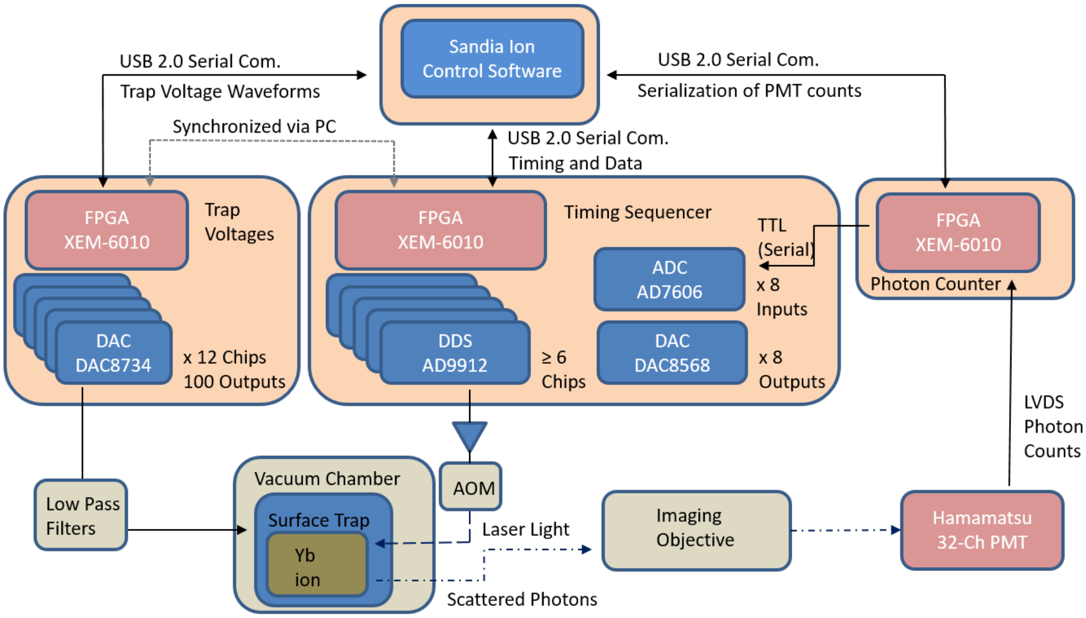

Figure 3.16: Illustration of the control structure, depicting all of the digital electronics used to control this experiment.

3.3.1 Timing Control

The timing control for our experiment is orchestrated by an Opal Kelly XEM6010-LX150 FPGA. This timing FPGA is clocked at 100 MHz, from an atomic Rb source, and is loaded with firmware developed as part of the Sandia ion control system.

This firmware allows us to write python like pulse programs that support “for” and “while” loop functionality as well as conditional branching of the experimental procedure. This functionality allows us to perform complex experimental procedures. We will take full advantage of this to do state distillation, which requires adapting the experimental procedure during the course of the experiment, depending on feedback from the ion. This is achieved by sending the timing FPGA multiple branches for all possible future operations. Because the experimental time scale of 10’s of μs this approach is preferable to sending new commands to the timing FPGA during an experiment. Such communications would be difficult to achieve with the asynchronous communication between the PC and the timing FPGA.

In addition to timing control, this FPGA also controls a handful of peripherals used in pulse programs. The parameters of these devices can be updated on the fly during the experimental procedure. These devices include 8 AD 9912 DDS chips, 8 DAC8568 digital to analog converters, 8 AD7606 analog to digital converters, as well as 24 digital inputs. We use these digital inputs to read in the signals from the muli-channel PMT. The current system takes low voltage differential signals (LVDS) from the multi-channel PMT’s individual channels to a separate Opal Kelly XEM6010-LX45 FPGA. This PMT FPGA emits TTL pulses on a digital line back to the timing FPGA for each LVDS signal. In the future, we plan to send back the number of LVDS counts received on all PMT channels through serial communication with the timing FPGA. This will be done over the same digital lines currently being used, this is why the task of translating LVDS to TTL signal is currently performed by an FPGA. In the future this PMT FPGA will be necessary to implement the logic to determine what serial command to communicate back to the timing FPGA.

This configuration of FPGAs allows the timing FPGA to get back photon count values, collected during the course of an experiment, on experimental time scales. That means the timing FPGA can be programmed with conditional logic that selects the next branch of operations based on returned photon counts. This allows us to perform feedback to the operational parameters during the course of an experiment.

The same digital lines are also used to communicate with another FPGA that controls the DC voltages, this is done so that we can change the voltages during the course of an experiment. This allows us to move and manipulate the ion position during an experiment, this is necessary for our individual addressing scheme [40].

3.3.2 Trapping Voltage Control

Generating and controlling both the DC and RF trapping voltages is probably the most challenging component of the experimental apparatus. The difficulties in producing stable, low noise DC lines and a stable RF line are distinct. The trouble with the DC lines arises from the sheer number of electrodes which must be controlled and filtered without compromising their dynamic performance. The challenges with the RF arise from the high voltage necessary and intrinsic reactance of the components making up the line into the vacuum chamber. Because of these differences, we will address each separately in the next two subsections.

3.3.2.1 DC Voltages

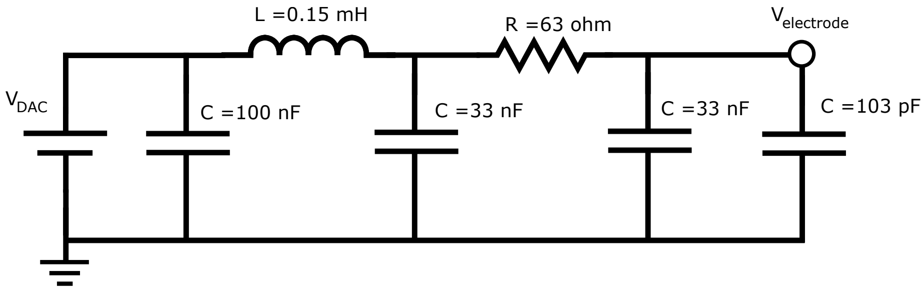

Figure 3.17: Circuit diagram for the 50 kHz third order Butterworth filters we use for each DC line. The final capacitor is the trench capacitor on chip which connects DC and RF chip grounds. There are 100 of these fitlers, split into four boards that plug directly into the chamber.

The DC voltages are generated with twelve DAC8734 digital to analog converters. Each chip has 8 output channels, each channel gives 16-bits of resolution on a bipolar ±16.5 V output. An XEM6010-LX45 FPGA is used to control each of these voltage sources. The DACs and DAC FPGA all reside on a board which routes all of these voltages out onto four 25 pin D-Sub connectors. We limit each of these lines to ± 10 V to protect the DC electrodes of the trap. Each D-sub line then plugs into filter boards attached to the vacuum chamber. To minimize the pickup from laboratory noise on these lines, these filter boards use third order Butterworth filters [41] on each line with a corner frequency of 50 kHz. This corner will limit how quickly we can update the DC potential, but for now our experiments have not tried to accomplish any fast transport of ions or diabatic excitation of motion.

During an experimental sequence, we have control over the voltages being output by these chips via the DAC FPGA. This FPGA is also connected to the main control computer. As part of the configuration of the experimental procedure,

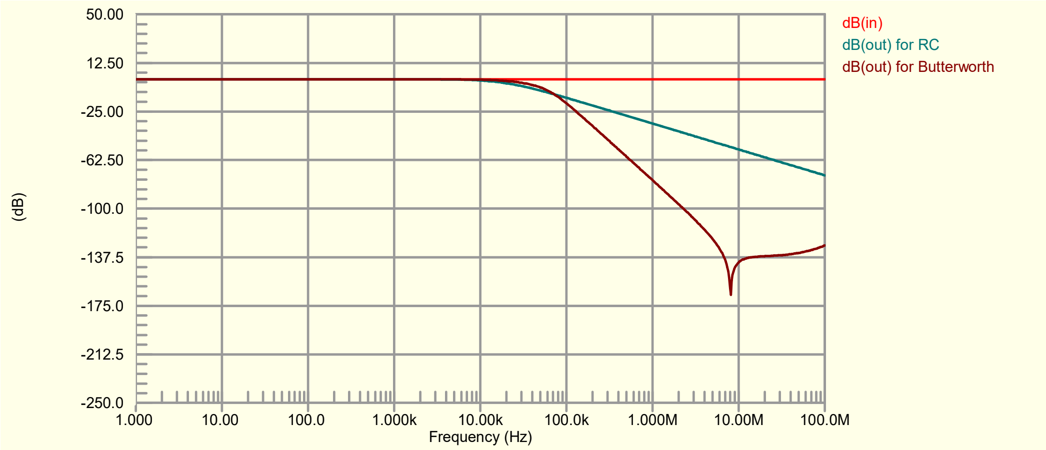

Figure 3.18: Simulated filter function for the Butterworth filters we use, the knee is somewhat softened by the intrinsic resistance of the inductor.

we define a large array of voltages for each DC line. These voltages correspond to simulated solutions to the DC potential along the axial trapping direction, $\hat{z}$. These simulations are based on Green's functions of the trap geometry. The simulations are performed by the trap designers and we have very limited access to the codes they use to do these simulations. We then specially define the specific solutions where we perform experimental procedure. These include specific positions along the trap, as well as solutions which change ion spacing, or add anharmonic terms to the DC potential. In general we have to get these specific solution types, once specified, from the designers of the trap. When the simulations are run we get specific solutions as well as the array voltages necessary to move between these specific solutions. One can picture these particular solutions as nodes in a graph, with the array defining the edges between nodes. By defining a graph in this way, we have a map between different points of interest.

As part of the configuration of these voltage nodes we define the rate at which voltages in the array should be applied to move from one node to another. We also define the interpolation between lines in this array, as well as any wait times to be executed as each line of the array is applied. When the nodes are defined, they are loaded with the array of edges into the memory of the DAC FPGA. The DAC FPGA and the main timing FPGA are connected via digital I/O lines of the main timing FPGA. When an experiment is initialized on the PC side the two FPGA's synchronize. To manipulate the ions during an experiment, the timing FPGA sends a serial command to the DAC FPGA that tells the DAC FPGA which edge between operational nodes to execute. The timing FPGA then waits for a signal from the DAC FPGA signaling completion of this operation before it continues with the experimental procedure. This "handshake" synchronization between FPGAs is sufficient for our purposes.

3.3.2.2 RF Voltage

The RF voltage applied to the trap is generated by an HP ESG-1000A source amplified and then filtered by a helical resonator [42]. The challenging aspect of generating this RF voltage is that the voltage at the trap is directly proportional to the secular frequencies of the trap, and the frequency must be clean enough to not drive secular motion of the trap[14]. Because of this second issue, we generally use quarter wave resonators to transform power to voltage on the open voltage node of the trap.

This resonator functions by coupling a source coil to a larger coil whose length is approximately one quarter of the desired RF drive wavelength. The end of the coil

---

[14] Discussed in depth in section 2.1.1.

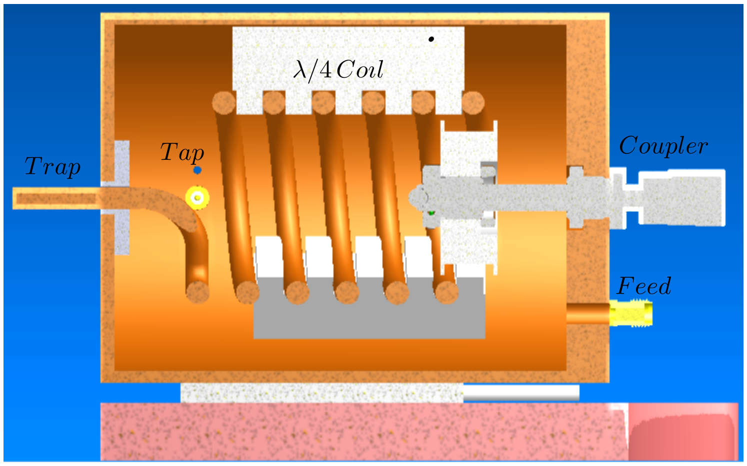

Figure 3.19: A cross section of the helical resonator used to step up the RF power to voltage to drive the transverse confinement of the trap.

near the source is grounded to the housing of the resonator, which has cylindrical symmetry. The other end of the coil is then connected to a feedthrough which is connected in vacuum to the RF rail on the chip. This end of the coil is an anti-node of the standing wave present in the resonator. By moving the source inductor in and out of the larger coil, we can change the coupling impedance between the two. On resonance, these circuits can have high quality factors $Q = \frac{\Omega_0}{\omega_\Delta}$, where ω_Δ is the full width half maximum frequency of the resonator and Ω_0 is the resonance frequency of the resonator. For our resonator, the drive frequency is $\Omega_0 = 35MHz$ and $Q \approx 200$. Since the secular frequencies of our trap are usually in the 1-3 MHz range, this is adequate spectral purity for the experiments we wish to perform. The bigger issue for our experiment is trying to maintain a stable RF voltage at the trap, this will be discussed in the next section.

3.3.3 Stabilization

Due to the sensitive nature of these experiments a handful of parameters must be controlled actively. The two which are the most important are the RF voltage and the beatnote frequency of the Raman laser. As previously stated the RF voltage in directly proportional to mode frequency. Therefore, this voltage must be stabilized or the coherence of a transition coupled via the motion will be strongly degraded.

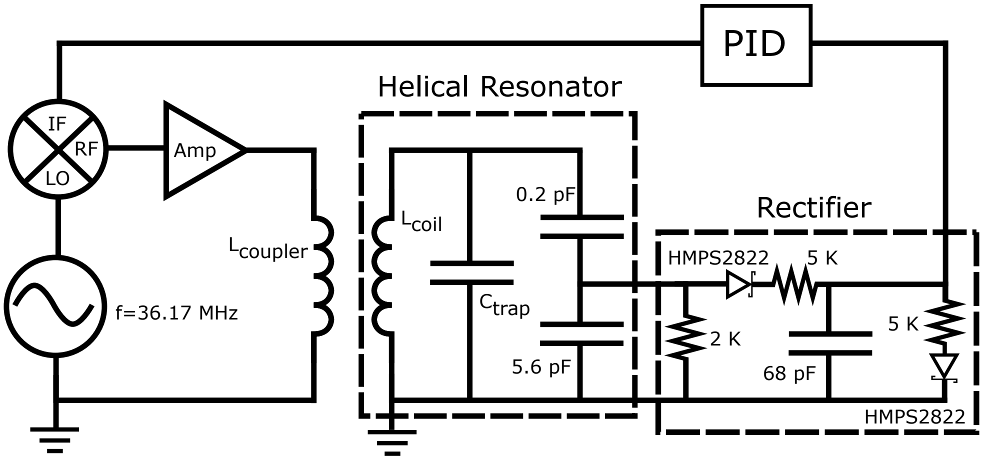

Figure 3.20: The lumped element circuit model of the resonate circuit used to step up the RF voltage for the trap.

The difficulty with stabilizing this signal is that it is high voltage at radio frequency, derived from a resonate circuit. Any dissipative elements used to sample the voltage will destroy the resonator quality factor. Because of this we use reactive elements, specifically a capacitive voltage divider to sample the high voltage anti-node of the resonator. If appropriate capacitors are chosen, the ratio of trap voltage tap voltage can be stable to a few parts per million. In our experiment, the ratio of trap voltage to tap voltage was measured to be 178. This signal is then sent into a rectifier to turn this RF signal into a DC error signal. Once we have a DC signal proportional to the RF amplitude, we feed this into a feedback loop [43]. Both the rectifier and the capacitive tap use very low thermal coefficient, passive components. The error signal is then sent into an off the shelf servo controller, NewFocus LB1500. We extensively test this feedback by measuring the stability of the secular frequencies. The context in which we took this data and its implications to our experimental goals are discussed in Chapter 6.

As stated previously, we interfere two comb teeth of our pulsed laser to create a beatnote at the qubit splitting to drive all the coherent operations detailed throughout this thesis. The beatnote must be stabilized because, as previously stated, the internal laser cavity that is generating these pulses is not actively stabilized. Because the length of this cavity directly determines the repetition rate of the laser, if environmental factors can couple into the length of this cavity, they can affect the beatnote frequency. Unfortunately, our laser does not provide any external control of this cavity length so it cannot be directly stabilized. However, because the beatnote driving our Raman transitions is derived from two beams split from the same source we can use an AOM to compensate for drifts in the repetition rate. This feedforward method of stabilizing the beatnote is very similar to the stabilization used in a phase locked loop (PLL).

To accomplish this lock, we sample the beam directly out of the laser and measure, with a fast photodiode from Alphalas, the frequency comb of the laser. By amplifying and filtering this comb we can isolate the specific comb line which will participate in driving Raman transitions. We then mix this comb line down with a stable frequency source. This source also acts as the global clock for all coherent

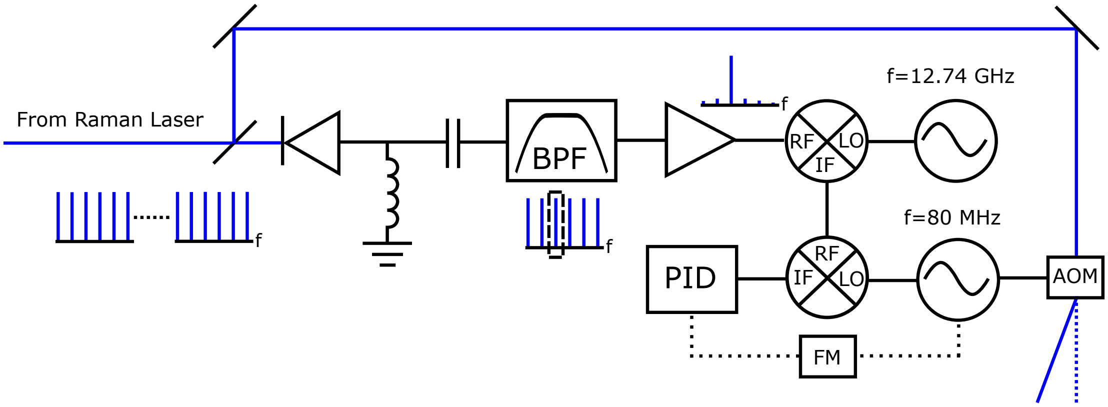

Figure 3.21: A schematic for the feed forward lock used to stabilize drifts in the repetition rate of the 355 laser. We use an HP 8672 for the microwave source and an HP 8640 for the AOM drive. The bandpass filter is a 12 pole waveguide filter which I optimized for the comb line of interest. It has a bandwidth of approximately 100 MHz and a center frequency of 12.8 GHz.

operations and therefore is referenced to a stable Rb clock. The demodulated beatnote signal, which is around 79 MHz, is then mixed with the source used to drive the AOM at approximately the same frequency. The resulting DC signal is fed into another servo (NewFocus LB1500). The feedback is applied to the frequency modulation port of the source driving the AOM. This allows us to remove shifts in the repetition rate of the laser before the light reaches the ions [44, 45].

3.4 Ball Grid Array Trap

The trap we used to do all of the experiments discussed here was developed in a collaboration between Honeywell and the Georgia Tech Research Institute (GTRI). The trap is known officially as the ball grid array (BGA) trap and implements a relatively simple linear trap design. The trap is gold on a silicon substrate, the ions when trapped sit approximately 60 μm from the surface of the trap. There are 48

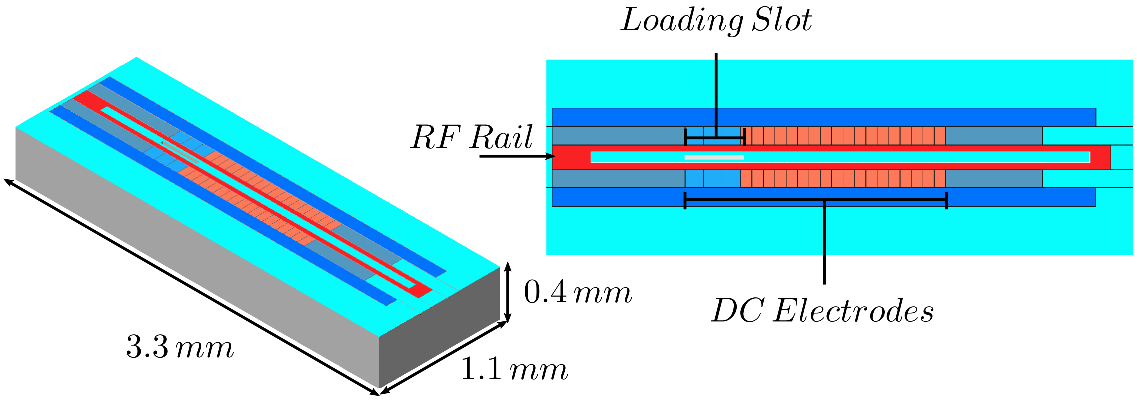

Figure 3.22: A schematic of the trap structure, the smaller DC electrodes in pink are 60 μm apart, the larger DC electrodes near the loading zone are 100 μm wide. The loading slot is approximately 60 μm wide. There are large DC electrodes around the periphery of the trap to help rotate the DC axes if necessary.

DC electrodes, 60 μm in width each, a slot for loading ions from the backside, and a specified ion to RF electrode distance of 94 μm. GTRI designed the trap and Honeywell fabricated the trap. The intent was to create a trap with high optical access. Because micro-fabricated traps are so small and the coupling between the RF and DC electrodes can lead to pickup of RF on the DC electrodes, by having small capacitors on-chip to mitigate this effect. This is a tradeoff, however, since these capacitors take up real estate on the chip. If you want to focus down laser beams to address individual ions, normally separated by no more than 5 μm, the Rayleigh length of those beams will be quite short. This means that the trapping structure itself can be the limiting factor when tightly focusing lasers above the surface.

Groups have tried a variety of approaches to get around this difficulty. The most popular of these approaches involves etching a slot through the chip which can have very high NA from above the chip [46]. Another recent approach has

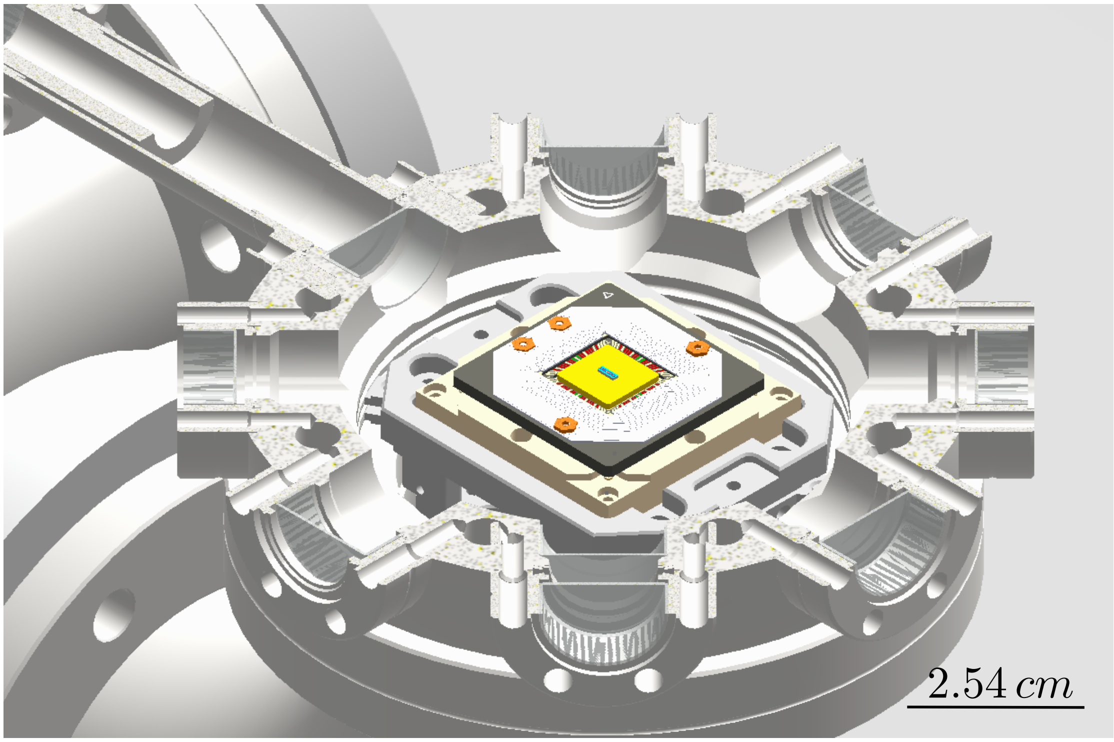

Figure 3.23: CAD model of the trap in the spherical octagon to give as sense of scale for how close the trap is to nearby surfaces.

been to raise a relatively small trapping area above the carrier which routes the electrical connections out to the ceramic pin grid array (CPGA) attached to the wiring harness. To do this, however, you have to find a place to put all of the filtering capacitors. This has led to the bow-tie like geometries of traps like the Sandia High Optical Access (HOA) trap, as well as traps with some novel fabrication techniques including our trap the BGA.

The BGA utilizes trench capacitors, which are located directly under each electrode and go down to a ball which is bump bonded onto the carrier. This configuration means the raised trapping structure can be very small. The BGA is only $0.4 \times 1.1 \times 3.3$ mm in extent, and the surface is essentially only populated with the trapping electrodes. In principle this means that we can get tightly focused beams across the surface, but this is not the case in practice due to an oversight in design. The carrier which routes out electric connections is still too large, and the trap is not tall enough. The smallest spot sizes we can achieve with our 355 nm laser are approximately 8 μm.

In the future, we plan to move to the Sandia HOA trap which has both a high NA$\approx$ 0.2 from the side as well as a slot through the trap that has an NA$\approx$ 0.6. This will allow us to get beams focused down to 1 μm, at which point we should be able to individually address ions in the chain.

Chapter 4: Coherent Operations

In this chapter I want to go through the atom-light interactions. To coherently manipulate the spin state of the ions, we use stimulated Raman transitions. If we so choose, we can align these beams to have a net $\delta\boldsymbol{k}$ momentum transfer along one of the principal axes of the trap allowing us to couple to not only the spin degree of freedom but also the external degrees of freedom.

4.1 Raman Interaction

Consider a three level atom described by two ground states $|0\rangle$,$|1\rangle$, and one excited state $|e\rangle$. Leaving out the motion for a moment, choose the $|0\rangle$ as the zero energy level, $\langle 0|\hat{H}_0|0\rangle = 0$. Then we can write down an ion Hamiltonian of the form,

$$\hat{H}_0 = \hbar\omega_1 |1\rangle\langle 1| + \hbar\omega_e |e\rangle\langle e| \tag{4.1}$$

With an arbitrary wavefunction,

$$|\psi\rangle = c_0 |0\rangle + c_1 |1\rangle + c_e |e\rangle \tag{4.2}$$

To couple states $|0\rangle$ and $|1\rangle$ with light from two beams, the electric fields of these beams takes the following form.

$$\begin{aligned}
\boldsymbol{E_1} &= \frac{1}{2}\boldsymbol{E_{01}} e^{-i(\omega_{L1}t+\phi_1)} + h.c. && (4.3)\\
&= \frac{1}{2}\mathcal{E}_1 \hat{\boldsymbol{\epsilon}}_{\boldsymbol{1}} e^{-i(\omega_{L1}t+\phi_1)} + h.c. = \frac{1}{2}\mathcal{E}_1 \Phi_{L1} \hat{\boldsymbol{\epsilon}}_{\boldsymbol{1}} + h.c. && (4.4)\\
\boldsymbol{E_2} &= \frac{1}{2}\boldsymbol{E_{02}} e^{-i(\omega_{L2}t+\phi_2)} + h.c. && (4.5)\\
&= \frac{1}{2}\mathcal{E}_2 \hat{\boldsymbol{\epsilon}}_{\boldsymbol{2}} e^{-i(\omega_{L2}t+\phi_2)} + h.c. = \frac{1}{2}\mathcal{E}_2 \Phi_{L2} \hat{\boldsymbol{\epsilon}}_{\boldsymbol{2}} + h.c. && (4.6)\\
& && (4.7)
\end{aligned}$$

The vector amplitudes, $\boldsymbol{E_{01}}$ and$\boldsymbol{E_{02}}$, include a polarization vector, and the frequencies of the beams are such that one laser couples $|0\rangle \leftrightarrow |e\rangle$ with an arbitrary detuning δ on top of a large detuning Δ_0. The other laser couples $|1\rangle \leftrightarrow |e\rangle$ with a frequency similarly far detuned, minus the splitting between the two ground states $|1\rangle$ and $|0\rangle$.

Explicitly, we have the frequencies, $\omega_{L1} = \omega_e + \Delta_0 - \delta$ and $\omega_{L2} = \omega_e - \omega_1 + \Delta_0$. We have also absorbed the position of the ions relative to the incident field into the phases $\phi_{1,2}$; this position will allow us to couple to the external degrees of freedom of the ion chain and will be discussed later in this chapter.

The coupling between states $|0\rangle \leftrightarrow |e\rangle$ and $|1\rangle \leftrightarrow |e\rangle$ is mediated by these two beams, and takes the form of an electric dipole transition.

$$\langle i| \hat{H}_I |e\rangle = -\langle i| \boldsymbol{\mu} \cdot \boldsymbol{E_j} |e\rangle \tag{4.8}$$

$$= -\langle i| \boldsymbol{\mu} \cdot \boldsymbol{\hat{\epsilon}_j} |e\rangle \mathcal{E}_j \tag{4.9}$$

$$\langle i| \boldsymbol{\mu}_i \cdot \boldsymbol{\hat{\epsilon}_j} |e\rangle = \langle e| \boldsymbol{\mu}_i \cdot \boldsymbol{\hat{\epsilon}_j^*} |i\rangle \tag{4.10}$$

$$\boldsymbol{\mu}_i \cdot \boldsymbol{\hat{\epsilon}_j} = \mu_{i,e_j} \mathcal{E}_j |i\rangle \langle e| \tag{4.11}$$

$$\boldsymbol{\mu}_i \cdot \boldsymbol{\hat{\epsilon}_j^*} = \mu_{i,e_j}^* \mathcal{E}_j^* |i\rangle \langle e| \tag{4.12}$$

Where μ_{i,e_j} is related to a reduced dipole matrix element between states $|i\rangle$ and $|e\rangle$ for the jth beam, $\mathcal{E}_j$ and ϵ_j are the electric field amplitude and the polarization of the jth beam, we will look at these terms in depth in section 4.1.2. Equations 4.10-4.12 are a consequence of requiring Herminicity in the interaction Hamiltonian. This gives us an atom-light interaction Hamiltonian of the following form,

$$\hat{H}_I = -\boldsymbol{\hat{\mu}} \cdot \boldsymbol{E} \tag{4.13}$$

$$= -\left(\boldsymbol{\hat{\mu}_0} + \boldsymbol{\hat{\mu}_1}\right) \cdot \left(\boldsymbol{E_2} + \boldsymbol{E_1}\right) \tag{4.14}$$

$$= -\frac{1}{2}\left(\boldsymbol{\hat{\mu}_0} + \boldsymbol{\hat{\mu}_1}\right) \cdot \left(\mathcal{E}_2 \Phi_{L2} \boldsymbol{\hat{\epsilon}_2} + \mathcal{E}_1 \Phi_{L1} \boldsymbol{\hat{\epsilon}_1} + h.c.\right) \tag{4.15}$$

where we have grouped all of the phases together in the terms Φ_i, and we have broken out the individual polarization operators. We save the discussion of these parameters for a later section detailing $^{171}\text{Yb}^+$ specific parameters. Expanding equation 4.15, we get

$$\hat{\boldsymbol{\mu}} \cdot \boldsymbol{E} = \frac{1}{2}\left(\hat{\boldsymbol{\mu}}_{\mathbf{0}} + \hat{\boldsymbol{\mu}}_{\mathbf{1}}\right) \cdot \left(\mathcal{E}_2 \Phi_{L2} \hat{\boldsymbol{\epsilon}}_{\mathbf{2}} + \mathcal{E}_1 \Phi_{L1} \hat{\boldsymbol{\epsilon}}_{\mathbf{1}} + h.c.\right) \tag{4.16}$$

$$= \frac{1}{2}\hat{\boldsymbol{\mu}}_{\mathbf{0}} \cdot \left(\mathcal{E}_1 \Phi_{L1} \hat{\boldsymbol{\epsilon}}_{\mathbf{1}} + \mathcal{E}_1^* \Phi_{L1}^* \hat{\boldsymbol{\epsilon}}_{\mathbf{1}}^{\boldsymbol{*}}\right) + \frac{1}{2}\hat{\boldsymbol{\mu}}_{\mathbf{0}} \cdot \left(\mathcal{E}_2 \Phi_{L2} \hat{\boldsymbol{\epsilon}}_{\mathbf{2}} + \mathcal{E}_2^* \Phi_{L2}^* \hat{\boldsymbol{\epsilon}}_{\mathbf{2}}^{\boldsymbol{*}}\right) \tag{4.17}$$

$$+ \frac{1}{2}\hat{\boldsymbol{\mu}}_{\mathbf{1}} \cdot \left(\mathcal{E}_1 \Phi_{L1} \hat{\boldsymbol{\epsilon}}_{\mathbf{1}} + \mathcal{E}_1^* \Phi_{L1}^* \hat{\boldsymbol{\epsilon}}_{\mathbf{1}}^{\boldsymbol{*}}\right) + \frac{1}{2}\hat{\boldsymbol{\mu}}_{\mathbf{1}} \cdot \left(\mathcal{E}_2 \Phi_{L2} \hat{\boldsymbol{\epsilon}}_{\mathbf{2}} + \mathcal{E}_2^* \Phi_{L2}^* \hat{\boldsymbol{\epsilon}}_{\mathbf{2}}^{\boldsymbol{*}}\right) \tag{4.18}$$

To determine the population dynamics of an arbitrary state, we substitute our interaction Hamiltonian into the Schrödinger equation, $i\hbar\dot{\psi} = H\psi = (H_0 + H_I)\psi$. For convenience we set $\hbar = 1$ and solve the Schrödinger equation under some simplifying assumptions. Solving for the individual probability amplitudes, c_i, the resulting time evolution is governed by,

$$i\dot{c}_0 = -\frac{1}{2}\left(\mu_{0e_1}^* \mathcal{E}_1^* \Phi_{L1}^* + \mu_{0e_1} \mathcal{E}_1 \Phi_{L1}\right) c_e \tag{4.19}$$

$$i\dot{c}_1 = \omega_1 c_1 - \frac{1}{2}\left(\mu_{1e_1} \mathcal{E}_1 \Phi_{L1} + \mu_{1e_2} \mathcal{E}_2 \Phi_{L2}\right) c_e \tag{4.20}$$

$$i\dot{c}_e = \omega_e c_e - \frac{1}{2}\left(\mu_{0e_1}^* \mathcal{E}_1^* \Phi_{L1}^* + \mu_{0e_2}^* \mathcal{E}_2^* \Phi_{L2}^*\right) c_0 - \frac{1}{2}\left(\mu_{1e_1}^* \mathcal{E}_1^* \Phi_{L1}^* + \mu_{1e_2}^* \mathcal{E}_2^* \Phi_{L2}^*\right) c_1 \tag{4.21}$$

To make the following calculations a little less cumbersome, we will define the single photon coupling rates for each of the transitions in the following way,

$$g_{0e_1} = -\mu_{0e_1}\mathcal{E}_1 e^{-i\phi_1} \tag{4.22}$$

$$g_{0e_2} = -\mu_{0e_2}\mathcal{E}_2 e^{-i\phi_2} \tag{4.23}$$

$$g_{1e_1} = -\mu_{1e_1}\mathcal{E}_1 e^{-i\phi_1} \tag{4.24}$$

$$g_{1e_2} = -\mu_{1e_2}\mathcal{E}_2 e^{-i\phi_2} \tag{4.25}$$

We can simplify the effects of multiple beams by writing the generalized coupling as $g_{ik_j} = -\mu_{ik_j}\mathcal{E}_j e^{-i\phi_j}$, where j is an index the beam, and i and k index the coupled states. The coupled equations for the population dynamics then become,

$$i\dot{c}_0 = \frac{1}{2}\sum_{j=1}\left(g_{0e_j}e^{-i\omega_{Lj}t} + g^*_{0e_j}e^{i\omega_{Lj}t}\right)c_e \tag{4.26}$$

$$i\dot{c}_1 = \omega_1 c_1 + \frac{1}{2}\sum_{j=1}\left(g_{1e_j}e^{-i\omega_{Lj}t} + g^*_{1e_j}e^{i\omega_{Lj}t}\right)c_e \tag{4.27}$$

$$i\dot{c}_e = \omega_e c_e + \frac{1}{2}\sum_{j=1}\left[\left(g_{0e_j}e^{-i\omega_{Lj}t} + g^*_{0e_j}e^{i\omega_{Lj}t}\right)c_0 + \left(g_{1e_j}e^{-i\omega_{Lj}t} + g^*_{1e_j}e^{i\omega_{Lj}t}\right)c_1\right] \tag{4.28}$$

We can simplify these equations by moving to the frame rotating with respect to the un-perturbed Hamiltonian. We apply the following transformation to our system of coupled equations,

$$c_0 = \tilde{c}_0 \tag{4.29}$$

$$c_1 = \tilde{c}_1 e^{-i\omega_1 t} \tag{4.30}$$

$$c_e = \tilde{c}_e e^{-i\omega_e t} \tag{4.31}$$

This will remove all of the stationary terms from this Hamiltonian leaving us with the following evolution.

$$i\dot{\tilde{c}}_0 = \frac{1}{2}\sum_{j=1}^{m}\left(g_{0e_j} e^{-i(\omega_{Lj}+\omega_e)t} + g^*_{0e_j} e^{-i\Delta_{e_j} t}\right)\tilde{c}_e \tag{4.32}$$

$$i\dot{\tilde{c}}_1 = \frac{1}{2}\sum_{j=1}^{m}\left(g_{1e_j} e^{-i(\omega_{Lj}+\omega_e-\omega_1)t} + g^*_{1e_j} e^{-i(\Delta j-\omega_1)t}\right)\tilde{c}_e \tag{4.33}$$

$$i\dot{\tilde{c}}_e = \frac{1}{2}\sum_{j=1}^{m}\left[\left(g_{0e_j} e^{i\Delta_{e_j} t} + g^*_{0e_j} e^{i(\omega_j+\omega_e)t}\right)\tilde{c}_0 + \left(g_{1e_j} e^{i(\Delta_{e_j}-\omega_1)t} + g^*_{1e_j} e^{i(\omega_j+\omega_e-\omega_1)t}\right)\tilde{c}_1\right] \tag{4.34}$$

Where we have defined detuning frequencies for either beam, $\Delta_{e_1} = \omega_e - \omega_{L1} = \delta - \Delta_0$ and $\Delta_{e_2} = \omega_e - \omega_{L2} = \omega_1 - \Delta_0$. The relative rates of all of these terms is $\delta \ll \omega_1 \ll \Delta_{e_j} \ll \omega_e$. After the integration, these terms will pick up factors of $\frac{1}{\omega}$. Therefore we can make the so-called rotating wave approximation (RWA) and assume that all terms which rotate with a total frequency $\omega > \Delta_{e_j}$ will average to zero. By moving into a rotating frame and making the rotating wave approximation to remove terms rotating faster than Δ_{e_j}, we can get equations of the form,

$$i\dot{\tilde{c}}_0 = \frac{1}{2}\sum_{j=1}^{m} g^*_{0e_j} e^{-i\Delta_{e_j}t}\tilde{c}_e \tag{4.35}$$

$$i\dot{\tilde{c}}_1 = \frac{1}{2}\sum_{j=1}^{m} g^*_{1e_j} e^{-i(\Delta j-\omega_1)t}\tilde{c}_e \tag{4.36}$$

$$i\dot{\tilde{c}}_e = \frac{1}{2}\sum_{j=1}^{m} \left[g_{0e_j} e^{i\Delta_{e_j}t}\tilde{c}_0 + g_{1e_j} e^{i(\Delta_{e_j}-\omega_1)t}\tilde{c}_1\right] \tag{4.37}$$

We want to eliminate the excited state $|e\rangle$ from these equations, which can be accomplished through adiabatic elimination. This is an approximation which will allows us to find an approximate form for $\tilde{c}_e$ through direct integration, where we consider all the population to be found in $\tilde{c}_e = 0$ at $t = 0$. To be valid we need the time dependence of $\dot{\tilde{c}}_e$ to be dominated by $e^{-i\Delta_{e_j}t}$ so that $\tilde{c}_0$ and $\tilde{c}_1$ can be considered constant and move outside the integrand. This will be a valid approximation as long as the ground states are sufficiently decoupled from the excited state, if the detuning from the excited state is large then this approximation remains valid. Performing the integration with this assumption gives,

$$\tilde{c}_e = \frac{1}{2}\sum_{j=1}^{m} \left[\frac{g_{0e_j}\left(1-e^{i\Delta_{e_j}t}\right)}{\Delta_{e_j}}\tilde{c}_0 + \frac{g_{1e_j}\left(1-e^{i(\Delta_{e_j}-\omega_1)t}\right)}{\Delta_{e_j}-\omega_1}\tilde{c}_1\right] \tag{4.38}$$

The amplitude, c_e, can now be eliminated from the coupled differential equations leaving us with a coupled two-state system. This is the result we are after, we have coupled the two ground states via the excited state without any population residing in the, presumably short lived, excited state. In practice, this type of coupling allows us to drive population between two long lived ground states without the decoherence associated with spontaneous emission. In the case of $^{171}\mathrm{Yb}^+$, these ground states can be the clock states of the $^2S_{1/2}$ hyperfine manifold which can maintain a long coherence time between each other [32]. At this point we are left with.

$$i\dot{\tilde{c}}_0 = \sum_{j=1}^{m}\left[\frac{|g_{0e_j}|^2\left(e^{-i\Delta_{e_j}t}-1\right)}{4\Delta_{e_j}}\tilde{c}_0 + \frac{g^*_{0e_j}g_{1e_j}\left(e^{-i\Delta_{e_j}t}-e^{-i\omega_1 t}\right)}{4(\Delta_{e_j}-\omega_1)}\tilde{c}_1\right] \tag{4.39}$$

$$i\dot{\tilde{c}}_1 = \sum_{j=1}^{m}\left[\frac{g_{0e_j}g^*_{1e_j}\left(e^{i\left(\Delta_{e_j}-\omega_1\right)t}-e^{-i\omega_1 t}\right)}{4\Delta_{e_j}}\tilde{c}_0 + \frac{|g_{1e_j}|^2\left(e^{i\left(\Delta_{e_j}-\omega_1\right)t}-1\right)}{4(\Delta_{e_j}-\omega_1)}\tilde{c}_1\right] \tag{4.40}$$

From earlier, we know that $\Delta_{e_j} \gg \omega_1$, and so we can make the approximation that $\Delta_{e_j} - \omega_1 \approx \Delta_{e_j}$. If we once again make a RWA, we can eliminate nearly all of the time dependence,

$$i\dot{\tilde{c}}_0 = \sum_{j=1}^{m}\left[-\frac{|g_{0e_j}|^2}{4\Delta_{e_j}}\tilde{c}_0 - \frac{g^*_{0e_j}g_{1e_j}e^{-i\omega_1 t}}{4(\Delta_{e_j}-\omega_1)}\tilde{c}_1\right] \tag{4.41}$$

$$i\dot{\tilde{c}}_1 = \sum_{j=1}^{m}\left[-\frac{g_{0e_j}g^*_{1e_j}e^{-i\omega_1 t}}{4\Delta_{e_j}}\tilde{c}_0 - \frac{|g_{1e_j}|^2}{4(\Delta_{e_j}-\omega_1)}\tilde{c}_1\right] \tag{4.42}$$

By transforming back to the lab frame from the rotating frame we have been working in, $\tilde{c}_0 = c_0$ and $\tilde{c}_1 = c_1 e^{i\omega_1 t}$ and we can remove the final piece of time dependence from these equations,

$$i\dot{c}_0 = \sum_{j=1}^{m}\left[-\frac{|g_{0e_j}|^2}{4\Delta_{e_j}}c_0 - \frac{g_{0e_j}^{*}g_{1e_j}}{4(\Delta_{e_j}-\omega_1)}c_1\right] \tag{4.43}$$

$$i\dot{c}_1 = \sum_{j=1}^{m}\left[-\frac{g_{0e_j}g_{1e_j}^{*}}{4\Delta_{e_j}}c_0 - \left(\omega_1 - \frac{|g_{1e_j}|^2}{4(\Delta_{e_j}-\omega_1)}\right)c_1\right] \tag{4.44}$$

At this point it is convenient to re-label the on-diagonal and off-diagonal terms of the coupled system. The on-diagonal elements correspond to AC Stark shifts induced by the off resonant coupling Raman laser. The off-diagonal elements give the effective coupling or Rabi rate between the two levels. We parametrize these two effects by

$$\delta_{l0} = \sum_{j=1}^{m}\frac{|g_{0e_j}|^2}{4\Delta_{e_j}} \tag{4.45}$$

$$\delta_{l1} = \sum_{j=1}^{m}\frac{|g_{1e_j}|^2}{4(\Delta_{e_j}-\omega_1)} \tag{4.46}$$

$$\Omega = \sum_{j=1}^{m}\frac{g_{0e_j}^{*}g_{1e_j}}{2\Delta_{e_j}} \tag{4.47}$$

The system of equations 4.43-4.44 can be recast in matrix form with an effective Hamiltonian,

$$i\frac{\partial}{\partial t}\begin{pmatrix} c_0 \\ c_1 \end{pmatrix} = \begin{pmatrix} -\delta_{l0} & -\frac{\Omega}{2} \\ -\frac{\Omega^*}{2} & \omega_1 - \delta_{l1} \end{pmatrix} \cdot \begin{pmatrix} c_0 \\ c_1 \end{pmatrix} \tag{4.48}$$

This gives us an effective model for Raman coupling via an excited state, now we need to extend this model to include the effects of multiple excited states. This will allow us to calculate effective Rabi rates from reduced dipole matrix elements. In later sections we will dive into calculations of these parameters for specific $^{171}\mathrm{Yb}^{+}$ couplings.

4.1.1 Pulsed Raman Interaction

In practice, we drive the Raman transitions described above with a pulsed laser. Briefly, let us look at how this difference affects the above derivation. It is worth noting that a lot of the work is already done for us, we performed the above derivation for two beams, in fact we can extend the above sums to any number of beams. However we must consider the modification to the spectrum of the above coupling lasers. Lets consider the changes to the electric field,

$$\begin{aligned}
\boldsymbol{E_1}(t) &= \frac{1}{2}\boldsymbol{E_{01}}e^{-i(\omega_{L1}t+\phi_1)} + h.c. && (4.49)\\
&= \frac{1}{2}\mathcal{E}(t)_1\boldsymbol{\hat{\epsilon}_1}e^{-i(\omega_{L1}t+\phi_1)} + h.c. && (4.50)\\
&= \frac{1}{2}\mathcal{E}_1\sum_n f(t-nT)e^{-i(\omega_{L1}t+\phi_1)} + h.c. && (4.51)
\end{aligned}$$

This is a sum over pulses from the laser in the time domain where T is the time between subsequent pulses [44]. Where f is the functional form of the pulse, in practice this is $\mathrm{sech}^3(t)$, however, this will not be relavent for our discussion. If we say the ions will interact with many pulses by taking a Fourier transform we can look at the frequency components of this laser pulse,

$$\boldsymbol{E_1}(\omega) = \frac{1}{2}\mathcal{E}_1 \sum_j f(j\omega_{rep}) e^{-i[(\omega_{L1}+j\omega_{rep})t+\phi_j]} + h.c. \tag{4.52}$$

Where we have absorbed the different $\boldsymbol{k_j}$ vectors into phases,ϕ_j, just as before. Our generalized g_{ik_j} is still valid, and by following the derivation from the previous section we come to the same results,

$$\delta_{l0} = \sum_j \frac{|g_{0e_j}|^2}{4\Delta_{e_j}} \tag{4.53}$$

$$\delta_{l1} = \sum_j \frac{|g_{1e_j}|^2}{4(\Delta_{e_j} - \omega_1)} \tag{4.54}$$

$$\Omega = \sum_j \frac{g^*_{0e_j} g_{1e_j}}{2\Delta_{e_j}} \tag{4.55}$$

However, now the sum over j is over all spectral components of the pulse, and the Δ_{e_j} detunings contain frequencies at intervals of the repetition rate of the laser, $\Delta_{e_j} = \omega_e - \omega_{L1} = \delta - \Delta_0 + j\omega_{rep}$.

4.1.2 Yb Ion Coupling

It is necessary now to extend our model to include the effects of the other coupled levels in $^{171}\text{Yb}^+$. For the case of $^{171}\text{Yb}^+$ the 355 nm Raman lasers will coupled the $^2S_{1/2}\,|F=0, m_F=0\rangle$ and $|F=1, m_F=0\rangle$ to the excited state hyperfine manifolds $^2P_{1/2}\,|F=1\rangle$, $^2P_{3/2}\,|F=1\rangle$, and $^2P_{3/2}\,|F=2\rangle$. In general, we can extend the form of our couplings to include any number of excited states by introducing a sum over these excited states

$$\delta_{l0} = \sum_{k\in|e_i\rangle}\sum_{j}\frac{|g_{0k_j}|^2}{4\Delta_{k_j}} \tag{4.56}$$

$$\delta_{l1} = \sum_{k\in|e_i\rangle}\sum_{j}\frac{|g_{1k_j}|^2}{4(\Delta_{k_j}-\omega_1)} \tag{4.57}$$

$$\Omega = \sum_{k\in|e_i\rangle}\sum_{j}\frac{g^*_{0k_j}g_{1k_j}}{2\Delta_{k_j}} \tag{4.58}$$

To calculate any of these parameters, the dipole matrix element embedded with the g_{ik_j} terms must be evaluated. By using the Wigner-Eckart theorem we can calculate these matrix elements in terms of ClebschGordan coefficients and reduced dipole matrix elements, which can then be evaluated with known quantities.

$$g_{ik_j} = -\mu_{ik_j}\mathcal{E}_j e^{-i\phi_j} \tag{4.59}$$

$$\mu_{ik_j} = \langle i|\, \boldsymbol{\mu}\cdot\boldsymbol{\hat{\epsilon}_j}\, |e\rangle \tag{4.60}$$

$$= \langle i|\, \hat{T}^1_q\, |e\rangle \tag{4.61}$$

By making use of 3-J and 6-J symbols we can come up with a form of these matrix elements which only require knowledge about the J angular momentum couplings [47]. Note that $\boldsymbol{\mu}\cdot\boldsymbol{\hat{\epsilon}_j} = \sum_q \hat{T}^\kappa_q$, for single photon coupling $\kappa = 1$. The value of q depends on the polarization of the coupling laser, $\hat{\epsilon}_{\sigma^+} \to q = 1$, $\hat{\epsilon}_{\sigma^-} \to q = -1$, and $\hat{\epsilon}_\pi \to q = 0$, we can sum over all polarizations and explicitly we find

$$\langle i|\,\hat{T}^1_q\,|e\rangle = \sum_q \langle J', F', m'_F|\,\hat{T}^1_q\,|J, F, m_F\rangle \tag{4.62}$$

$$= \frac{\langle J', F'|\,|\hat{T}^1|\,|J, F\rangle}{\sqrt{2J'+1}} \sum_q \langle F, m_F, 1, q|F', m'_F\rangle \tag{4.63}$$

$$= (-1)^{-F+1-m'_F} \sum_q \begin{pmatrix} F & 1 & F' \\ m_F & q & -m'_F \end{pmatrix} \langle J', F'|\,|\hat{T}^1|\,|J, F\rangle \tag{4.64}$$

$$= (-1)^{-J'+I-m'_F} \sqrt{(2F+1)(2F'+1)} \sum_q \begin{pmatrix} F & 1 & F' \\ m_F & q & -m'_F \end{pmatrix} \begin{Bmatrix} J' & F' & I \\ F & J & 1 \end{Bmatrix} \langle J'|\,|\hat{T}^1|\,|J\rangle \tag{4.65}$$

$$= \sum_q C(J', F', m'_F, J, F, m_F, I, q)\,\langle J'|\,|\hat{T}^1|\,|J\rangle \tag{4.66}$$

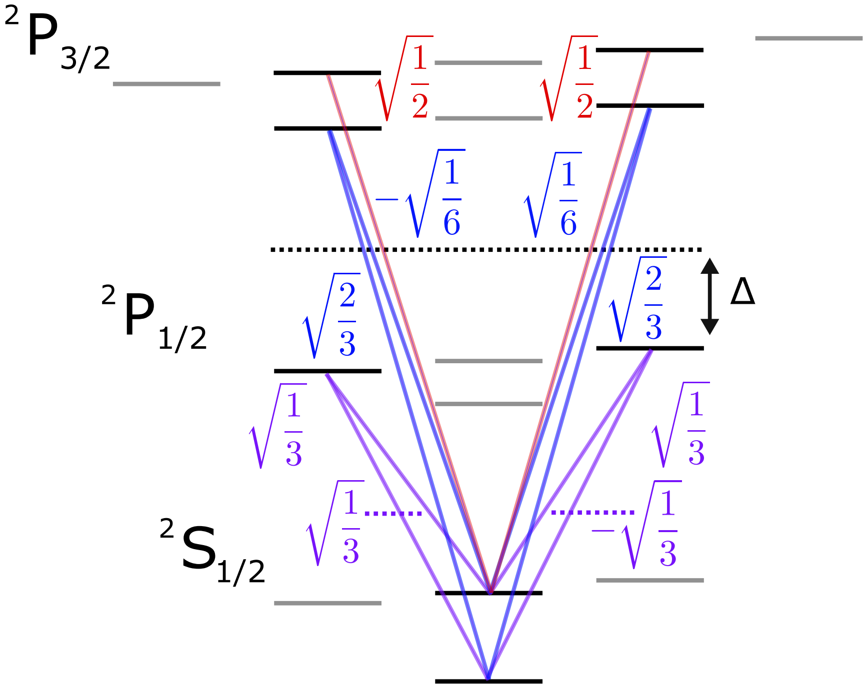

Figure 4.1: The coupling coefficents given by ClebschGordan coefficients for the relevant transitions in $^{171}Yb^{+}$.

The values of the 6-j and 3-j symbols are readily calculated from Clebsch-

Gordon coefficients, or by using built-in functionality in programs like Mathematica. By using Fermi's golden rule, we can calculate a value for the reduced matrix element $\langle J'| |\hat{T}^1| |J\rangle$ in terms of experimentally relevant parameters.

$$|\langle J'| |\mu| |J\rangle|^2 = \frac{3\hbar c^3}{4\omega_0^3}(2J'+1)B_i\Gamma_0 \tag{4.67}$$

Where once again, B_i is the branching ratio. We can equate this parameter to the saturation intensity of the transition with the previously defined equation

$$\begin{align} I_{sat} &= \frac{\pi h c \Gamma_0}{3\lambda^3 B} \tag{4.68} \\ &= \frac{\hbar\omega_0^3\Gamma_0}{12\pi c^2 B} \tag{4.69} \\ I &= \frac{c\mathcal{E}^2}{8\pi} \tag{4.70} \end{align}$$

We can use these expressions to write the above coupling rate g in terms of the intensity of the individual beams,

$$\begin{align} g_{ik_j} &= -\mu_{ik_j}\mathcal{E}_j e^{-i\phi_j} \tag{4.71} \\ &= -\mathcal{E}_j e^{-i\phi_j}\sum_q C(J',F',m'_F,J,F,m'_F,q)\sqrt{\frac{3\hbar c^3}{4\omega_0^3}(2J'+1)B_i\Gamma_0} \tag{4.72} \\ &= -\sum_q C(J',F',m'_F,J,F,m'_F,q)\sqrt{(2J'+1)}\Gamma_0\sqrt{\frac{I}{2I_{sat}}}e^{-i\phi_j} \tag{4.73} \\ &= -\Gamma_0\sqrt{\frac{I}{2I_{sat}}}e^{-i\phi_j}\sum_q \tilde{C}_{ikq} \tag{4.74} \end{align}$$

This derivation allows us to compare relative coupling rates from the various levels to various beams given their intensities and polarizations, parameters which are routinely controlled in the lab. Putting everything together we get,

$$\delta_{l0} = \sum_{k=|e\rangle} \sum_{j=1}^{m} \frac{\hbar\Gamma_k^2}{4\Delta_{k_j}} \frac{I_j}{2I_{sat}} \tilde{C}_{0kq}^2 \tag{4.75}$$

$$\delta_{l1} = \sum_{k=|e\rangle} \sum_{j=1}^{m} \frac{\hbar\Gamma_k^2}{4(\Delta_{k_j} - \omega_1)} \frac{I_j}{2I_{sat}} \tilde{C}_{1kq}^2 \tag{4.76}$$

$$\Omega = \sum_{k=|e\rangle} \sum_{j=1}^{m} \frac{\hbar\Gamma_k^2}{2\Delta_{k_j}} \frac{I_j}{2I_{sat}} \tilde{C}_{1kq}\tilde{C}_{0kq} \tag{4.77}$$

At this point we have calculated all the relevant parameters to coherently drive stimulated Raman transitions with a pulsed laser between the hyperfine ground states of $^{171}\mathrm{Yb}^{+}$. We can use this coupling to drive coherent dynamics between the $|F = 1, m_F = 0\rangle$ and $|F = 0, m_F = 0\rangle$ ground states for many oscillation periods. The next section will cover how we use these same interactions to coherently address the external phonon degrees of freedom.

4.1.3 Raman Coupling with Normal Modes

Once again start with the bare Hamiltonian for our three level system, but now must consider the confining potential. The motion of the ion in the harmonic potential will dress the internal degrees of freedom, and we get a Hamiltonian of the form[1],

---

[1] We have set $\hbar = 1$ for convenience in this section.

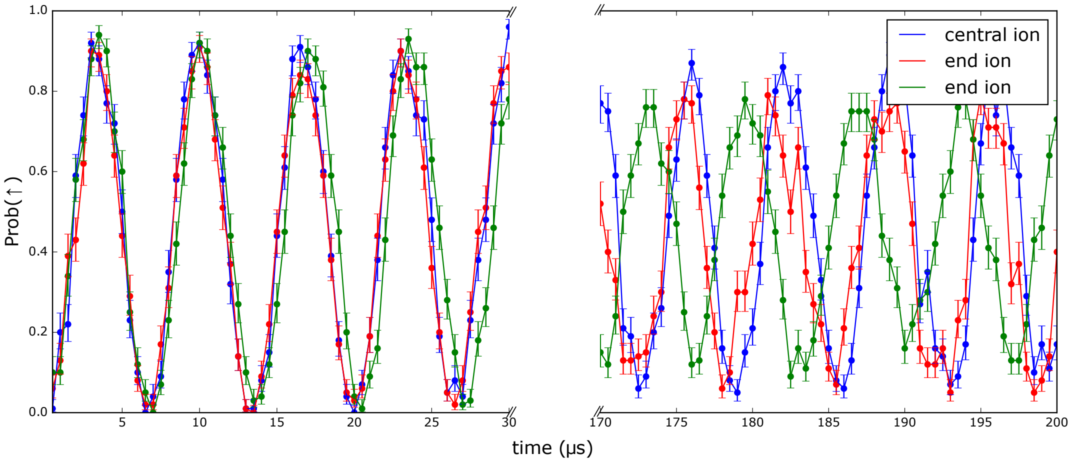

Figure 4.2: Rabi flops were performed with three ions trapped, by locking the beatnote of the laser such that two comb teeth interfere to bridge the ground state hyperfine splitting of $^{171}\text{Yb}^{+}$. We can coherently drive transitions between these two levels for more than 20 flips. The phase jumps in the later flops we believe are the result of air currents causing pointing instabilities. The error bars on this plot depict a 1 σ confidence interval. This interval was calculated using the Clapper-Pearson interval [48] for binomially distributed Bernoulli trials. This should give an overly conservative estimate of the error bars. Error bars will be calculated in a similar fashion throughout this thesis.

$$\hat{H}_0 = \sum_i^2 \omega_e \left|e\right\rangle_i \left\langle e\right|_i + \omega_1 \left|1\right\rangle_i \left\langle 1\right|_i + \omega_a(\hat{a}^\dagger \hat{a} + \frac{1}{2}) + \omega_b(\hat{b}^\dagger \hat{b} + \frac{1}{2}) \tag{4.78}$$

Where $\hat{b}^\dagger$ and $\hat{a}^\dagger$ are creation operators for phonons on modes a and b, where $\hat{b}$ and $\hat{a}$ are destruction operators for phonons on these modes. We now want to apply our radiation fields to couple the two ground states via the excited state. This perturbation can be written as follows, Where we will no longer hide the position phase dependence. The positions x are the positions of the individual ions which yields,

$$\hat{H}_I = \sum_{i}^{2} E_1 \left|e\right\rangle_i \left\langle 0\right|_i e^{-i\omega_{L1}t} e^{i\boldsymbol{k}_1\boldsymbol{x}_i} + E_2 \left|e\right\rangle_i \left\langle 1\right|_i e^{-i\omega_{L2}t} e^{i\boldsymbol{k}_2\boldsymbol{x}_i} + h.c. \tag{4.79}$$

If we move to the interaction picture to remove the stationary terms of the Hamiltonian, similar to our rotating frame from before, we will rotate with respect to energy eigenstates of the unperturbed Hamiltonian. This is equivalent to the transformation.

$$\begin{aligned}
\hat{\hat{H}}_I =& \hat{U}_0^\dagger \hat{H}_I \hat{U}_0 = e^{i\hat{H}_0 t} \hat{H}_I e^{-i\hat{H}_0 t} && (4.80) \\
=& E_1 \left|e\right\rangle_1 \left\langle 0\right|_1 e^{i(\omega_e-\omega_{L1})t} e^{i\boldsymbol{k}_1\cdot[\boldsymbol{x}_{0a}(\hat{a}^\dagger e^{i\omega_a t}+\hat{a}e^{-i\omega_a t})+\boldsymbol{x}_{0b}(\hat{b}^\dagger e^{i\omega_b t}+\hat{b}e^{-i\omega_b t})]} && (4.81) \\
&+ E_1 \left|e\right\rangle_2 \left\langle 0\right|_2 e^{i(\omega_e-\omega_{L1})t} e^{i\boldsymbol{k}_1\cdot[\boldsymbol{x}_{0a}(\hat{a}^\dagger e^{i\omega_a t}+\hat{a}e^{-i\omega_a t})-\boldsymbol{x}_{0b}(\hat{b}^\dagger e^{i\omega_b t}+\hat{b}e^{-i\omega_b t})]} \\
&+ E_2 \left|e\right\rangle_1 \left\langle 1\right|_1 e^{i(\omega_e-\omega_1-\omega_{L2})t} e^{i\boldsymbol{k}_2\cdot[\boldsymbol{x}_{0a}(\hat{a}^\dagger e^{i\omega_a t}+\hat{a}e^{-i\omega_a t})+\boldsymbol{x}_{0b}(\hat{b}^\dagger e^{i\omega_b t}+\hat{b}e^{-i\omega_b t})]} \\
&+ E_2 \left|e\right\rangle_2 \left\langle 1\right|_2 e^{i(\omega_e-\omega_{L2})t} e^{i\boldsymbol{k}_2\cdot[\boldsymbol{x}_{0a}(\hat{a}^\dagger e^{i\omega_a t}+\hat{a}e^{-i\omega_a t})-\boldsymbol{x}_{0b}(\hat{b}^\dagger e^{i\omega_b t}+\hat{b}e^{-i\omega_b t})]} + h.c.
\end{aligned}$$

An important point to note here is that spin operators on different ions have the same sign but different signs with respect to the normal modes. This is the case because we have made the substitution, $\boldsymbol{x}_1 = \hat{x}_a + \hat{x}_b$ and $\boldsymbol{x}_2 = \hat{x}_a - \hat{x}_b$, which transforms from real space ion coordinates, $\boldsymbol{x}_1$ and $\boldsymbol{x}_2$, to normal mode coordinates, $\boldsymbol{x}_a$ and $\boldsymbol{x}_b$. The corresponding operators can be written as $\hat{x}_a = \hat{x}_{0a}(\hat{a}^\dagger + \hat{a})$ and $\hat{x}_b = \hat{x}_{0b}(\hat{b}^\dagger + \hat{b})$. Where $\hat{x}_{0b}$ and $\hat{x}_{0a}$ are the amplitudes of zero point motion for either mode. These are defined as $\hat{x}_{0i} = \sqrt{\frac{\hbar}{2m\omega_i}}$. The amplitudes, which in principle depend on the normal mode frequencies, we will wrap up in a Lambe-Dicke parameter, defined as the dot product of momentum vector and the zero point motion of a given mode, $\boldsymbol{k} \cdot \boldsymbol{x_0}$. In general, we can write H_I for arbitrary numbers of ions.

$$\tilde{H}_I = \sum_j \Omega \hat{\sigma}_j^+ e^{i\omega_1 t} \prod_i e^{[i\eta_{i,j}(\hat{a}_i^\dagger e^{i\omega_i t} + \hat{a}_i e^{-i\omega_i t})]} e^{-i\omega_\Delta t} + \text{h.c.} \tag{4.82}$$

For now we will restrict the discussion to only two ions. However, by using the above general interaction Hamiltonian, the following results can easily be generalized to more ions. By considering only far detuned laser fields, we will make the same adiabtic elimination as in the previous sections (we are never driving population through the excited state), however the beatnote between our two radiation fields will drive transitions in the ground state manifold (between spin-up and spin-down). We are going to make the implicit assumption here that operators of the form $|0\rangle_i \langle 1|_j$ where $i \neq j$ are unphysical, as this would imply virtually exciting one ion to the excited state and emitting on another ion. Our Hamiltonian then becomes,

$$\begin{aligned} \hat{\tilde{H}}_I =& E_2 E_1^* |0\rangle_1 \langle 1|_1 \, e^{-i(\omega_1+\omega_2-\omega_{L1})t} e^{i\delta\boldsymbol{k}_1 \cdot [\boldsymbol{x}_{0,a}(\hat{a}^\dagger e^{i\omega_a t} + \hat{a} e^{-i\omega_a t}) + \boldsymbol{x}_{0,b}(\hat{b}^\dagger e^{i\omega_b t} + \hat{b} e^{-i\omega_b t})]} \\ &+ E_2 E_1^* |0\rangle_2 \langle 1|_2 \, e^{-i(\omega_1+\omega_2-\omega_{L1})t} e^{i\delta\boldsymbol{k}_2 \cdot [\boldsymbol{x}_{0,a}(\hat{a}^\dagger e^{i\omega_a t} + \hat{a} e^{-i\omega_a t}) - \boldsymbol{x}_{0,b}(\hat{b}^\dagger e^{i\omega_b t} + \hat{b} e^{-i\omega_b t})]} + h.c. \end{aligned} \tag{4.83}$$

This Hamiltonian represents all the coupling between spin and motion we can drive via stimulated Raman transitions. We now make the assumption that all terms $\eta_{i,m} = \delta\boldsymbol{k}_i \cdot \boldsymbol{x}_{0,m} \ll 1$, where $m \in \{a, b\}$ are normal mode indicies and $i \in \{1, 2\}$ are ion/laser indicies. This allows us to expand the exponential terms in orders of η, where we assume all η's are of similar order.

$\mathcal{O}(\eta^0)$:

$$H_{\eta^0} = (\hat{\sigma}_1^- + \hat{\sigma}_2^-)e^{-i(\omega_1+\Delta)t} + h.c. \tag{4.84}$$

$\mathcal{O}(\eta^1)$:

$$\begin{aligned} H_\eta =& i(\eta_{1,a}\hat{\sigma}_1^- + \eta_{2,a}\hat{\sigma}_2^-)(\hat{a}^\dagger + \hat{a}e^{-2i\omega_a t})e^{-i(\omega_1+\Delta-\omega_a)t} \\ &+ i(\eta_{1,b}\hat{\sigma}_1^- - \eta_{2,b}\hat{\sigma}_2^-)(\hat{b}^\dagger + \hat{b}e^{-2i\omega_b t})e^{-i(\omega_1+\Delta-\omega_b)t} + h.c. \end{aligned} \tag{4.85}$$

$\mathcal{O}(\eta^2)$:

$$\begin{aligned} H_{\eta^2} = &-(\eta_{1,a}^2\hat{\sigma}_1^- + \eta_{2,a}^2\hat{\sigma}_2^-)(\hat{a}^\dagger\hat{a}^\dagger + \hat{a}\hat{a}^\dagger e^{-2i\omega_a t} + \hat{a}^\dagger\hat{a}e^{-2i\omega_a t} + \hat{a}\hat{a}e^{-4i\omega_a t})e^{-i(\omega_1+\Delta-2\omega_a)t} \\ &-(\eta_{1,b}^2\hat{\sigma}_1^- + \eta_{2,b}^2\hat{\sigma}_2^-)(\hat{b}^\dagger\hat{b}^\dagger + \hat{b}\hat{b}^\dagger e^{-2i\omega_b t} + \hat{b}^\dagger\hat{b}e^{-2i\omega_b t} + \hat{b}\hat{b}e^{-4i\omega_b t})e^{-i(\omega_1+\Delta-2\omega_b)t} \\ &-2(\eta_{1,b}\eta_{1,a}\hat{\sigma}_1^- - \eta_{2,b}\eta_{2,a}\hat{\sigma}_2^-)(\hat{a}^\dagger\hat{b} + \hat{b}^\dagger\hat{a}(e^{2i(\delta\omega_{b,a})t} + e^{2i\omega_a t}) + \hat{a}\hat{b}e^{2i\omega_b t})e^{-i(\omega_1+\Delta+\delta\omega_{b,a})t} \\ &+ h.c. \end{aligned} \tag{4.86}$$

We have defined the spin raising and lowering operators $|\{1,0\}\rangle_i \langle\{0,1\}|_i$ as $\hat{\sigma}_i^{\{+,-\}}$, respectively, where i is once again an ion index. The detunings are defined $\Delta = \omega_{L2} - \omega_{L1}$ and $\delta\omega_{b,a} = \omega_b - \omega_a$. Although this looks rather busy, everything basically falls out with a RWA. By setting Δ to different resonance frequencies we can remove different terms just as before. We make this substitution for any of these terms and we will say anything that is rotating faster than Δ will rotate away.

Where we will now generalize to arbitrary numbers of ions. This leaves only leaves a few terms in each order of η that we will be interested in.

$\mathcal{O}(\eta^0)$: Spin flip transitions

$$\tilde{H}_I^{RWA} = \sum_j \Omega(\sigma_j^+ + \sigma_j^-) \tag{4.87}$$

$\mathcal{O}(\eta^1)$: red sideband and blue sideband transitions (RSB and BSB)

$$\tilde{H}_I^{RWA} = \sum_j \eta_{i,j}\Omega(\sigma_j^+ \hat{a}_i + \sigma_j^- \hat{a}_i^\dagger) \tag{4.88}$$

$\mathcal{O}(\eta^2)$: Mixing transitions

$$\tilde{H}_I^{RWA} = \sum_j \eta_{i,j}\eta_{k,j}\Omega(\sigma_j^+ \hat{a}_i \hat{a}_k^\dagger + \sigma_j^- \hat{a}_i^\dagger \hat{a}_k) \tag{4.89}$$

The index j is again an ion index where i and k index the modes. These terms certainly do not constitute all of the terms in the expansion of η, however they will be the only ones we are interested in. The η^0 terms drive spin-flip transitions, without coupling to the motion. The η^1 terms add or subtract motional quanta conditional on a spin-flip. Finally the η^2 terms drive interference between the normal modes conditional on a spin-flip. In the next champter I will show experimental results driving the first two terms. The third term is one that will be the subject of Chapter 6.

4.1.4 STIRAP

The final type of coherent operation that we will consider is one that we want to use for readout of the phonon states. One of the problems with reading out the phonon occupation of a given normal mode is that if we try and readout the occupation with the spin-motion coupling described in the previous section, each number state will evolve at a different rate. One way to drive all of these transitions at the same rate is to drive these transitions in the weak coupling limit through an adiabatic passage [49]. We accomplish this passage by driving stimulated Raman transitions, therefore this is known as stimulated Raman adiabatic passage (STIRAP) [50]. The coupling lasers are the same, let us consider an unperturbed Hamiltonian, $\hat{H}_0$, and coupling Hamiltonian, $\hat{H}_I$. The total Hamiltonian will have the form,

$$\hat{H}_0 = \hbar\Delta \left|e\right\rangle \left\langle e\right| + \hbar\delta \left|1\right\rangle \left\langle 1\right| \tag{4.90}$$

$$\hat{H}_I = \frac{1}{2}\hbar\Omega_P \left|0\right\rangle \left\langle e\right| + \frac{1}{2}\hbar\Omega_S \left|1\right\rangle \left\langle e\right| + h.c. \tag{4.91}$$

$$\hat{H}_{tot} = \hat{H}_0 + \hat{H}_I \tag{4.92}$$

$$= \hbar \begin{pmatrix} 0 & \frac{1}{2}\Omega_P & 0 \\ \frac{1}{2}\Omega_P & \Delta & \frac{1}{2}\Omega_S \\ 0 & \frac{1}{2}\Omega_S & \delta \end{pmatrix} \tag{4.93}$$

Where we have already made a RWA. We will have eigenstates made from the bare Hamiltonian eigenstates $\left|0\right\rangle$, $\left|1\right\rangle$, and $\left|e\right\rangle$. These eigenstates can be parametrized by,

$$|\psi_+\rangle = \sin\Theta\sin\Phi\,|0\rangle + \cos\Phi\,|e\rangle + \cos\Theta\sin\Phi\,|1\rangle \tag{4.94}$$

$$|\psi_0\rangle = \cos\Theta\,|0\rangle - \sin\Theta\,|1\rangle \tag{4.95}$$

$$|\psi_-\rangle = \sin\Theta\cos\Phi\,|0\rangle - \sin\Phi\,|e\rangle + \cos\Theta\cos\Phi\,|1\rangle \tag{4.96}$$

The eigenvalues for these states are,

$$\omega_\pm = \Delta \pm \sqrt{\Omega_P^2 + \Omega_S^2 + \Delta^2} \tag{4.97}$$

$$\omega_0 = 0 \tag{4.98}$$

and the angles Θ and Φ can be controlled by tuning the coupling rates Ω_p and Ω_S. Specifically, for the case where the two photon resonance condition is met, these angles are give by [50],

$$\tan\Theta = \frac{\Omega_P}{\Omega_S} \tag{4.99}$$

$$\tan\Phi = \frac{(\Omega_P^2 + \Omega_S^2)^{\frac{1}{2}}}{(\Omega_P^2 + \Omega_S^2 + \Delta^2)^{\frac{1}{2}} + \Delta} \tag{4.100}$$

From these eigenstates we can see that one of these states, $|\phi_0\rangle$, will coherently evolve between $|0\rangle$ and $|1\rangle$, if we initialize in $|0\rangle$ this state has a lot of overlap with

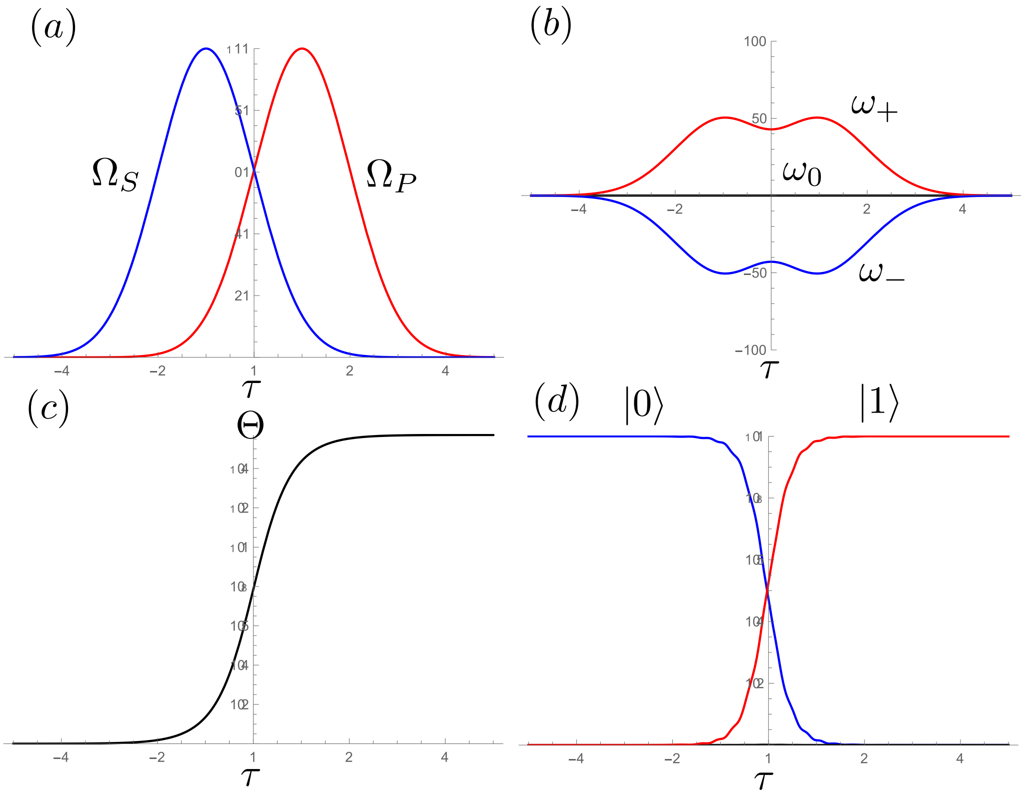

Figure 4.3: Evolution of various parameters as a function of normalized time if we ramp the coupling in a Gaussian fashion as shown in (a). The eigenvalues evolve as depicted in (b). If we start in the initial state $|0\rangle$ then we can transfer all of the population to $|1\rangle$. This is equivalent to smoothly varying the Θ parameter. This is shown in figures (c) and (d).

$|\psi_0\rangle$ when the coupling fields are off. If we adiabatically turn on the couplings Ω_P followed by Ω_S we can get full transfer of the population from $|0\rangle$ to $|1\rangle$ without significant overlap with $|\psi_\pm\rangle$. The condition on adiabaticity for this case is given by,

$$|\omega_\pm - \omega_0| \gg |\dot{\Theta}| \tag{4.101}$$

$$\gg \left| \frac{\dot{\Omega}_P \Omega_S - \dot{\Omega}_S \Omega_P}{\Omega_S^2 + \Omega_P^2} \right| \tag{4.102}$$

We can perform these types of transition on our RSB transitions, this allows us to transfer all the populations from the spin-down state to the spin-up state regardless of the small variations in Rabi rates between different phonon occupations. We want to use this operation extensively in a recursive procedure we will discuss in the next chapter to readout the phonon excitation number.

Chapter 5: Phonon Toolbox

Control and manipulation of bosonic degrees of freedom have been proposed as good candidates to test fundamental questions in quantum information science [9, 51–53]. In particular boson sampling has emerged as an area of extensive experimental research in the photonics community [54–56]. However, the experimental challenges of a linear optics implementation of such a sampler may prove extremely difficult to overcome in larger systems. Recently there have been proposals to use the external degrees of freedom in trapped ion chain as the bosons in a trapped ion boson sampling device [52].

To perform any of these experiments, however, one will need to have exquisite control of the phonon states of the ion chain. Here we present our progress towards creating a toolbox which allows for the initialization of a specific phonon Fock state, as well as readout of that state. We make use of our micro-fabricated ion trap to manipulate and shuttle the ion chains. By making use of this transport and known composite pulse sequences, we will show individual ion addressing without tightly focused beams. We also show that distillation of this initialized phonon state can be done through measurement without destroying the coherence of the coupled phonon-spin state. By using a STIRAP process, we can in principle recover the phonon occupation we initialized.

5.1 Sideband Cooling

To begin any experiments which utilize phonons as a resource for quantum information, we need to be able to initialize the phonon state of the ion chain to a pure state. The Doppler cooling we used to cool ions near the ground state of the trap still left an average phonon occupation, $\bar{n} \approx 5$. The thermal distribution associated with this many phonons is still too broad to use reliably in a simulation of bosonic physics. To sub-Doppler cool, we will utilize the spin-motion coupling derived from the coherent Raman interactions discussed previously. By tuning our Raman beatnote to be resonant with terms which destroy phonons conditional on a spin-flip,

$$\tilde{H}_I^{RSB} = \sum_j \eta_{i,j} \Omega (\sigma_j^+ \hat{a}_i + \sigma_j^- \hat{a}_i^\dagger) \tag{5.1}$$

We can remove quanta of phonon excitation, these are known as red sideband transitions (RSB). The other first order phonon modifying terms are transitions that add a phonon conditional of a spin flip, which are known as blue sideband transitions (BSB) and are given by,

$$\tilde{H}_I^{BSB} = \sum_j \eta_{i,j} \Omega (\sigma_j^+ \hat{a}_i^\dagger + \sigma_j^- \hat{a}_i) \tag{5.2}$$

Once the ion spin is flipped, we can re-initialize it in the spin-down configuration through the optical pumping scheme described earlier. This scattering imparts $\hbar\boldsymbol{k}$ of momentum to the ions but it only takes a few scattering events to optically pump the ions and $\hbar\boldsymbol{k}$[1] is much less than the secular frequency. Thus we expect optical pumping to have a minimal impact on phonon state occupation. Once the internal state of the atom is back in the spin-down state then we can repeat the procedure of removing a phonon and optically pumping. By doing this, in our experiment roughly 30 times, the average phonon number can be reduced to well below one quantum.

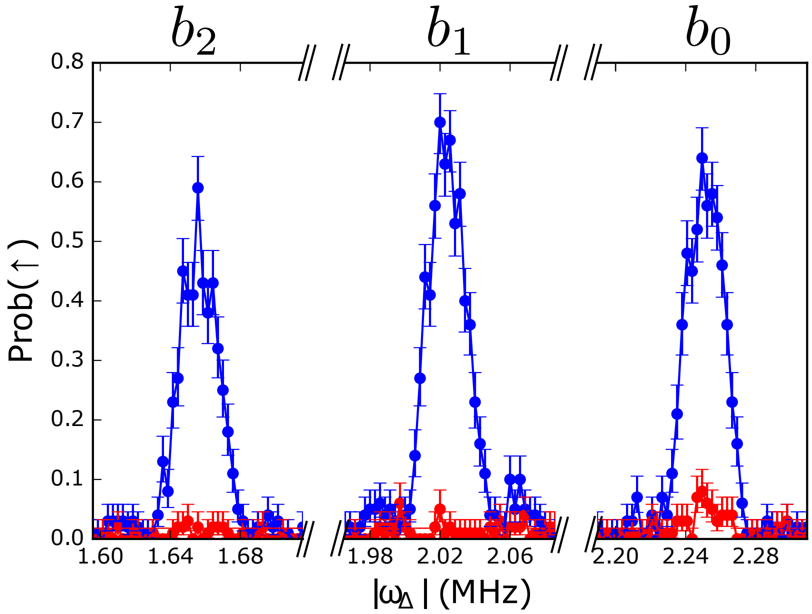

Figure 5.1: Mode occupation as a function of detuning in a three ion chain. By scanning the Raman beatnote over the the RSB and BSB transitions and comparing the relative amplitudes, we can determine the mode occupations after sub-Doppler cooling. The average phonon occupations of the above curves are $\bar{\text{n}}_{mode1} \approx 0.129$, $\bar{\text{n}}_{mode2} \approx 0.061$, and $\bar{\text{n}}_{mode3} \approx 0.026$ for a three ion chain. The error bars on this plot depict a 1 σ confidence interval. This interval was calculated using the Clapper-Pearson interval [48] for binomially distributed Bernoulli trials. This should give an overly conservative estimate of the error bars. Error bars will be calculated in a similar fashion throughout this thesis.

---

[1] Discussed in depth in Chapter 2.3.3.

This process is then repeated on all modes, we have modified the principal axes of the trap such that only the in plane transverse modes couple to the momentum kick imparted by the Raman beatnote. This is accomplished by a applying a twist to the DC quadrapole[2]. For a three ion chain we need to cool three modes. This is the first stage of testing any of the tools we have developed to initialize and manipulate phonon states.

We can measure the residual phonon population, as seen in Fig 5.1, by measuring the amplitude of the phonon subtracting (RSB) vs phonon adding (BSB) transitions. For a fixed time, the ratio between these amplitudes is related to the mean phonon occupation of mode being measured by,

$$\frac{RSB}{BSB} = \frac{\bar{n}}{\bar{n}+1} \tag{5.3}$$

5.1.1 Heating Rates

As mentioned previously, one drawback to using a micro-fabricated ion trap is that because the ions are close to the trapping surfaces, they undergo heating at a rate which was has confounded the community for some time. Therefore if we are going to claim any capability to manipulate and create Fock states of the motion using a micro-fabricated ion trap, we need to say something concrete about the heating rates of our trap. I want to preface this discussion by saying that heating rates in general are a challenging thing to nail down. Our heating rates may not be

---

[2] This is one of the solutions we have the trap designers construct for us, we can add this on top of the harmonic axial confinement to rotate the DC principal axis.

indicative of other laboratories, even if they use the same hardware.

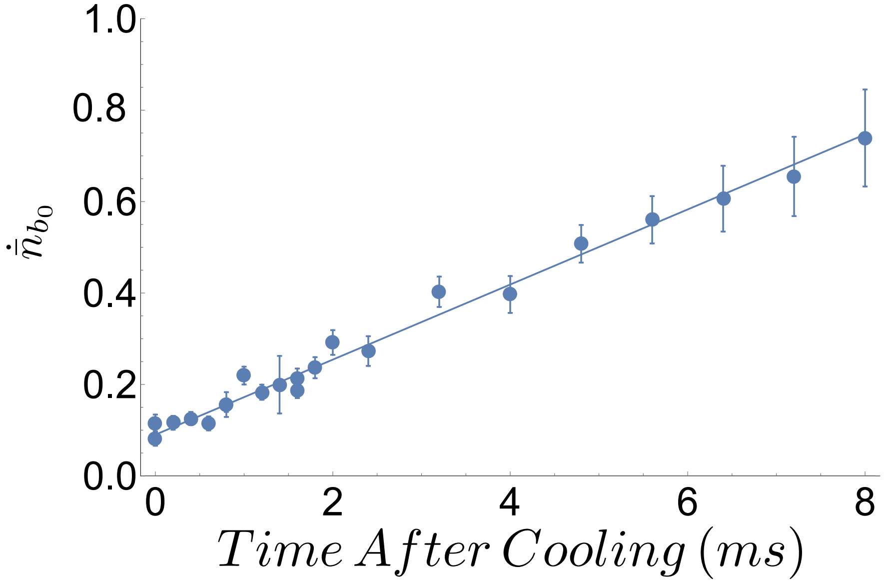

Figure 5.2: Change in the number of phonons in mode b_0 as a function of time after cooling. The heating rate is found to be $\dot{\bar{n}}_{COM} \approx 80 \pm 9\frac{quanta}{s}$, the slope of this line. The other two modes are strongly decoupled from environmental gradients, so these rates were so low they became impractical to measure. Error bars are again calculated from a binomial distribution.

In our case, we have found surprisingly low heating rates, see Fig. 5.2. The largest heating rate will always be found in the normal mode associate with the common mode of motion, b_0. The b_0 mode will be the only mode that has overlap with scalar electric fields. To drive motion in the other modes the driving field must have a gradient in the electric field amplitude across the ion chain. Considering the ion spacing and the distance to the nearest surfaces, gradients across the ion chain can be extremely hard to generate. These gradients are unlikely to occur due to deposited charges or oscillating dipoles on the surface of the trap, which are two of the current theories of anomalous heating[3] [58–60].

---

[3] However, there has been very reccent work that suggests that the heating rate is somehow entirely dominated by the RF [57].

This heating rate has been measured to be $80 \pm 9 \frac{quanta}{s}$ on the 2.7 MHz in plane transverse b_0 mode. This implies that we have approximately 1 ms in which to do our experiments before a pollutant phonon finds its way into the system. Although this may not seem like a long time, the longest interactions we generally induce are on the order of 200 μs. Also, in other groups using micro-fabricated traps, the heating rates were reduced by two orders of magnitude by going cryogenic [61–63]. Certainly this is a complication we wish to avoid, but it is not outside the realm of possibility.

The heating rates associated with the other modes are the only other rates relevant for the rest of this thesis. These rates were measured to be so low that we have not been able to successfully extract a number for them. For the purposes of this thesis, we will focus mainly on three ion chains using the center of mass mode, b_0, and the next order symmetric mode, b_2[4]. This means we will be limited by the COM mode heating rate. However, we are still able to demonstrate the tools we have developed thus far, which should continue to be applicable if we decide to take steps to mitigate the effects of this heating rate.

5.2 Individual Addressing

All of the interactions that we are going to try and employ are derived by couplings to the spin and the motion via Raman transitions which mediate changes in the phonon state contingent on the spin state. For this reason it would be highly

---

[4] We do not use b_1 because we hope to drive interference terms between these modes, discussed in Chapter 6, parametrically and the difference frequencies between other modes and b_1 are two small to satisfy a RWA we must perform to drive this interaction.

advantageous to be able to initialize and manipulate the entire spin manifold to specific states. The traditional way to achieve individual addressing is to tightly focus laser beams so as to only interrogate single ions with a specific laser pulse [64]. This approach can prove challenging for micro-fabricated traps where beam must either skim the surface of the trap or pass through the trapping structure. Beams that skim the surface are usually limited to $NA \approx 0.2$ before the beams begin to clip on nearby surfaces that route electrode wiring out of the vacuum chamber.

One of the challenges specific to our particular trap, the BGA, is that it is difficult to get a tight focus with our 355 nm laser beams. To individually interrogate single ions by hitting only the ions of interest in the chain we need to achieve spots sizes well below the ion spacing of, 5 μm, and the tightest Gaussian spots that we can achieve before we begin to clip on parts of the trap assembly is 8 μm. Because more traditional forms of individual addressing are not accessible to us we make use of one of the features of a micro-fabricated trap and shuttle ions to an intensity gradient of the beatnote, where the Rabi rates on ions will be different. This coupled with composite pulse sequences allow us to flip single spins in our chain.

5.2.1 Transport

The greatest advantage of surface traps is the ability to manipulate the axial confinement to a degree of resolution that is inaccessible to macro-fabricated traps. By utilizing this ability, we shuttle our chain of ions 20 μm away from the center of the overlap between our two Raman beams. Once the chain is sitting on the

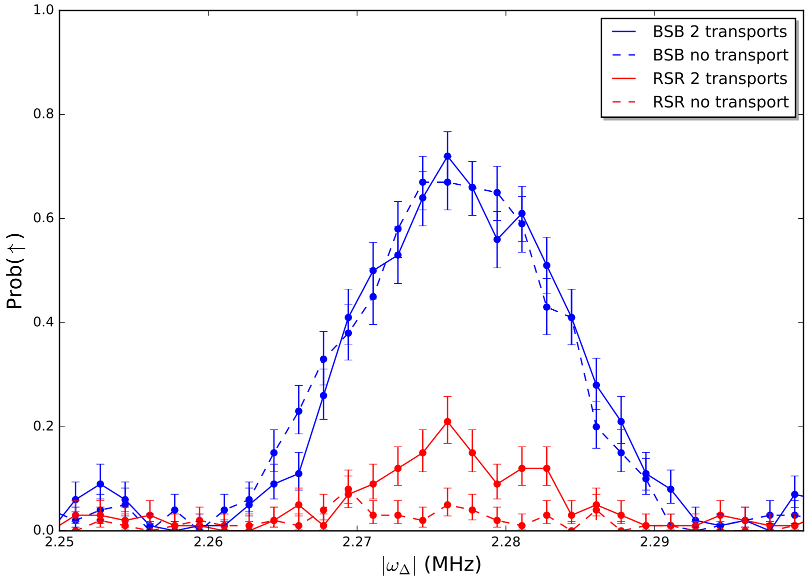

Figure 5.3: Probability of a spin-flip as a function of beatnote detuning. By looking at the asymmetry between the RSB and BSB transitions after transport, we can determine the approximate heating due to transport. In this case, we transport out to the location in which we plan to do our individual addressing and back twice. We measure the sidebands only for the COM mode, b_0, because it will be the mode most effected by the action we find $\Delta\bar{n} \approx 0.2\frac{quanta}{transport}$. Error bars are again calculated from a binomial distribution.

intensity gradient of the driving field, each ion experiences a different Rabi rate.

Once we have driven the chain into the desired spin state we can transport the ions back to the center of the beam overlap and continue with our procedures that globally address the spin chain. The biggest concern with doing this type of addressing or transport is that the transport will be non-adiabatic to the ion motion, inducing higher phonon mode occupation. Effectively heating the center of mass motion of the chain. In examining this, we have determined that when the transport potentials are finely tuned we can achieve as little as $\Delta\bar{n} \approx 0.2$ per transport on the center of mass, see Fig. 5.3. This of course is not ideal, but once again it is sufficient for out purposes . With tighter foci of our Raman beams and extensively optimized transport potentials, I am confident that this heating could be made negligible.

In principle, this is all we need to flip individual spins, however, the difference in Rabi rate between different ions is not sufficient to truly initialize them in a clean manner. Therefore, we couple this technique with composite pulse sequences, described in the next section, to try and obtain a more pure spin configuration.

5.2.2 Composite pulse sequences

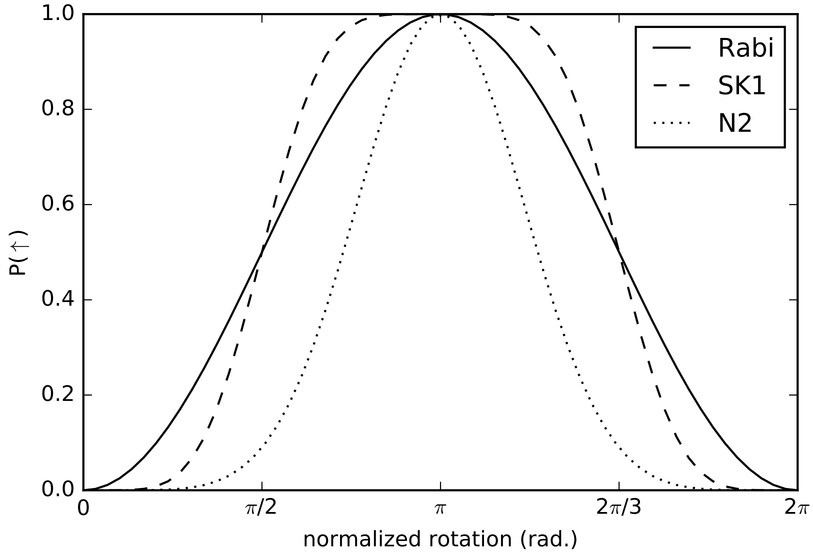

Figure 5.4: Probability of population transfer as a function of normalized time for three different pulse sequences. By using different pulse sequences we can get full population transfer to the spin-up state with more or less dependence on the rotation angle about the Bloch sphere. This plot shows population transfer for a single pulse as well as two composite pulse sequences.

The goal of a composite pulse sequence is to reduce the error from an imperfect roation around the Bloch sphere without knowledge of the specific error which has occured, see Fig. 5.4. For example if a single pulse has a small amplitude error $\mathcal{O}(\epsilon)$, by repeating this rotation n times the error is reduced to $\mathcal{O}(\epsilon^n)$ [65]. There have been a few composite pulse sequences developed to compensate for arbitrary errors, generally these pulses involve doing multiple rotations around the Bloch sphere about different axes.

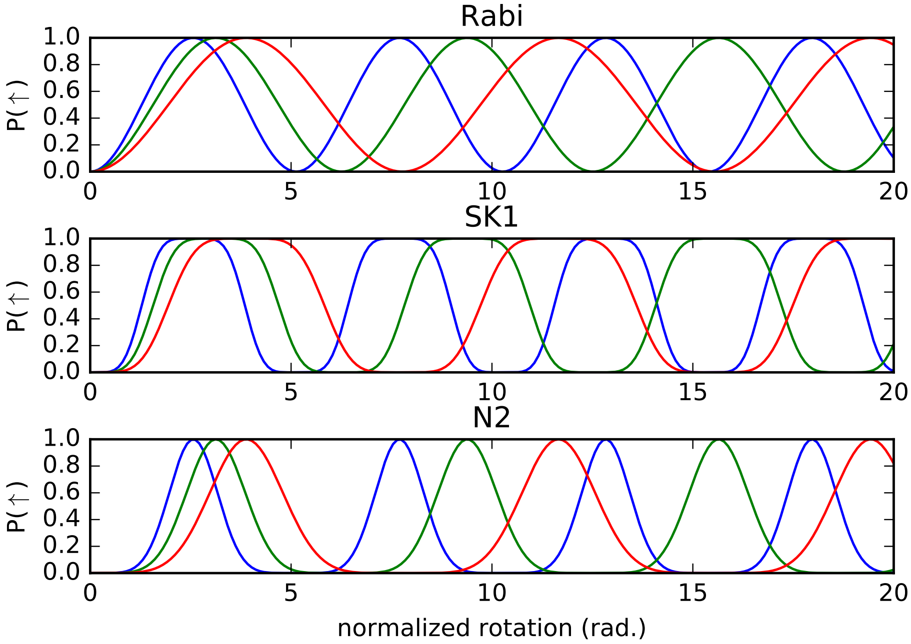

Figure 5.5: Probability of a population transfer as a function of normalized rotations for three different composite pulse sequences. Each color represents a different ion which experiences a different intensity of the beatnote. The upper curve shows Rabi flopping with an intensity gradient. The middle curve shows the SK1 pulse sequence and the bottom curve depicts the N2 pulse sequence.

From theoretical curves of the spin dynamics, we can see the differences in population transfer between the various pulse sequences we perform as a function of π-time, see Fig. 5.5. We compare three different sequences of driving pulses: First, we directly compare the different rates at which individual ion spins are flipped by turning on a single pulse. Next, we use a bandpass composite pulse sequence known as SK1, which is less sensitive to intensity fluctuations, effectively flattening the crests and troughs of the sinusoidal oscillations of the Bloch vector [65]. Finally, we examine a narrow band pulse sequence, N2, which is extremely sensitive to intensity [50,66]. This pulse sequence is narrowly peaked around a specific normalized π-time. In the end we choose which pulse sequence to use based on the number of ions and day-to-day calibrations. The three ion data used in this thesis was taken, almost exclusively, with the N2 composite pulse sequence.

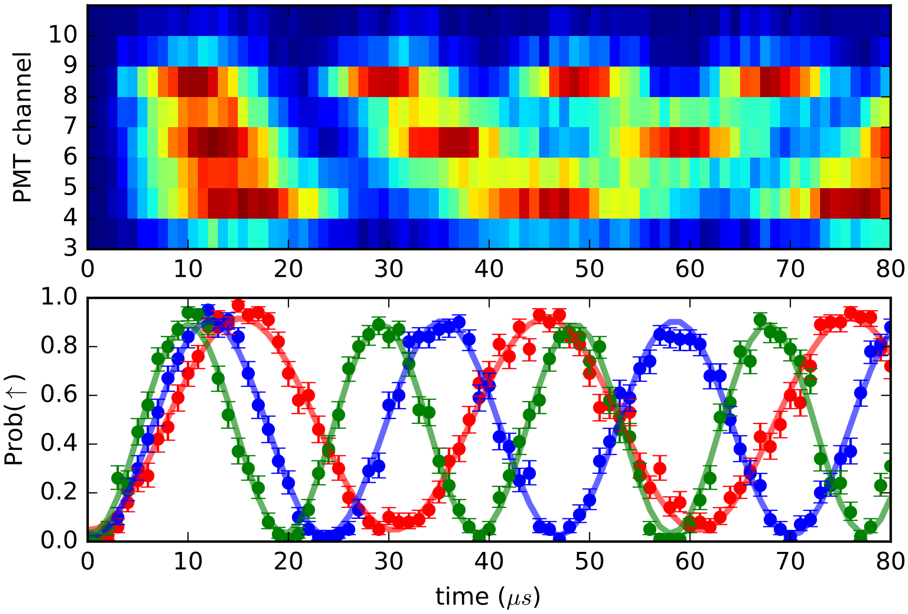

Figure 5.6: The lower curve shows calculated spin-up probabilities by implementing a threshold on the PMT data. The semi-transparent lines show a $\sin^2$ fit to the dynamics, these curves are only meant as guides to the eye. The heat map shows the photon count received by PMT channels on our multi-channel PMT. By using a single pulse there is still a great deal of overlap between individual ions being flipped up regardless of pulse time. Error bars are again calculated from a binomial distribution.

By making use of the intensity gradient in the beatnote that we transport ions over, we try and find a time where we find only one spin flipped for a given pulse

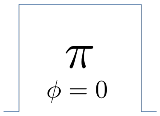

Figure 5.7: Single pulse sequence with normalized rotation angle around the Bloch sphere. The phase ϕ represents the axis about which we are performing the rotation.

sequence. In principle we could achieve this with a single pulse, see Fig 5.6 and 5.7, by manipulating the intensity gradient as well as the ion spacing. However, we can get much better temporal separation of spin flips by employing the composite pulse sequences discussed above.

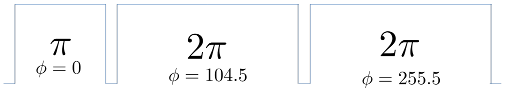

Figure 5.8: The SK1 pulse sequence with normalized rotation angle. The two additional pulses are done about a axes rotated from the initial rotation axis given by the angle ϕ.

By applying the SK1 sequence, see Fig. 5.8, we can eliminate some of the dependence on intensity, for example if a rotation angle, using a single pulse, would rotate an ion spin state 80% bright, using the SK1 pulse sequence that same rotation angle rotates the spin state fully bright, see Fig. 5.9. Similarly if a rotation angle, using a single pulse, would rotate the ion spin state 20% bright, using the SK1 sequence the ion will remain totally dark. However, this comes at the cost of a reduced effect of the intensity gradient. By separating ions by larger distances this pulse sequence is quite effective. When trapping only two ions and manipulating phonons, this is pulse sequence we use for initialization.

For three ion chains, we do much better using the N2 pulse sequence, see Fig. 5.10, because the N2 sequence is so strongly dependent on intensity, see Fig. 5.11.

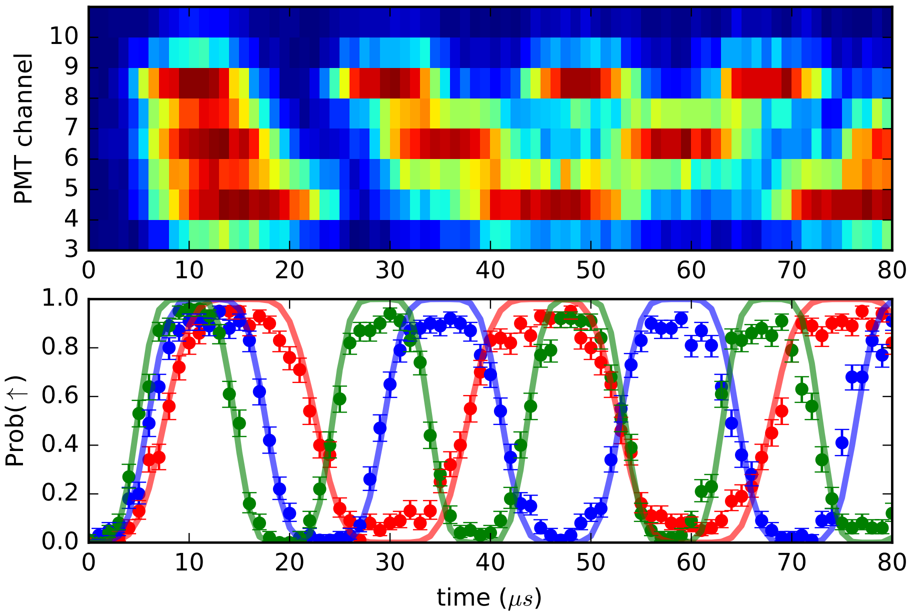

Figure 5.9: The SK1 pulse sequence results. It allows us to to get very high fidelity spin flips. The semi-transparent lines show the dynamics of perfect SK1 flopping. However as shown in the heat map there is considerable overlap with adjacent spin flips. These curves are meant as guides to the eye. Error bars are again calculated from a binomial distribution.

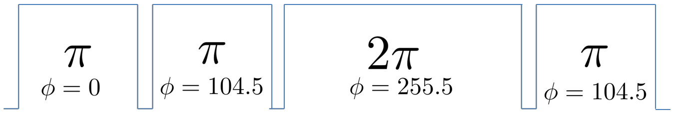

Figure 5.10: N2 pulse sequence with normalized rotation angle. The two additional pulses are done about a axes rotated from the initial rotation axis given by the angle ϕ.

This means we get the largest separation in time of individual spins flipped for the same intensity gradient. Unfortunately this means that initialization is now very sensitive to intensity fluctuations and pointing instabilities of the Raman laser. We have measured these to be $< 1\%$ in approximately 100 ms of measurement time. However, at long time scales the laser intensity can vary by as much as 20%, which means we have to calibrate the appropriate time to initialize spins several times a day.

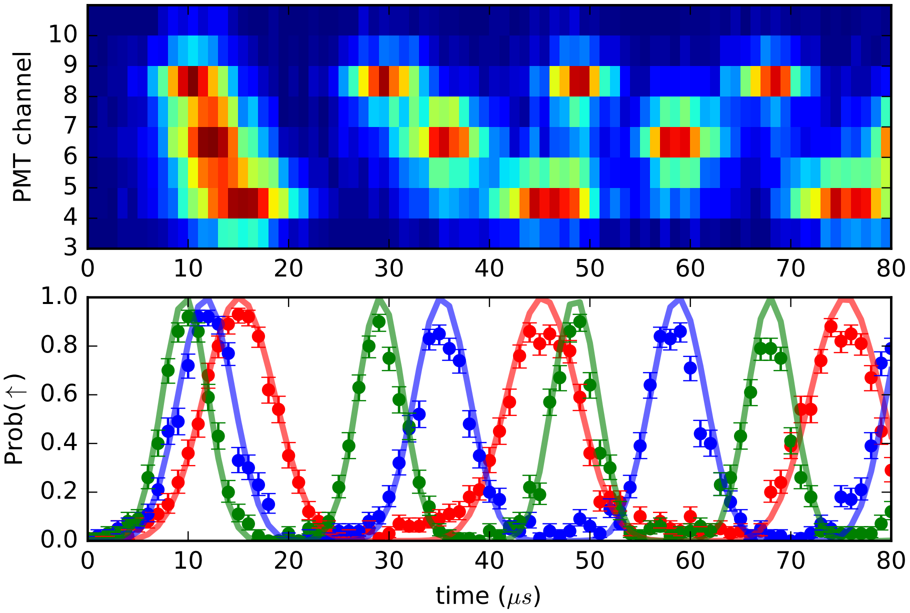

Figure 5.11: N2 pulse sequence measurement, this gives the best separation of spin-flips. This can be most readily observed in the multi-channel PMT where there is a distinct gap between adjacent ion spin flips. The semi-transparent lines show the dynamics of perfect N2 flopping. These curves are meant as guides to the eye. Error bars are again calculated from a binomial distribution.

To initialize a specific phonon occupation, we will make use of the conditional nature of our sideband transition, which will only change the phonon occupation if there is a corresponding spin to flip. To change the phonon state by one quanta, we need to have only one spin flipped before we apply a RSB. This requires the individual ion addressing described above so that we can selectively change the spin state of a specific ion. We expect to exchange the single spin-flip with one additional excitation of motion.

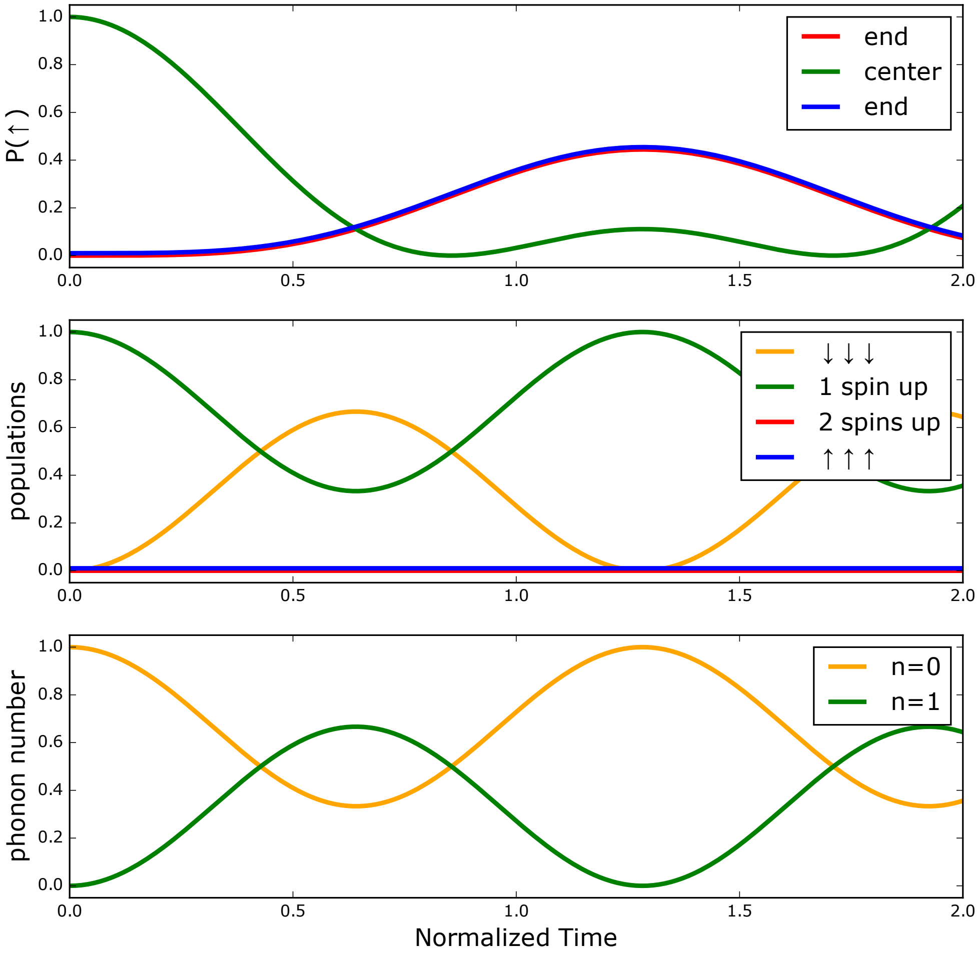

Figure 5.12: Calculation of the evolution of spin populations and phonon number with three ions. If we successfully flip an individual spin then we can drive a RSB on the mode we wish to prepare in order to initialize a single excitation in that mode. The top curve shows the spin dynamics as we initialize an excitation in mode b_2 from chapter 2. The middle curve shows the evolution of the spin manifold. The bottom curve shows the expected evolution of the phonon excitation.

Once we have flipped a single spin, we can drive a RSB to put a single phonon excitation in a given normal mode. Driving this term results in the state,

$c_{\downarrow,\downarrow,\downarrow} \left|\downarrow,\downarrow,\downarrow\right\rangle \left|1,0,0\right\rangle + (c_{\uparrow,\downarrow,\downarrow} \left|\uparrow,\downarrow,\downarrow\right\rangle + c_{\downarrow,\uparrow,\downarrow} \left|\downarrow,\uparrow,\downarrow\right\rangle + c_{\downarrow,\downarrow,\uparrow} \left|\downarrow,\downarrow,\uparrow\right\rangle) \left|0,0,0\right\rangle$, which has the highest overlap with $\left|\downarrow,\downarrow,\downarrow\right\rangle \left|1,0,0\right\rangle$, but still has a non-zero overlap with a zero phonon excitation state, see Fig. 5.12. This is because the manifold of possible spin flips is not a two state manifold. As we drive the spin, which was initialized up, back down adding a phonon in the process, we also begin to flip up all the other combinations of one spin flipped up states by removing the phonon we just added. This process is identical to how phonons were previously removed from the system during sideband cooling.

This complication requires us to distill only the component of the state which has the phonon we are interested in, and trace out all other spin components. To make sure we can start with a pure Fock state of the normal modes we are interested in, we perform a RSB such that we maximize overlap with $\left|\downarrow,\downarrow,\downarrow\right\rangle \left|1,0,0\right\rangle$, see Fig. 5.13, and then turn on our 369 nm laser tuned to scatter photons from the spin up state via the ${}^2P_{1/2}$ state. The splitting between the two hyperfine ground states we are using as spin-up and spin-down is large enough that the spin down states do not couple to the excited state. The spin-down state will remain unaffected by this light. If we collect any scattered photons, we re-pump the ion chain and repeat this procedure until we do not detect any scattered photons. This distills our quantum state to only that component with all spins down in a probabilistic fashion, where the probability of success is dependent on the mode we are driving and the ion we individually addressed. This state distillation has not been used before in this context and constitutes a new tool for engineering specific Fock states in ${}^{171}\mathrm{Yb}^+$ trapped ion chains.

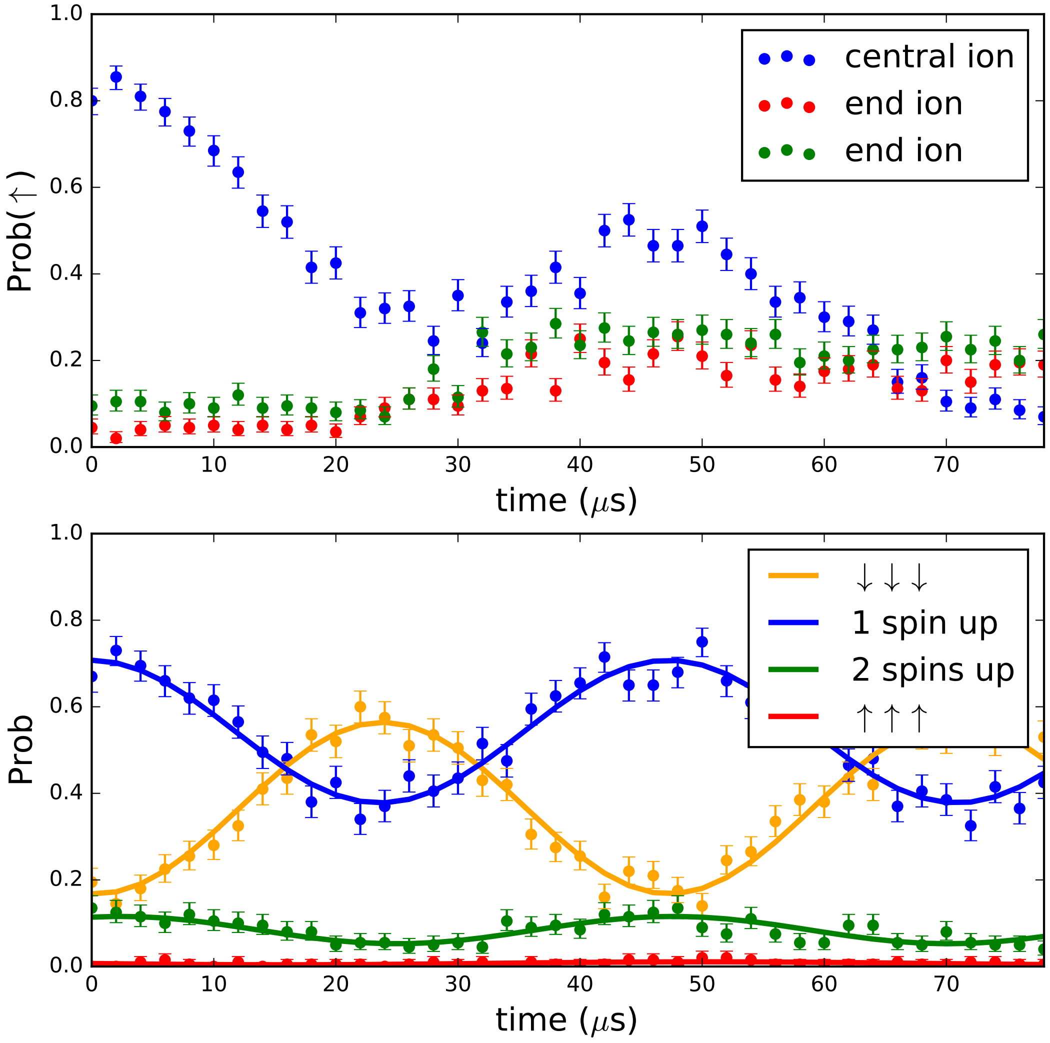

Figure 5.13: Measured evolution of the three ion populations. By driving a RSB transition, we flip a single spin as expected but which ion flips begins to become unclear after one exchange of motion with spin. The solid lines on the lower plot are $\sin^2$ fits to the data. Error bars are again calculated from a binomial distribution.

To verify that we still maintain purity in our phonon state after this distillation, we test the coherence of spin motion coupling by Rabi flopping on a RSB of the mode containing the excitation we introduced. If we have truly distilled $|\downarrow,\downarrow,\downarrow\rangle\,|1\rangle$

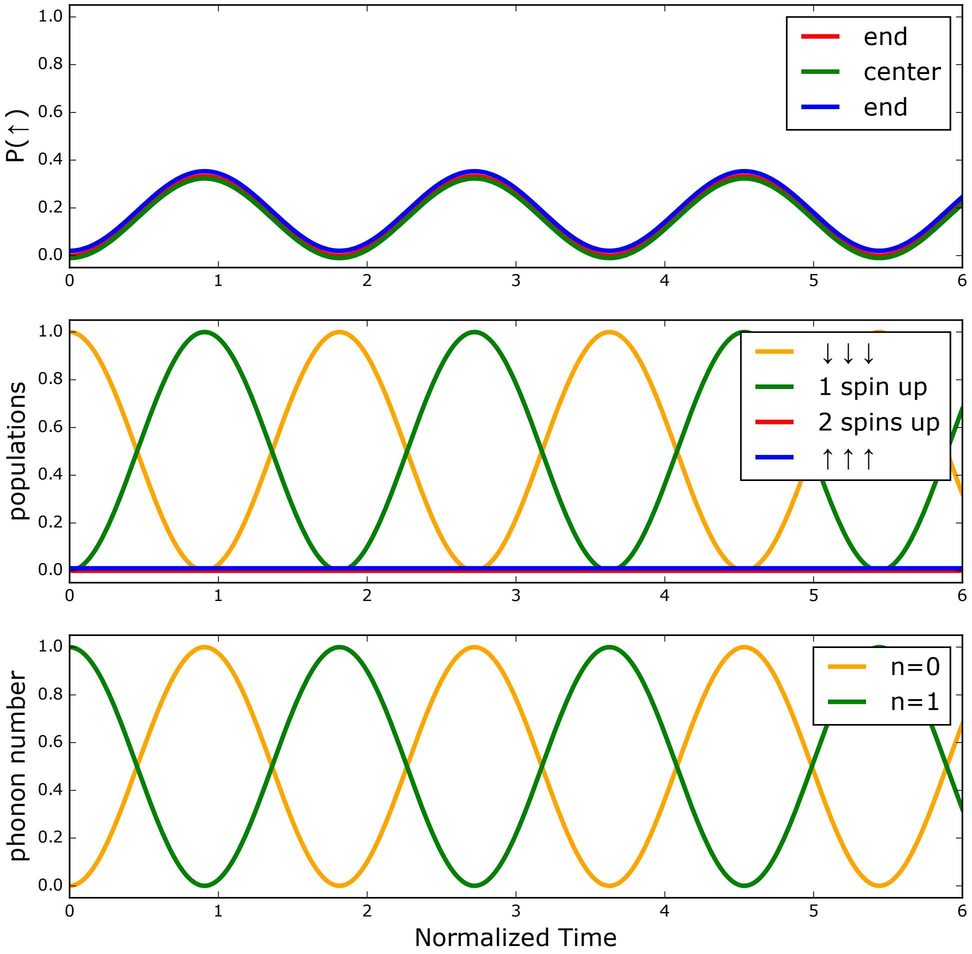

Figure 5.14: Calculated spin population and phonon number evolution. By driving a RSB after distillation, hopefully we exchange the single excitation of motion with a single spin flip. These theoretical curves show this for the b_0 mode. The top curve shows the spin dynamics of each ion. The middle curve shows the spin-manifold populations. The bottom curve shows the expected evolution of the excitation of motion. The time here is normalized to the coupling strength, for these simulations all of these coupling rates were set to unity.

in whatever mode we want to distill, then we should maintain coherent flopping between the $|\downarrow,\downarrow,\downarrow\rangle$ state and the one spin flipped manifold. Any leakage into higher phonon population or thermal state contamination should manifest as multiple spins being flipped simultaneously. These populations remain negligible, and we take this to mean our procedure up to this point, including transport and state distillation, is not overly contaminated with undesirable phonon occupation. We can perform these experiments on all three modes after multiple steps of distillation.

We look specifically at the case where we are trying to initialize the state $|\downarrow,\downarrow,\downarrow\rangle\,|1,0,0\rangle$, where the basis for the motion is $|b_0,b_1,b_2\rangle$ from before. In this case, we should expect to see all spins flip equally but not simultaneously as we drive spin-motion coupling through a RSB on mode b_0, see Fig. 5.14. Our results show that we maintain coherent flopping between the equal spin manifolds[5] we expect to be moving population between, see Fig. 5.15. However, the contrast of both of these curves is lower than expected. We believe this has to do with imperfect spin-flips in our individual addressing procedure. If we leave population in the spin-down state of the ion we are trying to individually address, it will not participate in the phonon initialization. This specific error is not caught by the distillation procedure.

In the case of the b_2 mode, we should expect to see the middle spin flip twice as much as the outer ions, see Fig. 5.16, given the relative normal mode amplitudes. Once again we expect that none of the spins should flip simultaneously because we only have one excitation to exchange. Similar to mode b_0, we see a decrease of approximately 20% in contrast, see Fig. 5.17. This consistency between two very different modes reinforces our belief that the contrast degradation is due to a problem in spin initialization before adding a phonon.

---

[5] All spins down, one spin up, two spins up, or three spins up.

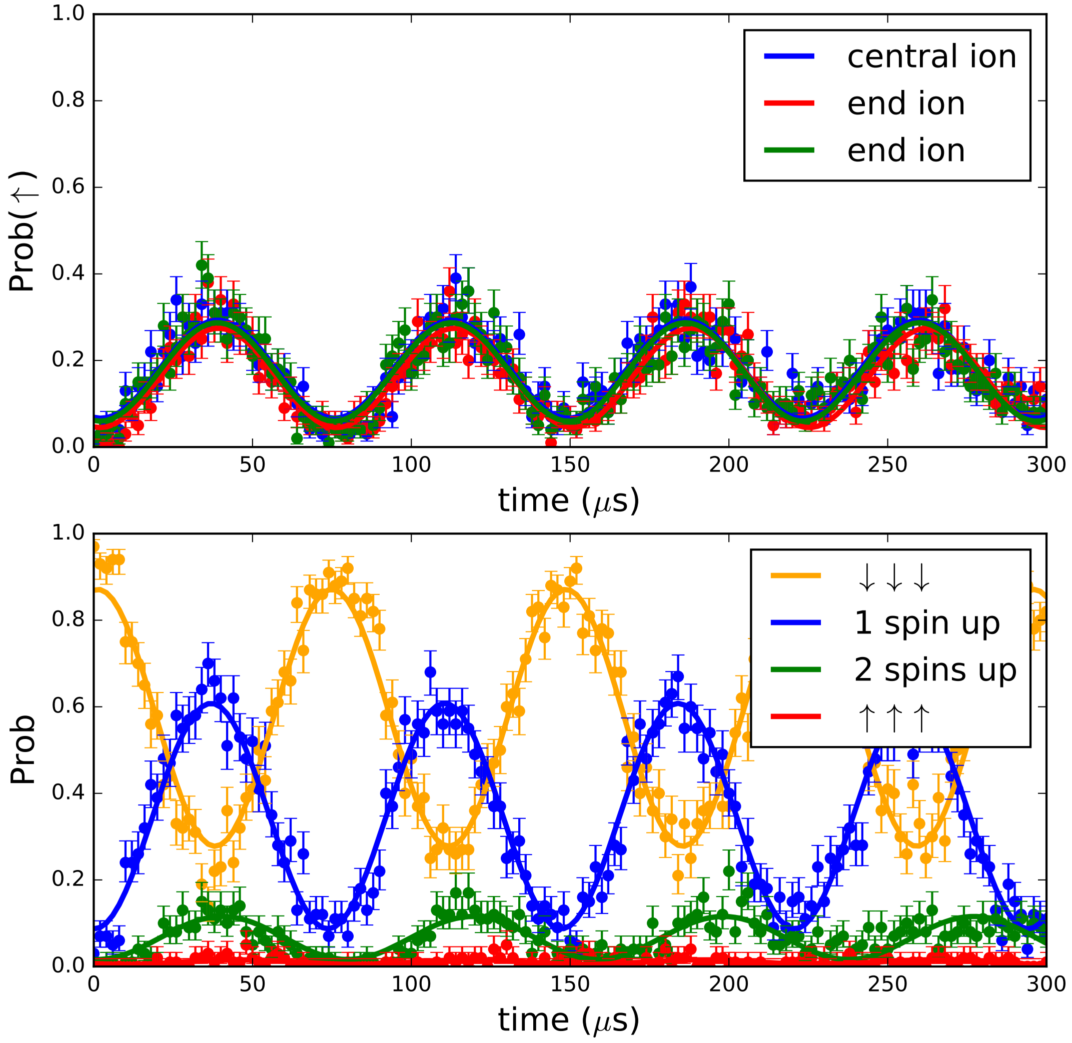

Figure 5.15: Experimental results of the simulated experiments in Fig. 5.14. The top plot shows the measured spin dynamics of each ion. The bottom plot shows the populations of the spin-manifolds. Note the reduced contrast in the spin manifold plot, we attribute this to poor initialization of spin. The solid lines are sine squared fits to the data of the form $A\sin^2(\omega t + \phi) + C$. Where A, ω, ϕ, and C are all fit parameters. Error bars are again calculated from a binomial distribution. The average reduced χ^2 for the fits on the upper plot is 0.95, for the lower plot the average reduced χ^2 is 0.985.

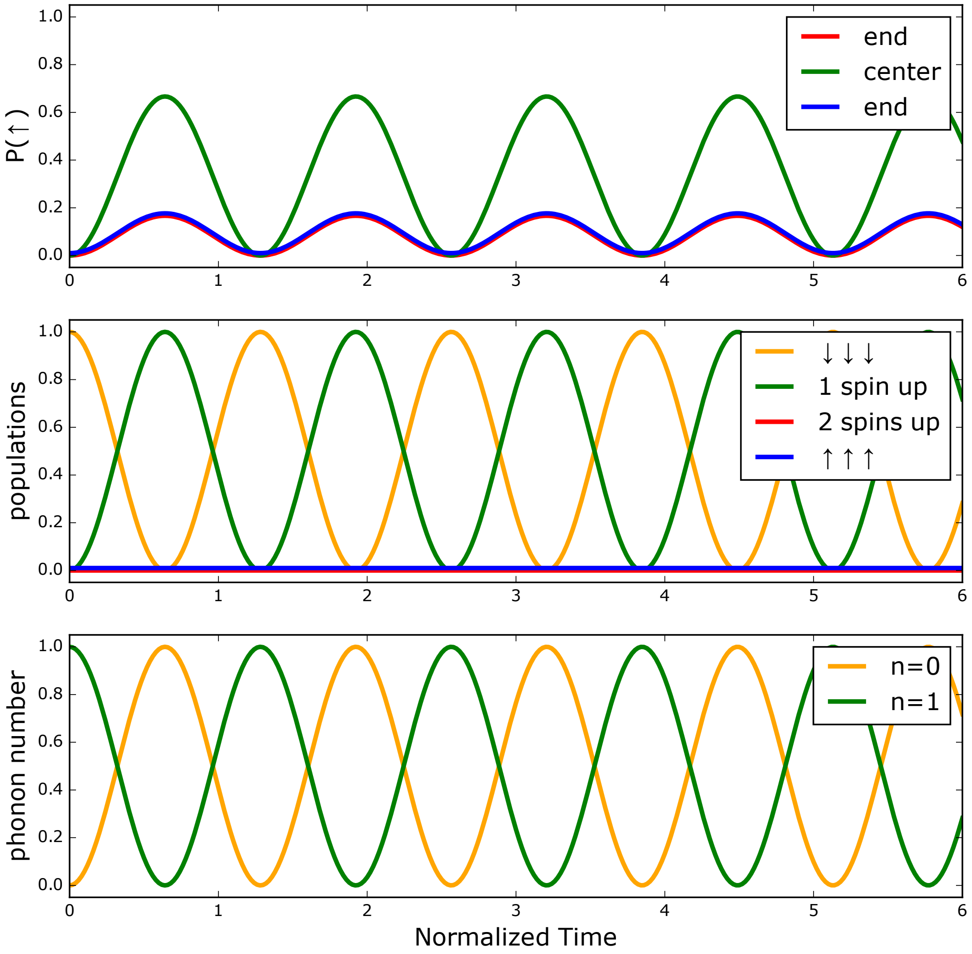

Figure 5.16: Calculated spin population and phonon number evolution. By driving a RSB after distillation hopefully we exchange the single excitation of motion with a single spin flip. These theoretical curves show this for the b_2 mode. The top curve shows the spin dynamics of each ion. The middle curve shows the spin-manifold populations. The bottom curve shows the expected evolution of the excitation of motion. Once again the normalized time is set but making the coupling strength unity and directly integrating the Schrödinger equation.

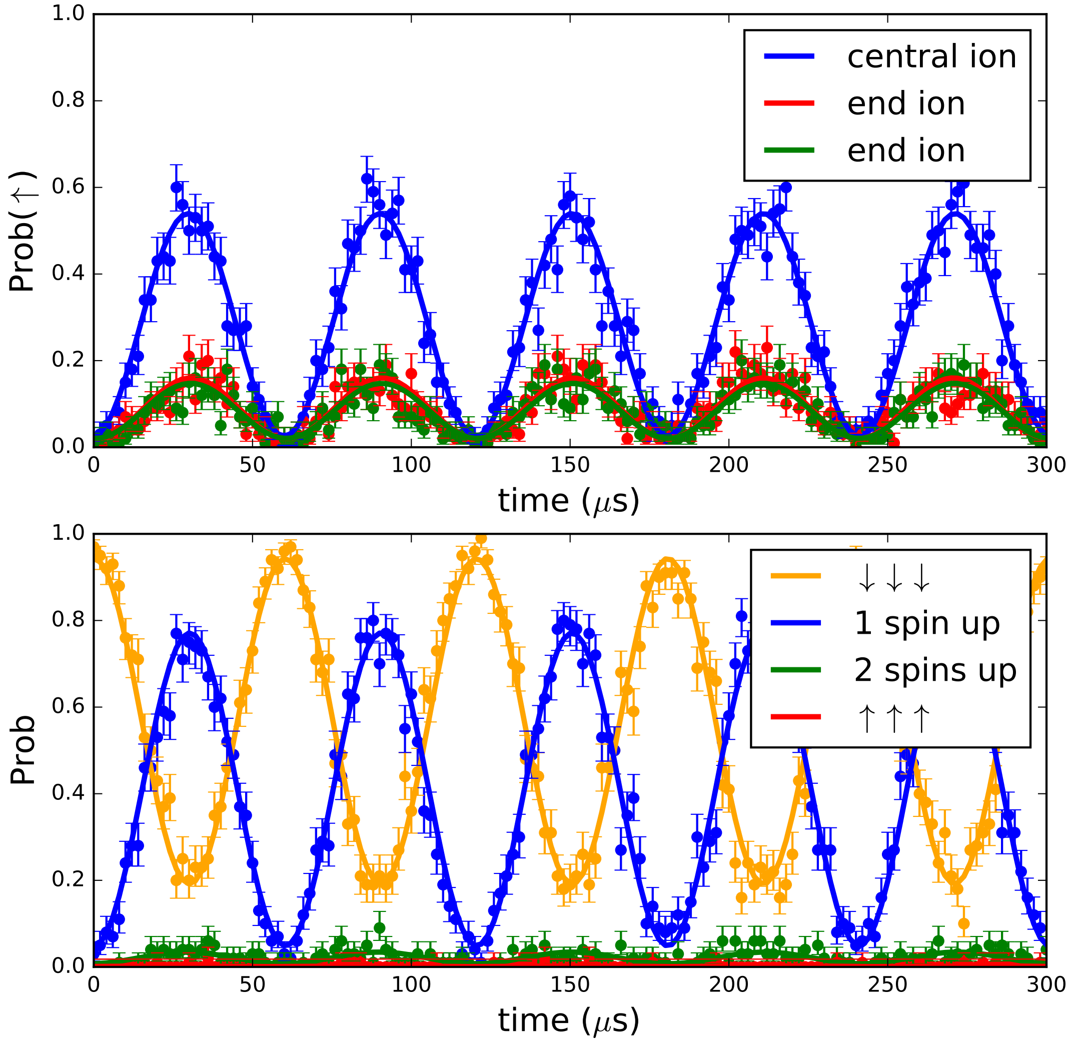

Figure 5.17: Experimental results of the simulation shown in Fig. 5.16. As before the top plot shows the measured spin dynamics of each ion and the bottom plot shows the populations of the spin-manifolds. The solid lines are sin squared fits to the data of the form $A\sin^2(\omega t + \phi) + C$. Where A, ω, ϕ, and C are all fit parameters. The average reduced χ^2 for the fits on the upper plot is 0.74, for the lower plot the average reduced χ^2 is 0.714. Error bars are again calculated from a binomial distribution.

5.4 Readout

In principle, the phonon occupation can be read out by comparing Rabi rates on the sideband transitions to known phonon occupations. However, this measurement would be subject to calibration errors which would make it less reliable than we would like it to be. Instead, we will read out the phonon occupation through a STIRAP process on the red sideband. The effect of this STIRAP procedure is to move all Fock population from $|n\rangle \rightarrow |n-1\rangle$, and in so doing flip a spin. By using this STIRAP procedure we are able to do this for wide a range of Fock states even though they each have Rabi rates that scale like $\sqrt{n}$. The pulse we use for our experiment is chirped in both frequency and amplitude [67].

Once mapped to the excited state, we do a spin flip transition to map all of the excited state populations to the ground state. However, the population associated with zero excitation, the ground state of the mode, will not have undergone a transition under the STIRAP process. The subsequent spin flip will put this population in the spin up state as opposed to the spin down state. If we try and detect the excited state, and collect any scattered photons we can say our population was in the $|n=0\rangle$ phonon Fock state at the beginning of this procedure. By repeating successive iterations of this process, leaving detection for the last step, then we can measure whether we have population in a given Fock state, see Fig. 5.19. This technique was proposed recently in the context of Boson sampling with ions [52], and has been demonstrated extensively for single ion states [49, 67]. We are currently working on generalizing a similar method for multi-ion chains, however, this

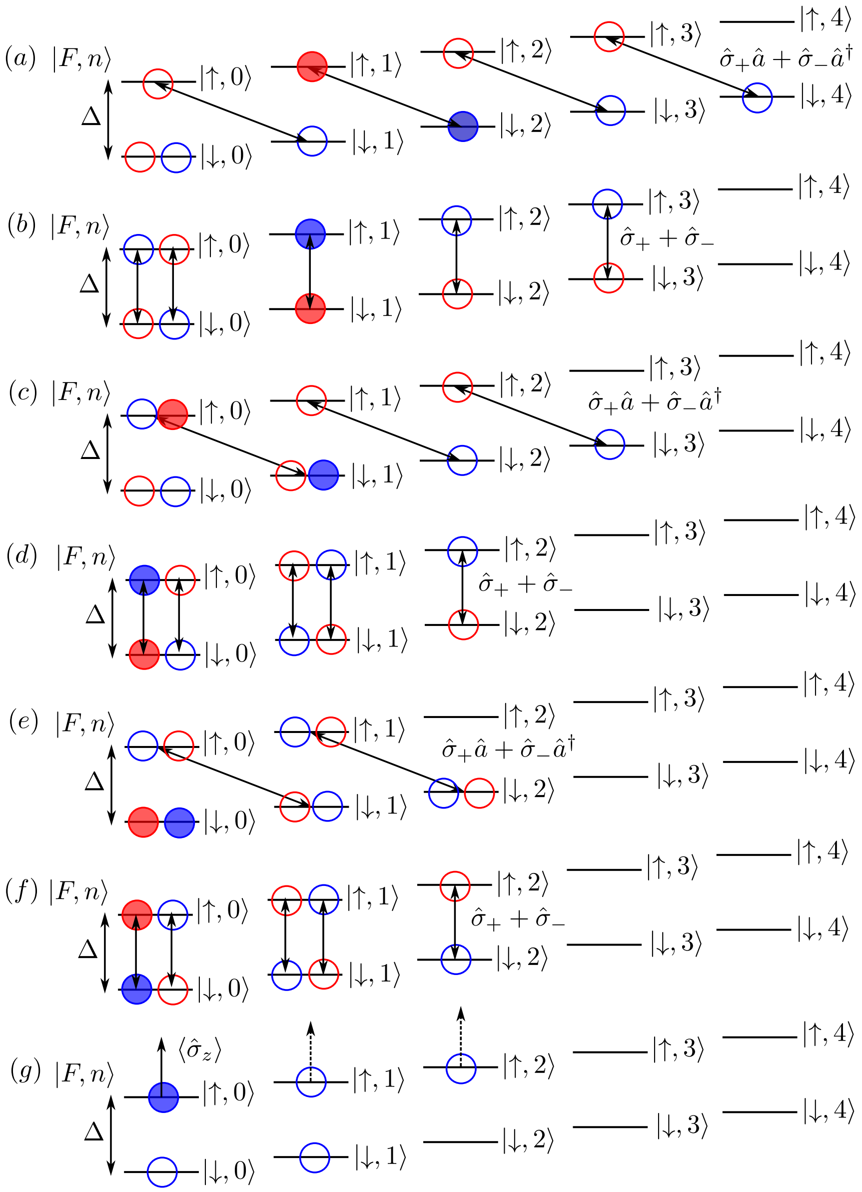

Figure 5.18: Procedure we plan on implementing to measure phonon number with STIRAP pulses. The blue circles represent the starting state before a procedure in this scheme, the red circles represent the end state after a procedure. The filled circle will represent the phonon mode we are trying to measure. In (a) we begin in the spin down state, by applying a STIRAP RSB we move the population to the spin up state by removing a quanta of motion. In (b) we apply a spin flip operation to put all of the population in the spin down state. Notice the population in the ground motion state moves to spin up. In (c-f) we repeat this procedure walking the population down. In (g) we turn on our detection laser, if we measure a photon we had occupation of the motion $n \leq 2$. By performing different numbers of these loops, we can read out the phonon occupation.

is complicated by the larger spin manifold. In principle, we can map normal mode excitations on single ion excitations[6] and read out in this way.

---

[6] Discussed in depth in section 6.2

Chapter 6: Phonon Interference

We have yet to talk about how these modes can be used for anything besides poor quantum memories. The tricky part is to engineer interactions between normal modes which will have dynamics that are not well captured by the spin degrees of freedom of the ion chain. For this we look to the photonics community, where photons play an identical role to the phonons in our current experiments. In photonics, interesting physics is achieved by using a network of beam splitters and utilizing bosonic statistics to generate non-trivial states. It would be ideal to demonstrate an experiment that has a direct analog to photonics using phonon excitations. This would also show the versatility of the tools we have been developing thus far. The demonstration experiment we have chosen to try is to look for Hong-Ou-Mandel (HOM) interference between phonon modes. I want to take some time to walk through these experiments, and then give our current results.

6.1 Hong-Ou-Mandel Photon Example

Hong-Ou-Mandel interference is a canonical example of the quantum behavior of light [68]. The experiment is relatively simple, given a beam splitter with perfect 50/50 visibility, take two identical single-photon sources and impinge those sources

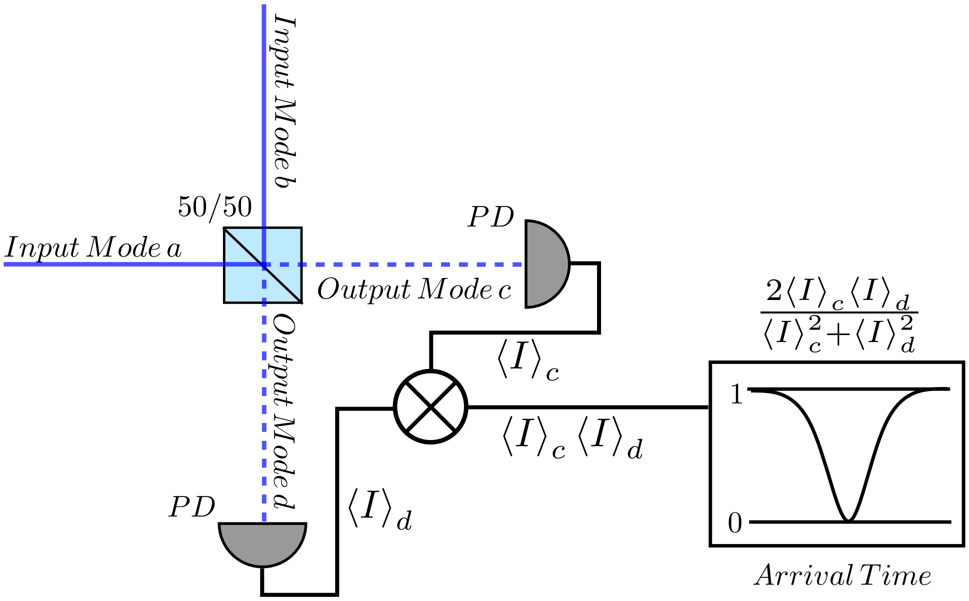

Figure 6.1: If a photon from input mode a and an identical photon from input mode b hit the beam splitter at exactly the same time then one measures the coincidence of both output detectors measuring a photon, the result will be zero due to bosonic statistics.

on two of the ports of the beam splitter. On the output ports, place two-single photon detectors. If you vary the amount of time it takes for one of the photons to hit the beam splitter, there will be a specific time at which point there will no longer be coincident counts on the detectors, see Fig. 6.1. This is known as the Hong-Ou-Mandel dip, and it is a consequence of the interference of the photon wavepackets at the beam splitter[1]. One way to view this experiment is to consider the beam splitter as a unitary rotation of input modes to output modes,

---

[1] If this dip exceeds 50% this effect exceeds the interference one might expect of classical correlations.

$$\hat{a}^\dagger = \frac{\hat{c}^\dagger + \hat{d}^\dagger}{\sqrt{2}} \tag{6.1}$$

$$\hat{b}^\dagger = \frac{\hat{c}^\dagger - \hat{d}^\dagger}{\sqrt{2}} \tag{6.2}$$

Because these operators are bosonoic they commute with each other, specifically $[c^\dagger, d^\dagger] = 0$. Then if we consider the input state acting on the vacuum to generate the two input photons, we end up with input and output states given by,

$$\begin{aligned} \hat{a}^\dagger\hat{b}^\dagger |0_a, 0_b\rangle &\rightarrow \frac{1}{2}(\hat{c}^{\dagger 2} + \hat{d}^\dagger\hat{c}^\dagger - \hat{c}^\dagger\hat{d}^\dagger - \hat{d}^{\dagger 2}) |0_c, 0_d\rangle \\ \hat{a}^\dagger\hat{b}^\dagger |0_a, 0_b\rangle &\rightarrow \frac{1}{2}(\hat{c}^{\dagger 2} - \hat{d}^{\dagger 2}) |0_c, 0_d\rangle \\ |1_a, 1_b\rangle &\rightarrow \frac{|2_c, 0_d\rangle - |0_c, 2_d\rangle}{\sqrt{2}} \end{aligned} \tag{6.3}$$

In other words, when measuring the output, there will be no coincident detection at different output ports. Just to highlight the point, if the particles interfering on the beam splitter were fermions, which anti-commute $\{c^\dagger, d^\dagger\} = 0$, then the cross terms would not cancel. In fact they would be the only terms due to the Pauli exclusion principle, and there would only be coincident counts on the detectors. The resulting output state is an entangled state of the two modes. This basic interference is one way linear optical quantum information processors generate entanglement [69]. It is also a perfect test for the bosonic nature of our phonons. Good Hong-Ou-Mandel contrast is indicative of good bosonic statistics; furthermore it requires us to generate specific Fock states and be able to read them out.

To give a more general mathematical description of this phenomena [70], we can start with two photons which have a joint Gaussian pulse shape β impinging on a beam splitter with unknown transmission (T) and reflection (R) coefficients. The creation and annihilation operators for the input state can be described as an integral over the pulse time, with corresponding creation operators acting on the vacuum state,

$$|1_1, 1_2\rangle = \int dt \int dt' \beta(t,t') \hat{a}_1^\dagger(t) \hat{a}_2^\dagger(t') |0\rangle \tag{6.4}$$

Where β is given by the overlap of the spectral amplitudes, ζ, normalized in the following way,

$$\beta(t,t') = \zeta(t)\zeta(t') \tag{6.5}$$

$$\zeta(t) = \left(\frac{2\Delta^2}{\pi}\right)^{\frac{1}{4}} e^{-i\omega_0 t} e^{-\Delta^2(t_0-t)^2} \tag{6.6}$$

$$1 = \int dt \int dt' |\beta(t,t')|^2 \tag{6.7}$$

$$1 = |R|^2 + |T|^2 \tag{6.8}$$

The Δ in the above expression is the spectral bandwidth of the light. In terms of the output operators, the input operators are defined as,

$$\hat{a}_1^\dagger(t) = R\hat{a}_3^\dagger(t) + T\hat{a}_4^\dagger(t) \tag{6.9}$$

$$\hat{a}_2^\dagger(t) = T\hat{a}_3^\dagger(t) + R\hat{a}_4^\dagger(t) \tag{6.10}$$

We can write the integration above in terms of the output operators to obtain,

$$\begin{aligned} |1_1, 1_2\rangle = \int dt \int dt' \frac{1}{2} RT \left[\beta(t,t') + \beta(t',t)\right] \left[\hat{a}_3^\dagger(t)\hat{a}_3^\dagger(t') + \hat{a}_4^\dagger(t)\hat{a}_4^\dagger(t')\right] \qquad (6.11) \\ + \left[R^2\beta(t,t') + T^2\beta(t',t)\right] \left[\hat{a}_3^\dagger(t)\hat{a}_4^\dagger(t') + \hat{a}_4^\dagger(t)\hat{a}_3^\dagger(t')\right] |0\rangle \end{aligned}$$

From the form of the operators, we can conclude that there will be two cases that will be interesting: The case where we get coincident detection on the output ports, $\langle 1_3, 1_4|$, and those in which we do not, $\langle 2_3, 0_4|$ and $\langle 0_3, 2_4|$. The probability of the first case is given by,

$$\begin{aligned}
\langle 1_3, 1_4 | 1_1, 1_2 \rangle &= \int dt \int dt' \left[R^2 \beta(t,t') + T^2 \beta(t',t) \right] && (6.12)\\
&\left[\langle 1_3, 1_4 | \, \hat{a}_3^\dagger(t) \hat{a}_4^\dagger(t') \, |0\rangle + \langle 1_3, 1_4 | \, \hat{a}_4^\dagger(t) \hat{a}_3^\dagger(t') \, |0\rangle \right] &&\\
&= \int dt \int dt' R^2 \beta(t,t') + T^2 \beta(t',t) && (6.13)\\
P(1_3, 1_4) &= | \langle 1_3, 1_4 | 1_1, 1_2 \rangle |^2 && (6.14)\\
&= | \int dt \int dt' R^2 \beta(t,t') + T^2 \beta(t',t) |^2 && (6.15)\\
&= R^4 \int dt \int dt' \beta^*(t,t') \beta(t,t') + T^4 \int dt \int dt' \beta^*(t',t) \beta(t',t) && (6.16)\\
&+ |R|^2 |T|^2 \int dt \int dt' \left[\beta^*(t,t') \beta(t',t) + \beta^*(t',t) \beta(t,t') \right] &&\\
&= |R|^4 + |T|^4 + 2|R|^2 |T|^2 |J|^2 && (6.17)\\
|J|^2 &= \int dt \int dt' \beta^*(t,t') \beta(t',t) && (6.18)
\end{aligned}$$

By completing the square and using the normalization convention defined above we get a term that looks like,

$$P(1_3, 1_4) = 1 - 2|R|^2 |T|^2 (1 + |J|^2) \quad (6.19)$$

Similarly we can look at the probability that both photons exit the same port of the beam splitter,

$$\langle 2_4, 0_4 | 1_1, 1_2 \rangle = \langle 0_4, 2_4 | 1_1, 1_2 \rangle = \int dt \int dt' \frac{\sqrt{2}}{2} RT \left[\beta(t,t') + \beta(t',t) \right] \tag{6.20}$$

$$\begin{aligned} P(2_3, 0_4) = P(0_3, 2_4) &= | \langle 2_3, 0_4 | 1_1, 1_2 \rangle |^2 = | \langle 0_3, 2_4 | 1_1, 1_2 \rangle |^2 && (6.21) \\ &= \frac{2}{4} |R|^2 |T|^2 \int dt \int dt' | \left[\beta(t,t') + \beta(t',t) \right] |^2 && (6.22) \\ &= |R|^2 |T|^2 \left(1 + |J|^2 \right) && (6.23) \end{aligned}$$

For the special case of a 50/50 beamsplitter, where $|R|^2 = |T|^2 = \frac{1}{2}$, the probabilities for each case reduces to,

$$\begin{aligned} P(2_3, 0_4) = P(0_3, 2_4) &= \frac{1}{4} \left(1 + |J|^2 \right) && (6.24) \\ P(1_3, 1_4) &= \frac{1}{2} (1 - |J|^2) && (6.25) \end{aligned}$$

We can see that $|J|^2$ is the overlap integral of the photon wavepackets in time. For the case in which both of these photons have perfect overlap in arrival time and have the same center frequency, ω_0, we say the photons are identical and the overlap integral $|J|^2 = 1$. For this case, the probability for both photons to exit the same port is $P(2_3, 0_4) = P(0_3, 2_4) = \frac{1}{2}$ and the probability that they exit different ports vanishes, $P(1_3, 1_4) = 0$. This gives rise to the aforementioned Hong-Ou-Mandel dip in coincident counts as the photon arrival time of one of the wavepackets is scanned.

6.2 Hong-Ou-Mandel Phonon Example

For the phonons we create, it can be challenging to create a direct analog of this beam splitter interaction. Essentially, this requires generating an $x_i \cdot x_j$ coupling of the modes we want to mix. This type of non-linearity requires us to introduce a gradient between normal modes. That can be difficult without perturbing the ions motion in such a way as to ruin the Fock states we have prepared. There are three approaches worth mentioning.

The first approach studied experimentally, but not in this context, involves driving a gradient of field electric field at the difference frequency between two modes [71–74]. This gradient needs to spatially overlap with both modes of interest, and the gradient itself will determine the strength of the coupling. This has been shown in a micro-fabricated trap where mixing was driven between the in and out of plane normal modes. There are a few reasons why we find this approach unappealing for our experiments. First, it is sometimes challenging to drive the nominally DC potentials without inducing micro-motion and subsequent heating of the normal modes.

More problematic is the fact that even though the trap electrodes are small, on the order of 60 μm and they are close $\approx 90\mu$m away from ions, the ions in a chain are spaced by $\approx 5\mu$m. This means that there needs to be a strong field gradient between ions created from electrodes that are an order of magnitude farther away. In practice this means that extremely large voltages must be applied to electrodes to get any non-negligible coupling. Because our trap has delicate features, for example the trench capacitors used to eliminate RF pick-up on the DC electrodes, we are limited to no more than 10 V on the DC electrodes. In simulations we estimated this would allow us to get less than a 10 Hz coupling between different normal modes an the same trapping axis. One could do better by coupling in and out of plane modes, however, we would then have to cool twice as many modes which might increase the length of experiments such that heating effects would start to set in before we could see any interference.

The second and more promising technique involves weakening the axial trap depth, which is equivalent to weakening the springs between ions by increasing their distance from one another [75]. If the distance is made large enough and a single ion is addressed[2] then the addressed mode is more of a local mode than a collective mode [51]. This local excitation will naturally begin to mix with the other local modes, and this mixing can be used as a beam splitter between local phonons when viewed at certain times. As a classical analog, think of beads connected axially by springs. When the springs are strong and a bead is displaced in the transverse direction and all the beads participate in the resulting harmonic motion, this is exciting a normal mode of motion. However, if the springs between beads are incredibly weak, then a bead displaced will oscillate at its center of mass frequency before the excitation slowly couples to the other beads. An alternative interpretation is to consider the fact that the normal modes of motion are the eigenstates of the confining Hamiltonian, while the local modes are superpositions of the normal modes and since they are not eigenstates the local modes, they will undergo time evolution

---

[2] This is much more easily accomplished now that the ions are separated by much larger distances

into one another at a rate given by the difference in their associated energies. The hopping between the local modes can be thought of as a beam splitter between local modes. This hopping between local modes goes like,

$$t_{i,i+1} \propto \frac{\omega_{\hat{z}}^2}{2\omega_{\hat{x},\hat{y}}} \tag{6.26}$$

This coupling has been shown to exhibit HOM type interference using two trapped Ca$^+$ ions in a macro-fabricated trap [75]. The main issue with this type of coupling is that it is very difficult to engineer the coupling exactly. It is difficult to modify the DC potential without inducing heating, in the experiments where this was demonstrated the potential was not changed and they observed the phonons hop back and forth. But if you want to stop the hopping for readout or to freeze the state in a given phonon configuration, this can be challenging to do with DC electrodes.

The way in which we are trying to induce this coupling relies on our Raman interaction. In Chapter four, we wrote down the coupling, for an arbitrary length ion chain, of the ion chain motion to light. Before making the Lamb-Dicke approximation that Hamiltonian took the form,

$$\tilde{H}_I = \sum_j \Omega \hat{\sigma}_j^+ e^{i\omega_{HF}t} \prod_i e^{[i\eta_{i,j}(\hat{a}_i^\dagger e^{i\omega_i t} + \hat{a}_i e^{-i\omega_i t})]} e^{-i\omega_\Delta t} + \text{h.c.} \tag{6.27}$$

By saying that the parameter η was small, we expanded the exponential in a Taylor series. However, not only are the terms in the expansion separated in strength by η, they are also spectrally resolved by combination of the normal mode frequencies. Therefore there are terms that are higher order in η which separate spectrally and can be driven [76]. More concretely, there exists a term that is second order in η that has the form,

$$\mathcal{O}(\eta^2) \rightarrow \tilde{H}_I^{RWA} = \sum_j \eta_{i,j}\eta_{k,j}\Omega(\sigma_j^+ \hat{a}_i \hat{a}_k^\dagger + \sigma_j^- \hat{a}_i^\dagger \hat{a}_k)$$

Once an appropriate rotating wave approximation is made, requiring the driving field to be at the difference frequency of the two modes of interest $\omega_\Delta = \pm|\omega_i - \omega_k|$. This term looks a lot like the traditional beam splitter Hamiltonian,

$$\tilde{H}_{BS} \propto (\hat{a}_i \hat{a}_k^\dagger + \hat{a}_i^\dagger \hat{a}_k) \tag{6.28}$$

If we can drive two colors, one color at the positive difference frequency, and one at the negative difference frequency then we can drive a Hamiltonian which is identical to this beam splitter Hamiltonian for the phonon modes, see Fig. 6.3

$$\tilde{H}_{HOM} = \sum_j \eta_{i,j}\eta_{k,j}\Omega(\sigma_j^+ + \sigma_j^-)(\hat{a}_i \hat{a}_k^\dagger + \hat{a}_i^\dagger \hat{a}_k) \tag{6.29}$$

This is the term we are attempting to drive when we induce our HOM coupling. The reason we find this coupling scheme appealing is that in principle we can drive many different interference terms by adding additional frequencies to our Raman beatnote, which is relatively trivial. It is also an externally driven interaction, which allows us to turn on and off the coupling at will. This would in principal allow us

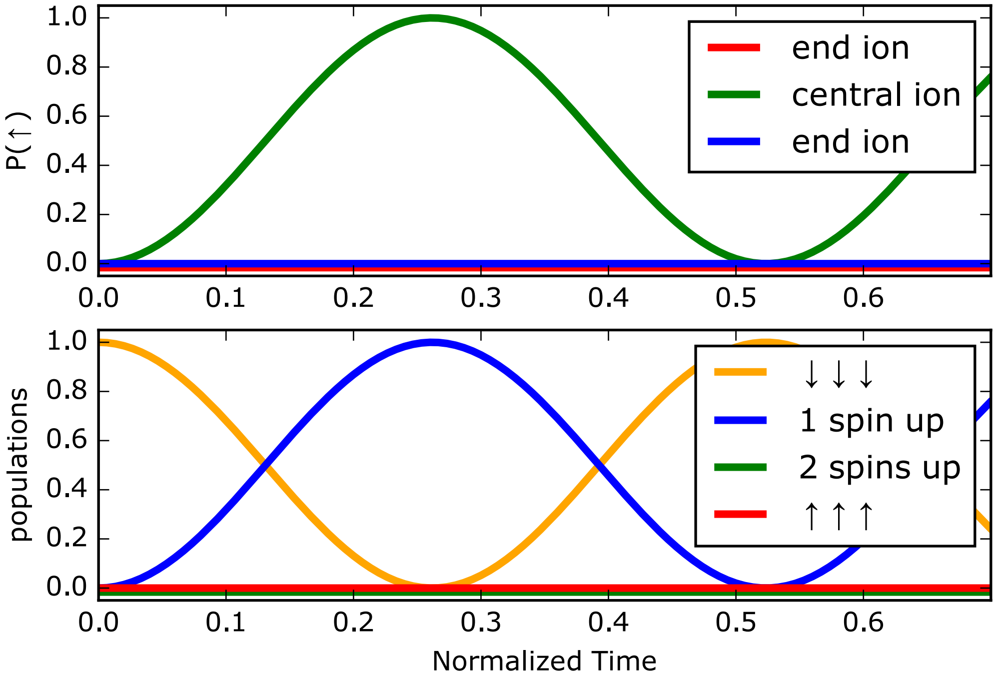

Figure 6.2: Theory plots describing the evolution, under the Hamiltonian $\tilde{H}_{HOM} = \sum_j \eta_{i,j}\eta_{k,j}\Omega(\sigma_j^+ + \sigma_j^-)(\hat{a}_i\hat{a}_k^\dagger + \hat{a}_i^\dagger\hat{a}_k)$, of the quantum state as a function of drive time. The upper plot shows how the individual spins should flip in a three ion chain. The bottom plot dipicts the evolution of the spin manifolds. The normalized time is a result of setting $\eta_{i,j}\eta_{k,j}\Omega = 1$ when calculating the state evolution.

to tune the visibility of the beam splitters we are creating. Finally, this type of interaction only relies on the normal modes; we are not required to modify the DC potential, and incur the heating that might result. Finally, once the interaction is turned off the modes will stop evolving which makes measurement less daunting.

6.2.1 Results

We have attempted to drive the interference term detailed above, and although our results thus far are not in agreement with theory, they give us some hope for a way forward and hint at what are our current limitations. Using the tools developed

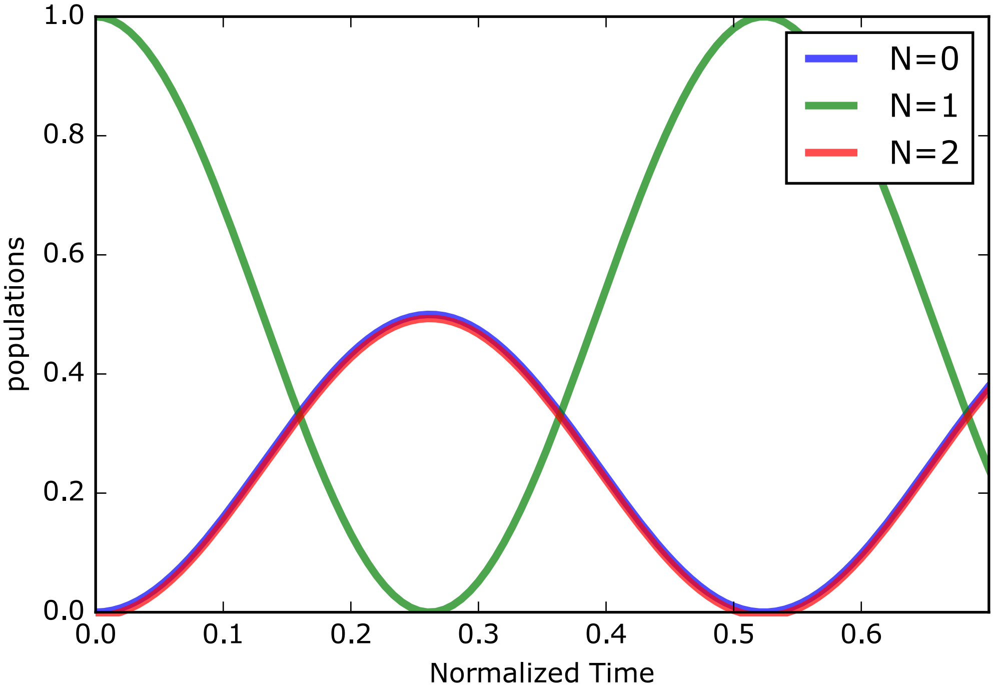

Figure 6.3: Theory plots describing the evolution of the quantum state as a function of drive time. This plot shows the evolution of the motion state for one of the modes as function of drive time. Where the red curve is the evolution of the $|n=2\rangle$ phonon state, green show the$|n=1\rangle$ phonon state, and blue is the $|n=0\rangle$ phonon state. In the beginning we initialize in $|n=1\rangle$ and this state oscillates between this and $|n=0\rangle + |n=2\rangle$, very similar to a Hong-Ou-Mandel experiment. The normalized time is a result of setting $\eta_{i,j}\eta_{k,j}\Omega = 1$ when calculating the state evolution.

in the previous chapters, we have tried to initialize our chain of three ions in the state,

$$|\Psi\rangle = |\psi\rangle_{spin} |\varphi\rangle_{motion} \tag{6.30}$$

$$= |\downarrow, \downarrow, \downarrow\rangle |1, 0, 1\rangle \tag{6.31}$$

When we drive the HOM term, we are going to look at the spin component of the three ion state, see Fig. 6.2. By using spin as a witness, we should expect to see flopping between the all spin down state $\psi_0 = |\downarrow, \downarrow, \downarrow\rangle$ and the one spin flipped up manifold $\psi = |\uparrow, \downarrow, \downarrow\rangle + |\downarrow, \uparrow, \downarrow\rangle + |\downarrow, \downarrow, \uparrow\rangle$, without any two spins being flipped simultaneously. This condition comes from the coupling we are trying to drive, which can only exchange one beam splitter excitation with one spin flip excitation. If we start with $\phi_0 = |1, 0, 1\rangle$, then the only other coupled state of the phonons is $\phi = |2, 0, 0\rangle - |0, 0, 2\rangle$.

What we observe is that we can induce some mixing, however the coherence of this mixing appears to be limited, see Fig. 6.4. What is interesting is that the decoherence we observe is still confined to the spin manifold we expect to couple to, which is not what we would expect if heating were the limiting factor. In fact, if the purity of the phonon state was limiting us, we would expect that the other spin manifolds, two spins and all spins being flipped up, would play a role in the dynamics. Our ability to create the $\phi_0 = |1, 0, 1\rangle$ Fock states of motion is all that limits how many spins are flipped. Our current working theory as to why the coherence is limited in this manner has to do with the stability of transverse mode frequencies. In Chapter 2, we showed that the transverse mode frequency is proportional to the RF voltage, $\omega_{x,y} \propto V_{RF}$ and as discussed previously in this chapter, the HOM terms we are driving are of order η^2. For fixed interaction time this means that these terms are a factor of η more narrow than a RSB or BSB. To maintain coherence the transverse secular frequencies must be stable to better than a fraction of the linewidth of those transitions. This means that the V_{RF} must be stable to much less than the linewidth of the HOM term. We estimate this level of

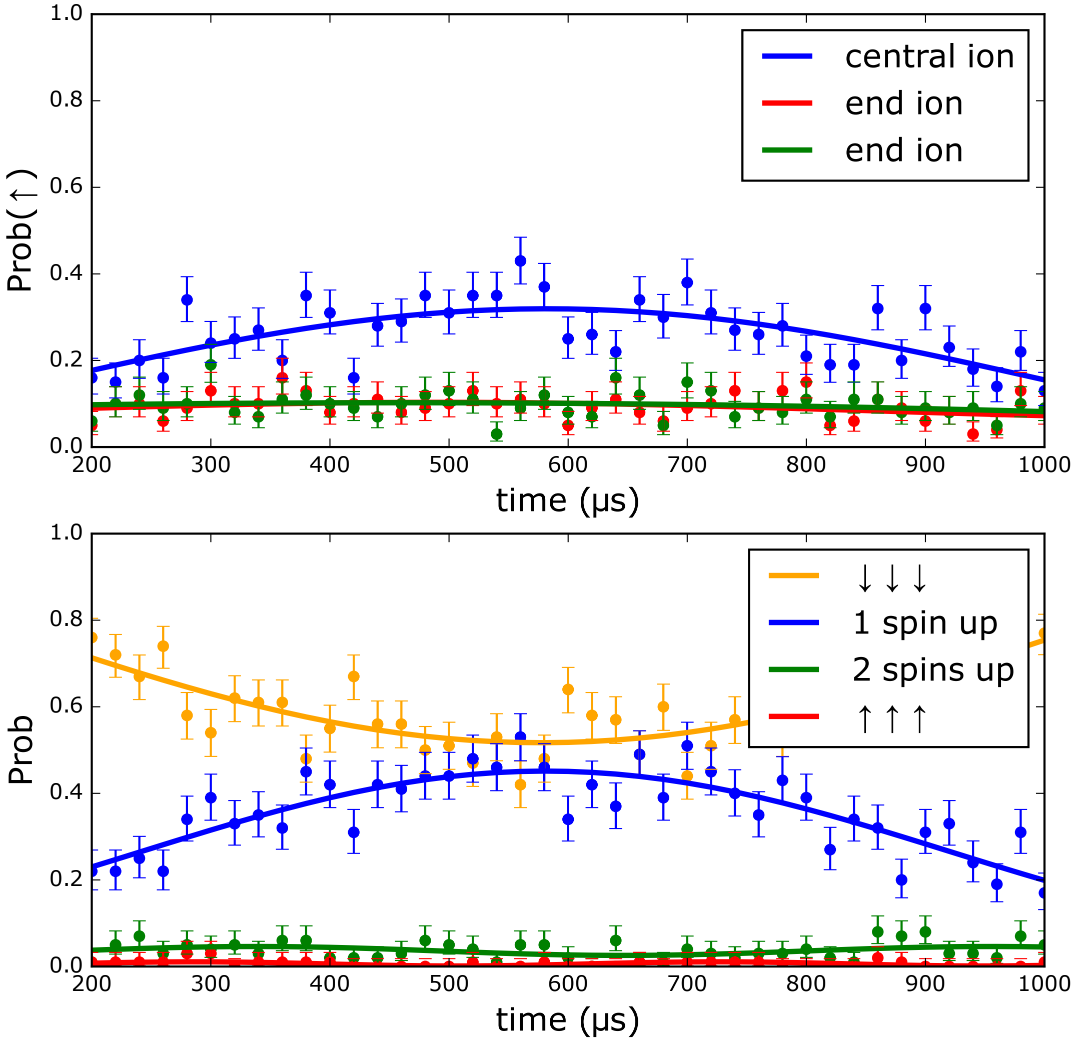

Figure 6.4: The state is initialized to $\psi_0 = |\downarrow,\downarrow,\downarrow\rangle\,|1,0,1\rangle$. By driving the HOM term, we see qualitatively what we expect, namely only the one spin flipped manifold is participating in the interaction. The solid lines on the lower curves are $\sin^2$ fits to the data of the form $A\sin^2(\omega t+\phi)+C$. Where A, ω, ϕ, and C are all fit parameters. The average reduced χ^2 for the fits on the upper plot is 0.887, for the lower plot the average reduced χ^2 is 0.785. Error bars are again calculated from a binomial distribution.

stability as,

$$V_0 = \omega_{x,y} \tag{6.32}$$

$$\delta\omega < \frac{\gamma}{10} \tag{6.33}$$

$$\delta\omega = \frac{\omega_{x,y}}{V_0}\delta V \tag{6.34}$$

$$\delta V < \frac{\gamma}{10\omega_{x,y}} V_0 \tag{6.35}$$

Where the term γ is the linewidth of the RSB or BSB, experimentally these transitions are 50 kHz wide with a center frequency of 2.7 MHz, which means the HOM term should be approximately 5 kHz wide. This means that the voltage must be stable to a part in 10^4 for us to be able to drive coherent flopping:

$$\begin{aligned}
\frac{\delta V}{V_0} &< \frac{\gamma}{10\omega_{x,y}} && (6.36)\\
&< \frac{5\text{kHz}}{10 \cdot 2.7\text{MHz}} && (6.37)\\
&< 2 \cdot 10^{-4} && (6.38)
\end{aligned}$$

From the data we have taken for the HOM drive so far we have much more like a part in 10^3 stability. To verify this, we took overlapping Allan deviation (OVAD) measurements of the frequency of the BSB transition [43]. We accomplish this by doing Ramsey spectroscopy. We applied a $\pi/2$ pulse on a cold BSB and wait a time τ and apply another $\pi/2$ pulse. By varying the delay τ, we obtained a fringe which we can fit to determine the frequency of the BSB. For our purpose, it is important to make the time $\tau \geq 200\ \mu$ s as this is the relevant time for our fastest HOM drive time. By repeating this measurement as fast as we can over an hour or more, we were able to calculate overlapping Allan deviations for the carrier as well as the BSB. The overlapping Allan deviation is given by [77],

$$\sigma_y^2 = \frac{1}{2m^2(M-2m+1)} \sum_{j=1}^{M-2m+1} \left\{ \sum_{i=j}^{j+m-1} [y_{i+m} - y_i] \right\}^2 \tag{6.39}$$

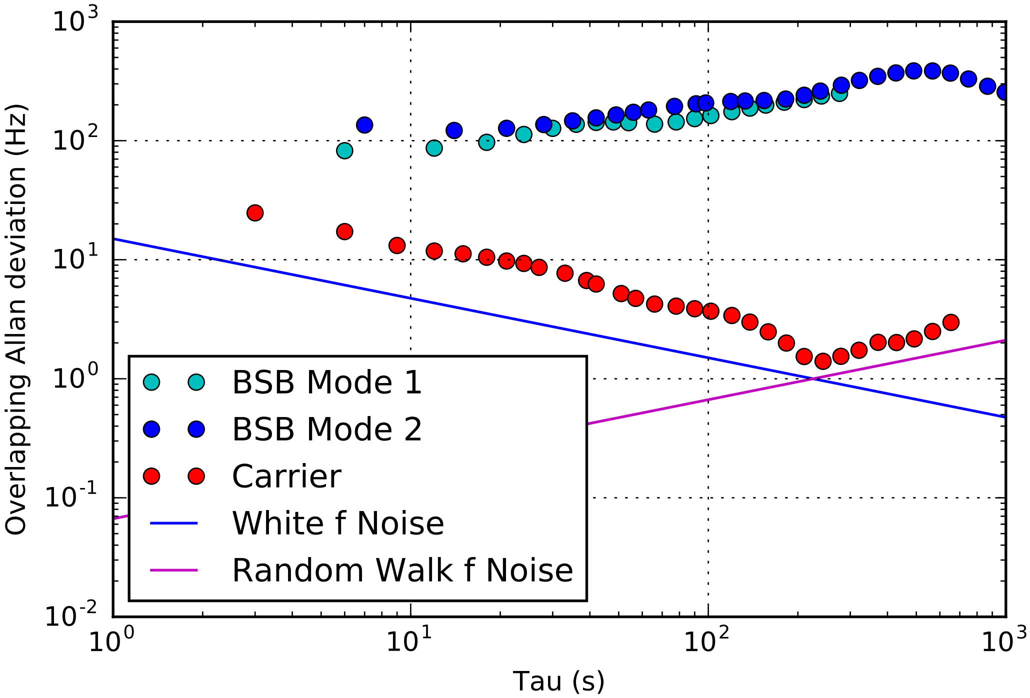

Figure 6.5: Allan deviation of the frequency of the b_0 and b_1 modes via Ramsey spectroscopy, we can see that the drifts in the sidebands are a limiting factor in performing the desired HOM interaction.

When compared to the carrier the BSB has substantially worse stability, which means the dominate drift is not the beatnote itself, see Fig. 6.5. We see that at the earliest time scales we can measure the BSB is already drifting with a slope similar to a random frequency walk. This implies that over a few seconds the BSB has moved by 100 Hz, because the distillation is probabilistic these experiments can take minutes from the first scan point to the last scan point. If the sidebands are moving by a part in 10^3 during this time, as the last few points in the plot suggest, this accounts for at least a portion of our loss of contrast.

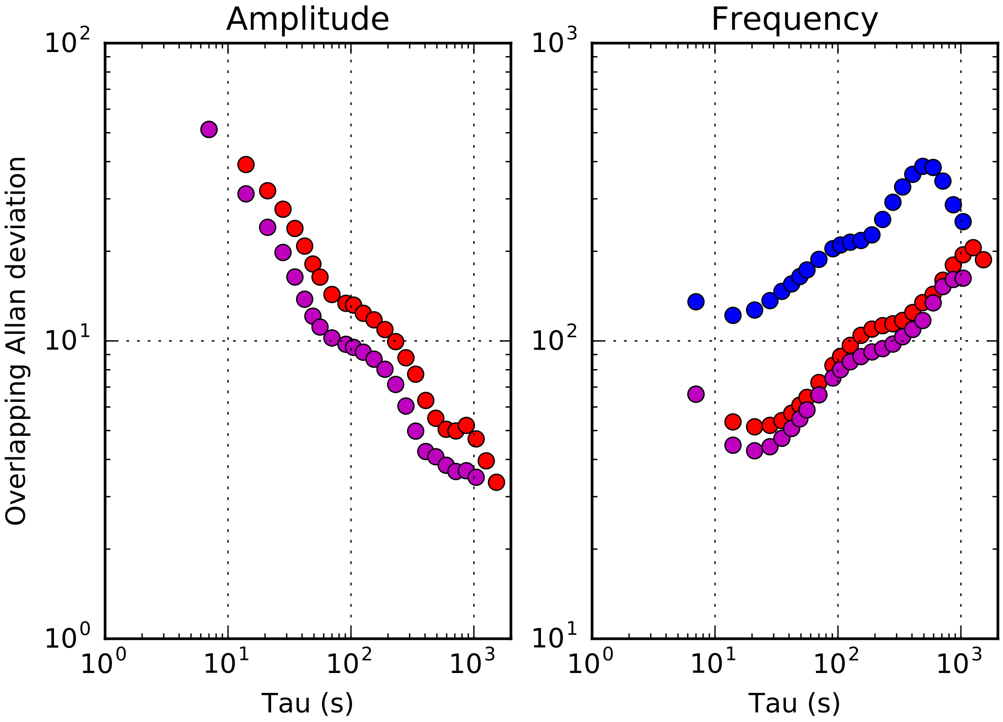

Figure 6.6: Allan deviation after better stabilization. The blue points are the same as the points in Fig. 6.5, the pink and purple points represent recent improvements in the stabilization of the mode frequencies. Where we have also measured the stability of the amplitude of Ramsey fringe we measure, this gives us an indication of the intensity drift of the beatnote. This is on the same order as the best stabilization achieved for similar stabilization circuits, and we still believe this may be the limiting factor in driving interference.

We think this is by far the limiting factor in driving our HOM terms. Recently, we have been trying to improve on the stabilization of this frequency by better stabilization the RF drive frequency. In doing so, we have made some improvements on the above results, see Fig. 6.6. Specifically we have temperature stabilized the helical resonator as well at the rectifier we use. We also have integrated a part per million stable voltage reference into the locking circuitry, this is done to stabilize the setpoint of the servo controller. However, we still believe this to be our limiting factor. This in fact is what motivated us to try and the develop phonon excitation readout discussed in section 5.4. This would allow us to look at the external degree of freedom as well as the spin degree of freedom.

Chapter 7: Outlook

7.1 Future Improvements

The intent of this chapter is to discuss some of our strategies for mitigating the problems we have encountered so far and try to motivate why these tool could be interesting in the future. We need to find a way to increase the coherence of the HOM interference we have seen thus far. We have begun by temperature stabilizing all the components in the RF stabilization circuit as well as try and find what component in that circuit [1] is inducing the most noise.

The biggest hurdle will be any out of loop noisy reactive elements in the vacuum chamber itself. In principle, if the RF leads are moving in the chamber this could change the line inductance and lead to a shift between measured tap voltage and trap voltage. This shift only has to be a part in 10^3 before it would account for all of the drifts we see in the experiment. If there is noise in the RF voltage picked up after the resonator, the feedback to the resonator itself will be limited in the bandwidth to the linewidth of the resonator. With feedback before the resonator, precisely because the helical resonator is a very good filter, it will be difficult to address frequencies that couple onto the RF line after the resonator.

---

[1] Discussed fully in Chapter 3.3.2.2.

There are two approaches we have devised to address these issues. We can move away from using transverse modes and instead couple to the axial modes of motion. This has two advantages, as stated in Chapter 2: First, the axial modes depend on the DC trapping voltages, which are much easier to stabilize and can be heavily low-pass filtered. Secondly, all of the mixing terms will have similar difference frequencies, which may make future experiments less challenging. The biggest problem with the axial modes is that they are at lower frequencies. Because the heating rate as well as the Doppler limit depend on this frequency, it can be much harder to cool these modes. Despite these drawbacks, with the voltages we are currently applying, we think we should be able to achieve axial frequencies of approximately 1 MHz.

The most invasive change, which would require us to break vacuum and replace the trap with a different trapping architecture, would be to arrange true individual addressing. The way in which we would achieve this is by making use of a new trap design, the HOA trap, where the NA from the side of the trap is around 0.25. This trap also has a slot through the trapping structure which allows tightly focused beams to be sent through the trap. This change is planned to occur in the next year, and this will require most of the experiment be dismantled for a few months. Luckily, the infrastructure of optics and electronics can readily be re-aligned to the new chamber assembly when it is under vacuum.

In conclusion, we have demonstrated a toolset for initializing and reading out the external degrees of freedom in a trapped ion chain. We do this with the hope of being able to utilize this additional quantum resource in experiments that require sampling from bosonic distributions[2]. This experiment is of interest because it is classically very difficult, P#-complete, to determine the probability of a specific output configuration from a bosonic distribution of output configurations derived from a network of linear beam splitters [54, 78]. If an experiment can bound that probability for a sufficiently large number of output modes, even to a multiplicative factor, it would be interesting to several communities of scientists [56].

---

[2] See Appendix B for more details on Boson Sampling.

Appendix A: Laser locking

Locking the frequency of our laser sources is of paramount importance to performing high fidelity operations. In previous chapters, there was a discussion of how we lock the frequency of the Raman beatnote, but the locks used to stabilize the frequencies of our various CW laser sources was left for this appendix. The reason why this is so challenging is two-fold. Firstly, we are trying to lock a wide spectral range of wavelengths from 369 nm to 935 nm[1]. Secondly, the 369 nm light is far enough into the blue that certain traditional locking schemes can prove difficult. This appendix is intended to discuss the several ways we have attempted to lock our lasers, as well as the planned improvements to our laser locking scheme.

A.1 Wavemeter Locking

The current, unsustainable, locking scheme we are using involves a wavemeter from High Finesse, this instrument has an accuracy of 50 MHz around the 369 nm wavelength, a precision of approximately 5 MHz, and returns a measurement of wavelength approximately every 2 seconds. These wavemeters operate by coupling light to a series of Fizeau interferometers of different lengths. By comparing

---

[1] Where some experiments in our group have Ba^+ wavelengths peppered throughout that region.

the interference pattern from each of these interferometers, software calculates the wavelength based on an interference pattern of a known calibration wavelength. The operational implementation of this lock is trivial, the wavemeter, a commercial product, determines the wavelength of the light you send to it via an optical fiber. One can then use that reading to feedback to the frequency of an ECDL by adjusting the cavity length or the diode current. The main issues with this type of lock involves timing, and for our purposes precision.

In the ion trapping community, as long as you can trap one ion then you can always use the ion as an accurate reference in this case the wavemeter. Therefore, we do not necessarily need high accuracy, just high precision. The problem, arises when you want to lock multiple wavelengths with this method using only one wavemeter. The cited precision specifications are only valid within a 2 nm band around the calibration wavelength. More problematic is how to couple all of these wavelengths into the same device. Until recently, there was only one port into these wavemeters, which meant a switch needed to be used. The switches generally sold for these devices work by taking many input fibers and directing them sequentially onto an output coupler using a MEMS mirror.

There are two problems with this. First, to be broadband the switch uses multimode optical fiber. By sending multimode light into the wavemeter, the precision specification will be degraded up to two orders of magnitude. The second problem is that the time it takes to switch between wavelengths can dramatically impact the bandwidth of a feedback loop that is relying on a measurement from the wavemeter.

A.2 Locking via discharge cells

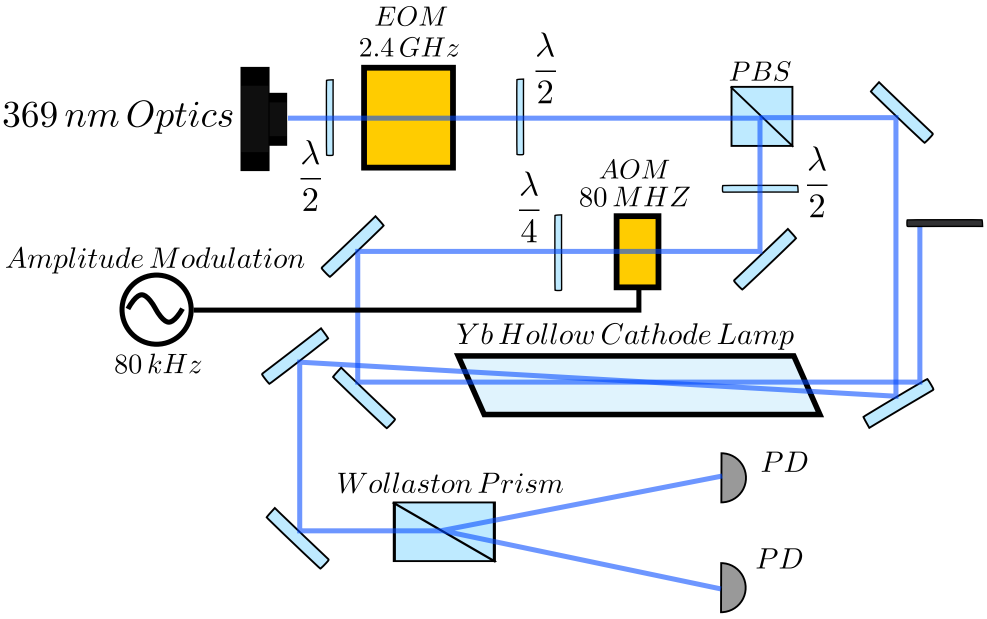

Figure A.1: The optics path for using a hollow cathode lamp in a polarization spectroscopy configuration. This requires interrogation of the ^{174}Yb$^+$ isotope. To shift the ^{174}Yb$^+$ line onto the ^{171}Yb$^+$ $S_{1/2} \rightarrow P_{1/2}$ resonance requires an EOM or another source of 369 nm light beatnote referenced to ^{174}Yb$^+$. Because the ion signals in the cell are so small we use lock-in amplification by modulating the power of the pump light via an AOM to achieve sufficient signal strength.

If for a moment we wish to only lock the 369 nm line and we wish to do so in a very accurate way, we can think about locking the laser to a cell of Yb$^+$ ions. This is most readily achieved by taking a hollow cathode lamp of Yb and running a large amount of current through the lamp, 10-30 mA, to create a plasma of Yb. Once a plasma is achieved, 369 nm light can be locked to the atoms in whatever way is most convenient. The most commonly used lock for this setup is a polarization lock [79–81]. This lock works by comparing the differential absorption of polarized light as the light is swept over resonance. By comparing the amplitude of transmitted light of different polarizations, a dispersive curve can be obtained with a zero crossing at the peak of resonance. This works because the presence of the pump changes the proportion of absorbed probe light of different polarizations. We can see this is we follow a derivation of transmitted intensity [82]. First, we note that a linearly polarized field in the circular polarization basis is of the form,

$$\boldsymbol{E} = E_0 \begin{pmatrix} \cos\phi \\ sin\phi \end{pmatrix} = E \left\{ \frac{e^{-i\phi}}{2} \begin{bmatrix} 1 \\ i \end{bmatrix} + \frac{e^{i\phi}}{2} \begin{bmatrix} 1 \\ -i \end{bmatrix} \right\} \tag{A.1}$$

After passing through the cell, there will be different absorption of the two polarizations, where we are ignoring the birefringent effects of the windows. The probe beam will have an electric field.

$$\boldsymbol{E} = E_0 \left\{ \frac{e^{-i\phi}}{2} \begin{bmatrix} 1 \\ i \end{bmatrix} e^{-L(i\frac{\omega}{c}n_+ + \frac{\alpha_+}{2})} + \frac{e^{i\phi}}{2} \begin{bmatrix} 1 \\ -i \end{bmatrix} e^{L(i\frac{\omega}{c}n_- - \frac{\alpha_-}{2})} \right\} \tag{A.2}$$

$$= E_0 e^{\left[-i\left(\frac{\omega}{c}nL - i\alpha\frac{L}{2}\right)\right]} \left\{ \frac{e^{-i\phi}}{2} \begin{bmatrix} 1 \\ i \end{bmatrix} e^{i\Omega} + \frac{e^{i\phi}}{2} \begin{bmatrix} 1 \\ -i \end{bmatrix} e^{-i\Omega} \right\} \tag{A.3}$$

$$\Omega = \frac{\omega L}{8c} \left(4\Delta n - i\Delta\alpha\right) \tag{A.4}$$

Where the $\frac{\omega}{c}n$ term corresponds to the phase shift the light acquires passing through the gas. We define ω as the frequency of the light and n as the index of refraction of the gas. The absorption of the light is defined as $\alpha_{\pm}$. The measurement we want to make is a differential measurement of the two different polarizations in the linear basis. By using a Wollaston prism to spatially separate both polarization and then direct each onto one port of a differential photodiode we can make this differential measurement. In this case, the intensity of the signal we mesure will be,

$$I_{sig} = I_y - I_x \tag{A.5}$$

$$= I_0 e^{-\alpha L} \cos\left(2\phi + \frac{L\omega}{c}\Delta n\right) \tag{A.6}$$

We can use the Kramers-Kronig dispersion relation to relate $\Delta\alpha$ and Δn, $\Delta n = \frac{c}{\omega_0}\frac{x}{1+x^2}\Delta\alpha$, whose parameters we will define shortly. If we make the approximation that the accumulated polarization angle is small, and we set $\phi = \frac{\pi}{4}$ to maximize our sensitivity to polarization, we can make a small angle approximation. This leaves the following equation for the intensity of our signal,

$$I_{sig} = -I_0 e^{-\alpha L}\left(L\Delta\alpha_0 \frac{x}{1+x^2}\right) \tag{A.7}$$

$$x = \frac{\omega_0 - \omega}{\Gamma_0/2} \tag{A.8}$$

From this equation we see that we get a dispersive curve, where there is a zero crossing on resonance. We can use this curve to feedback to the frequency of our laser source. The problem here, is that there will be very few $^{171}\mathrm{Yb}^+$ ions and the signal from these atoms will be small and will also be convoluted with all the other isotope signals. This leads to a DC offset in the zero crossing of the line we are interested in locking. In practice, we found it necessary to apply EOM sidebands to the pump and probe light to align the signals derived from the much more prevalent $^{174}\mathrm{Yb}^+$ isotope with the $^{171}\mathrm{Yb}^+$ resonance we were interested in locking. What we found when using this lock was that sufficient lock performance, < 2 MHz drift of the laser as measure by the ion, required very specific parameters of the lock and that small deviations from these parameters could dramatically and adversely affect lock performance.

A.3 Transfer Cavity Locking

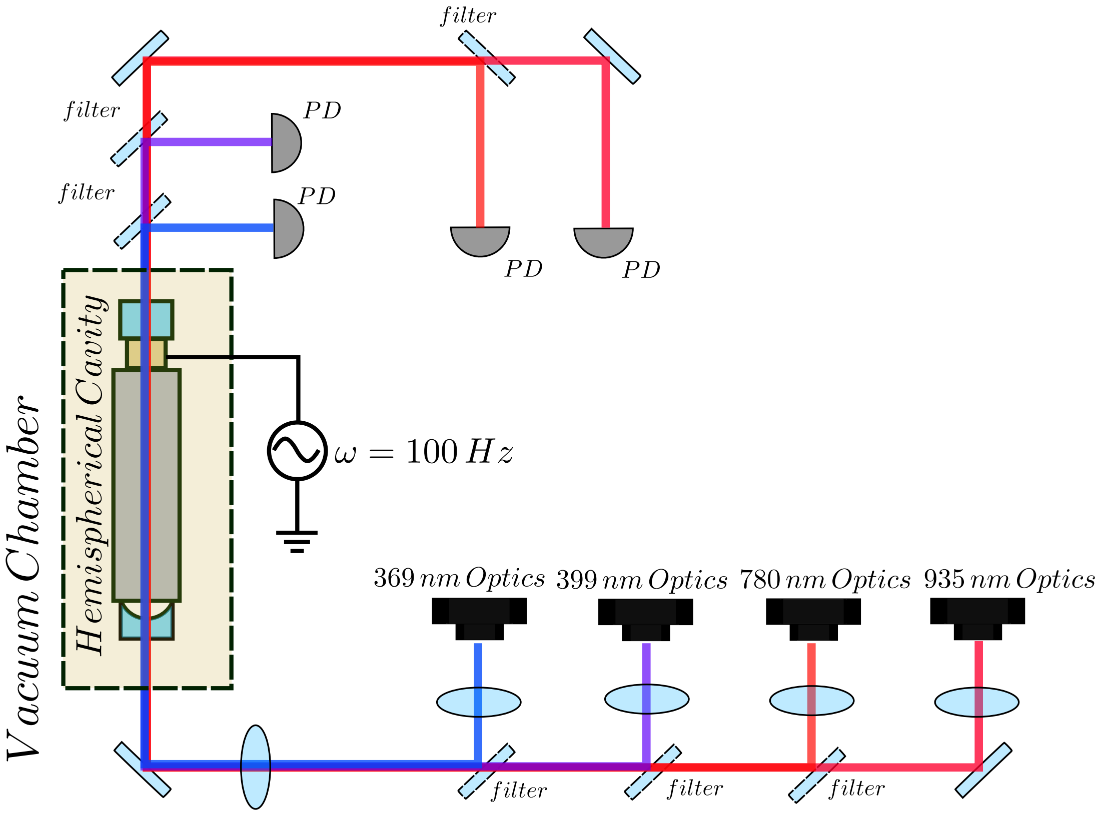

Figure A.2: The optics path for our scanning transfer cavity. The separation of wavelength can be accomplished with a variety of off the shelf filters. The photodiodes used depend on the electronics which digitize this signal. Ideally the response time of the photodiode is matched to the speed of the ADC to minimize dark counts.

The approach we are pursuing is to lock all of the lasers to a scanning optical cavity [83]. Light impinging on a Fabry-Perot interferometer will be resonant when the frequency of light satisfies the resonance condition, $\nu = m\frac{c}{2nL}$ where m

is a positive integer. By comparing the positions of resonances in a scan of the cavity length, we can compare frequencies of disparate laser sources. This can be accomplished while canceling the dependence of the resonance frequencies on the length of the cavity [84]. If one of these lasers is stabilized elsewhere to a known reference frequency, then we can use the cavity to stabilize the other laser sources to this laser. This can be seen if we compare the resonance condition for two adjacent cavity resonances of the reference laser to a laser we want to stabilize,

$$M\lambda_{ref} = 2n_{ref}L_0 \tag{A.9}$$

$$M\lambda_{ref} + \frac{\lambda_{ref}}{2} = 2n_{ref}(L_0 + \Delta L_0) \tag{A.10}$$

$$N\lambda_{sig} = 2n_{sig}\alpha\Delta L_0 \tag{A.11}$$

$$\tag{A.12}$$

Where ΔL_0 corresponds to scanned length of the cavity, which is less than the total length. The term $\alpha\Delta L_0$ is a position along that scanned length. The terms N and M are integers associated with the cavity resonance and n_{ref} is the index of refraction for the reference laser. In more physical terms, these equations represent the length change of the cavity necessary to see two reference lines, where we have arranged to have a resonance of the laser we are going to lock in-between these resonances. From these equations, we can solve for the wavelength of the signal light as a function of reference light.

$$L_0 = \frac{M\lambda_{ref}}{2n_{ref}} \tag{A.13}$$

$$\Delta L_0 = \frac{\left(M + \frac{1}{2}\right)\lambda_{ref}}{2n_{ref}L_0} - 1 \tag{A.14}$$

$$\lambda_{sig} = \lambda_{ref}\frac{n_{sig}}{n_{ref}}\frac{2M + \alpha}{2N} \tag{A.15}$$

Therefore if use the value of α as our set point, in a feedback loop we can effectively cancel out the length of the cavity, L_0, to first order. In practice, we must also stabilize the static length of the cavity L_0 to minimize the effect of pizeo non-linearities. We do this by stabilizing the value of Δ between the two reference resonances. This approach has the advantage that, in principle, we can lock all of the lasers to a single reference. Moreover, this can be accomplished without a large amount of overhead [2] in laboratory equipment. This is because the laser frequencies do not need to be tuned to the resonance as along as the element translating the mirrors of the cavity has enough throw to cover all the wavelengths.

The obvious problem with this lock is that the feedback bandwidth depends on the rate at which the scanned mirror can be translated. For larger mirrors, this rate can be truly limiting. In our current setup we use a 1 inch mirror and can only scan at a rate of approximately 100 Hz. However, by increasing the overhead involved with locking these lasers, one can do a Pound-Drever-Hall lock the cavity [85], operated as a static cavity, with much larger bandwidth.

---

[2] By overhead, I am referring to the AOMs, EOMs, and assorted electronics that would be needed to assure that the lasers are resonate with a static cavity.

Appendix B: Boson Sampling

In this section I am going to give a brief view of an experimentalist of how a Boson sampling experiment would work, and why it is interesting. Boson sampling is an interesting candidate experiment in the context of building a quantum device which can perform some simulation of computation that a classical computer can never hope to achieve. The experiment is as follows, given a set of Fock modes, we populate some known number state of those modes. If these modes then under go some form of coherent mixing, under a unitary transformation, $\hat{U}$, and the excitation occupation of the output modes is measured, the probability of getting population out on specific configurations of output channels depends on the matrix elements of $\hat{U}$ which mixed input modes to specific output modes. This probability is proportional to the permanent of a sub-matrix of $\hat{U}$ which does this mapping of input modes to output modes [56]. Specifically, this sub-matrix is constructed from elements of column vectors corresponding to the initial excitation, where the specific elements of these vectors are chosen corresponding to the rows of the measured output configuration. More formally, given the input state $|\psi\rangle$ the general output state will be $|\Gamma_{out}\rangle$,

$$|\Psi\rangle = |\psi_1, \psi_2, ..., \psi_M\rangle \tag{B.1}$$

$$|\Gamma_{out}\rangle = \sum_s c_s \left|\phi_1^{(s)}, \phi_2^{(s)}, ..., \phi_M^{(s)}\right\rangle \tag{B.2}$$

Where the sum is over all possible configurations of output excitations. The probability of measuring a specific output configuration is then given by,

$$P_s(\Phi_s|\Psi) = \frac{|\mathrm{Per}(\hat{U}^{(\Phi_s|\Psi)})|^2}{\prod_{j=1}^{M} \phi_j! \prod_{i=1}^{M} \psi_i!} \tag{B.3}$$

The reason why this experiment is interesting is that, from the above calculation we have shown that to calculate the probability of getting a specific output configuration requires calculating the permanent of a matrix, and in principle, this matrix can be large. This is significant because calculating the permanent is incredibly challenging classically, it belongs to the complexity class P#, and is in fact P#-complete. P# is not a class of decision problems like NP, instead it is a class of functions and in a sense can be related to a class of problems associated with determining the number of solutions to NP problems. Classically the most efficient algorithm for calculating the permanent of an $N \times N$ matrix is of order $\mathcal{O}(n^2 2^n)$. This implies that reasonably small systems can become intractable for a classical computer.

However, the experimental implementation of such an experiment seems feasible. In the linear optics community people are pursuing experiments in this vein for quite some time [56] [86]. Recently there have proposals on how to accomplish similar experiments with trapped ions [52]. The advantage to ions is that it might be easier to scale the number of ions, which would increase the number of modes and complexity of the classical computation. This is compared to scaling up the number of single photon sources, the bosonic excitations used in photonic boson sampler. The current state of the art in the photonics community is a 10 photon boson sampler [86], in the ion trap community no experimental implementations of boson sampling have been demonstrated.

To be clear, the experimental implementation would not hope to reconstruct the permanent of the unitary, $\hat{U}$. Such an experiment would take exponentially many measurements and would be highly limited by realistic error models [87, 88]. However, if an experiment can determine the probability of getting a given output mode configuration to within even some multiplicative factor for a sufficiently large $\hat{U}$; this might still constitute a demonstration of a quantum device performing a classically intractable problem. Even if an experiment was to demonstrate such a calculation the question of how to verify that the output probability was actually sampled from the unitary of interest is an open question [55]. However, there are some theoretical proposals and schemes to verify that the sampled distribution was not uniform [89, 90].

Bibliography

[1] M. Reiher, N. Wiebe, K.M. Svore, D. Wecker, and M. Troyer. Elucidating Reaction Mechanisms on Quantum Computers. *arXiv*, 1605(03590):1–28, 2016.

[2] Richard P. Feynman. Simulating physics with computers. *International Journal of Theoretical Physics*, 21(6-7):467–488, 1982.

[3] D Wineland, C Monroe, W Itano, D Leibfried, B King, and D Meekhof. Experimental issues in coherent quantum-state manipulation of trapped atomic ions. *Journal of Research of the National Institute of Standards and Technology*, 103(3), 1998.

[4] Rainer Blatt and David Wineland. Entangled states of trapped atomic ions. *Nature*, 453(7198):1008–1015, jun 2008.

[5] Thaddeus Ladd, Fedor Jelezko, Raymond Laflamme, Yasunobu Nakamura, Christopher Monroe, and Jeremy O'Brien. Quantum computers. *Nature*, 464(7285):45–53, 2010.

[6] Jacob Smith, Aaron Lee, Philip Richerme, Brian Neyenhuis, Paul W Hess, Philipp Hauke, Markus Heyl, David A. Huse, and Christopher Monroe. Many-body localization in a quantum simulator with programmable random disorder. *Nature Physics*, 12(10):907–911, jun 2016.

[7] R Blatt and C F Roos. Quantum simulations with trapped ions. *Nat. Phys.*, 8(4):277–284, 2012.

[8] D. Kielpinski, C. Monroe, and D. J. Wineland. Architecture for a large-scale ion-trap quantum computer. *Nature*, 417(6890):709–711, jun 2002.

[9] Yangchao Shen, Joonsuk Huh, Yao Lu, Junhua Zhang, Kuan Zhang, Shuaining Zhang, and Kihwan Kim. Quantum simulation of molecular spectroscopy in trapped-ion device. *arXiv*, pages 1–17, 2017.

[10] H.G. Dehmelt. Radiofrequency Spectroscopy of Stored Ions I: Storage. In *Advances in Atomic and Molecular Physics*, pages 53–72. 1968.

[11] Wolfgang Paul. Electromagnetic Traps for Charged and Neutral Particles (Nobel Lecture). *Angewandte Chemie International Edition in English*, 29(7):739–748, 1990.

[12] D Hucul, I V Inlek, G Vittorini, C Crocker, S Debnath, S M Clark, and C Monroe. Modular Entanglement of Atomic Qubits using both Photons and Phonons. *ArXiv*, 20742(July 2015):1–6, 2014.

[13] S. Debnath, N. M. Linke, C. Figgatt, K. A. Landsman, K. Wright, and C. Monroe. Demonstration of a small programmable quantum computer with atomic qubits. *Nature*, 536(7614):63–66, aug 2016.

[14] J. D. Wong-Campos, K. G. Johnson, B. Neyenhuis, J. Mizrahi, and C. Monroe. High resolution adaptive imaging of a single atom. *arXiv*, (July):1–9, 2015.

[15] J I Cirac and Peter Zoller. A scalable quantum computer with ions in an array of microtraps. *Nature*, 404(6778):579–81, 2000.

[16] C Monroe and J Kim. Scaling the Ion Trap Quantum Processor. *Science*, 339(6124):1164–1169, mar 2013.

[17] C. J. Ballance, T. P. Harty, N. M. Linke, M. A. Sepiol, and D. M. Lucas. High-Fidelity Quantum Logic Gates Using Trapped-Ion Hyperfine Qubits. *Physical Review Letters*, 117(6):060504, aug 2016.

[18] J. Zhang, P. W. Hess, A. Kyprianidis, P. Becker, A. Lee, J. Smith, G. Pagano, I.-D. Potirniche, A. C. Potter, A. Vishwanath, N. Y. Yao, and C. Monroe. Observation of a discrete time crystal. *Nature*, 543(7644):217–220, mar 2017.

[19] Fayaz Shaikh, Arkadas Ozakin, Jason M. Amini, Harley Hayden, C. S. Pai, Curtis Volin, Douglas R. Denison, Daniel Faircloth, Alexa W. Harter, and Richart E. Slusher. Monolithic Microfabricated Symmetric Ion Trap for Quantum Information Processing. *arXiv preprint arXiv: . . .*, page 911, may 2011.

[20] Fayaz A. Shaikh and Arkadas Ozakin. Stability analysis of ion motion in asymmetric planar ion traps. *Journal of Applied Physics*, 112(7):074904, oct 2012.

[21] J. Chiaverini, R. B. Blakestad, J. Britton, J. D. Jost, C. Langer, D. Leibfried, R. Ozeri, and D. J. Wineland. Surface-Electrode Architecture for Ion-Trap Quantum Information Processing. *Quantum Information and Computation*, 5(6):419–439, 2005.

[22] Emily Mount, So-Young Baek, Matthew Blain, Daniel Stick, Daniel Gaultney, Stephen Crain, Rachel Noek, Taehyun Kim, Peter Maunz, and Jungsang Kim. Single qubit manipulation in a microfabricated surface electrode ion trap. *New Journal of Physics*, 15(9):093018, sep 2013.

[23] J. True Merrill, Curtis Volin, David Landgren, Jason M. Amini, Kenneth Wright, S. Charles Doret, C. S. Pai, Harley Hayden, Tyler Killian, Daniel Faircloth, Kenneth R. Brown, Alexa W. Harter, and Richart E. Slusher. Demonstration of integrated microscale optics in surface-electrode ion traps. *New Journal of Physics*, 13, 2011.

[24] Andre Van Rynbach, Peter Maunz, and Jungsang Kim. An integrated mirror and surface ion trap with a tunable trap location. *Applied Physics Letters*, 109(22):221108, nov 2016.

[25] Erik W. Streed, Benjamin G. Norton, Andreas Jechow, Till J. Weinhold, and David Kielpinski. Imaging of Trapped Ions with a Microfabricated Optic for Quantum Information Processing. *Physical Review Letters*, 106(1):010502, jan 2011.

[26] D L Moehring, C Highstrete, D Stick, K M Fortier, R Haltli, C Tigges, and M G Blain. Design, fabrication and experimental demonstration of junction surface ion traps. *New Journal of Physics*, 13:75018.

[27] Kenneth Wright, Jason M. Amini, Daniel L. Faircloth, Curtis Volin, S. Charles Doret, Harley Hayden, C. S. Pai, David W. Landgren, Douglas Denison, Tyler Killian, Richart E. Slusher, and Alexa W. Harter. Reliable transport through a microfabricated X-junction surface-electrode ion trap. *New Journal of Physics*, 15, 2013.

[28] C. M. Shappert, J. T. Merrill, K. R. Brown, J. M. Amini, C. Volin, S. C. Doret, H. Hayden, C. S. Pai, K. R. Brown, and A. W. Harter. Spatially uniform single-qubit gate operations with near-field microwaves and composite pulse compensation. *New Journal of Physics*, 15, 2013.

[29] L. Deslauriers, S. Olmschenk, D. Stick, W. K. Hensinger, J. Sterk, and C. Monroe. Scaling and Suppression of Anomalous Heating in Ion Traps. *Physical Review Letters*, 97(10):103007, sep 2006.

[30] D F V James. Quantum dynamics of cold trapped ions with application to quantum computation. *Applied Physics B: Lasers and Optics*, 66(2):20, 1997.

[31] S. Olmschenk, K. C. Younge, D. L. Moehring, D. N. Matsukevich, P. Maunz, and C. Monroe. Manipulation and detection of a trapped Yb+ hyperfine qubit. *Physical Review A - Atomic, Molecular, and Optical Physics*, 76(5):1–9, 2007.

[32] Ye Wang, Mark Um, Junhua Zhang, Shuoming An, Ming Lyu, Jing Ning Zhang, L. M. Duan, Dahyun Yum, and Kihwan Kim. Single-qubit quantum memory exceeding 10-minute coherence time. pages 1–6, jan 2017.

[33] S. Olmschenk, D. Hayes, D. N. Matsukevich, P. Maunz, D. L. Moehring, K. C. Younge, and C. Monroe. Measurement of the lifetime of the 6p 2P1/2 level of Yb+. *Physical Review A*, 80(2):022502, aug 2009.

[34] Chr Balzer, A. Braun, T. Hannemann, Chr Paape, M. Ettler, W. Neuhauser, and Chr Wunderlich. Electrodynamically trapped Yb+ ions for quantum information processing. *Physical Review A - Atomic, Molecular, and Optical Physics*, 73(4):2–5, 2006.

[35] Harold J. Metcalf and Peter van der Straten. *Laser Cooling and Trapping*, volume 20 of *Graduate Texts in Contemporary Physics*. Springer New York, New York, NY, 1999.

[36] Christopher Foot. *Atomic Physics*, volume 1. Oxford University Press, 1 edition, 2005.

[37] D. J. Berkeland and M. G. Boshier. Destabilization of dark states and optical spectroscopy in Zeeman-degenerate atomic systems. *Physical Review A*, 65(3):033413, 2002.

[38] Eric D. Black. An introduction to PoundDreverHall laser frequency stabilization. *American Journal of Physics*, 69(1):79–87, jan 2001.

[39] P. C. Haljan, K.-A. Brickman, L. Deslauriers, P. J. Lee, and C. Monroe. Spin-Dependent Forces on Trapped Ions for Phase-Stable Quantum Gates and Entangled States of Spin and Motion. *Physical Review Letters*, 94(15):153602, apr 2005.

[40] J. True Merrill, S. Charles Doret, Grahame Vittorini, J. P. Addison, and Kenneth R. Brown. Transformed composite sequences for improved qubit addressing. *Physical Review A - Atomic, Molecular, and Optical Physics*, 90(4):2–5, 2014.

[41] Stephen Butterworth. On the theory of filter amplifiers. *Experimental Wireless and the Wireless Engineer*, 7:536–541, 1930.

[42] A. Zverev and H. Blinchikoff. Realization of a filter with helical components. *Component Parts, IRE Transactions on*, 8(3):99–110, 1961.

[43] K. G. Johnson, J. D. Wong-Campos, A. Restelli, K. A. Landsman, B. Neyenhuis, J. Mizrahi, and C. Monroe. Active stabilization of ion trap radiofrequency potentials. *Review of Scientific Instruments*, 87(5), 2016.

[44] D. Hayes, D. N. Matsukevich, P. Maunz, D. Hucul, Q. Quraishi, S. Olmschenk, W. Campbell, J. Mizrahi, C. Senko, and C. Monroe. Entanglement of Atomic Qubits Using an Optical Frequency Comb. *Physical Review Letters*, 104(14):140501, apr 2010.

[45] Emily Mount, Daniel Gaultney, Geert Vrijsen, Michael Adams, So-Young Baek, Kai Hudek, Louis Isabella, Stephen Crain, Andre van Rynbach, Peter Maunz, and Jungsang Kim. Scalable digital hardware for a trapped ion quantum computer. *Quantum Information Processing*, 15(12):5281–5298, dec 2016.

[46] Emily Mount, Chingiz Kabytayev, Stephen Crain, Robin Harper, So-Young Baek, Geert Vrijsen, Steven T. Flammia, Kenneth R. Brown, Peter Maunz, and Jungsang Kim. Error compensation of single-qubit gates in a surface-electrode ion trap using composite pulses. *Physical Review A*, 92(6):060301, dec 2015.

[47] Dmitry Budker, Derek F Kimball, and David P Demille. *Atomic Physics: An Exploration Through Problems and Solutions*. Oxford University Press, 2nd editio edition, 2008.

[48] Anirban DasGupta, T Tony Cai, and Lawrence D Brown. Interval Estimation for a Binomial Proportion. *Statistical Science*, 16(2):101–133, may 2001.

[49] Shuoming An, Jing-Ning Zhang, Mark Um, Dingshun Lv, Yao Lu, Junhua Zhang, Zhang-Qi Yin, H. T. Quan, and Kihwan Kim. Experimental test of the quantum Jarzynski equality with a trapped-ion system. *Nature Physics*, 11(2):193–199, 2014.

[50] Nikolay V. Vitanov, Andon A. Rangelov, Bruce W. Shore, and Klaas Bergmann. Stimulated Raman adiabatic passage in physics, chemistry, and beyond. *Reviews of Modern Physics*, 89(1):015006, mar 2017.

[51] D Porras and J I Cirac. Bose-Einstein Condensation and Strong-Correlation Behavior of Phonons in Ion Traps. *Physical Review Letters*, 93(26):263602, dec 2004.

[52] Chao Shen, Zhen Zhang, and L.-M. Duan. Scalable Implementation of Boson Sampling with Trapped Ions. *Physical Review Letters*, 112(5):050504, feb 2014.

[53] X.-L. Deng, D. Porras, and J. I. Cirac. Quantum phases of interacting phonons in ion traps. *Physical Review A*, 77(3):033403, mar 2008.

[54] Daniel Grier and Luke Schaeffer. New Hardness Results for the Permanent Using Linear Optics. (1122374):1–28, 2016.

[55] Sheng-Tao Wang and Lu-Ming Duan. Certification of boson sampling devices with coarse-grained measurements. *arXiv:1601.02627*, 2016.

[56] Bryan T Gard, Keith R Motes, Jonathan P Olson, Peter P Rohde, and Jonathan P Dowling. An Introduction to Boson-Sampling. In *From Atomic to Mesoscale*, pages 167–192. WORLD SCIENTIFIC, aug 2015.

[57] D. A. Hite, K. S. McKay, S. Kotler, D. Leibfried, D. J. Wineland, and D. P. Pappas. Measurements of trapped-ion heating rates with exchangeable surfaces in close proximity. *MRS Advances*, 80305:1–9, jan 2017.

[58] Philipp Schindler, Dylan J. Gorman, Nikos Daniilidis, and Hartmut Häffner. Polarization of electric-field noise near metallic surfaces. *Physical Review A*, 92(1):013414, jul 2015.

[59] I. Talukdar, D. J. Gorman, N. Daniilidis, P. Schindler, S. Ebadi, H. Kaufmann, T. Zhang, and H. Häffner. Implications of surface noise for the motional coherence of trapped ions. *Physical Review A*, 93(4):043415, apr 2016.

[60] E. Kim, A. Safavi-Naini, D. A. Hite, K. S. McKay, D. P. Pappas, P. F. Weck, and H. R. Sadeghpour. Electric-field noise from carbon-adatom diffusion on a Au(110) surface: First-principles calculations and experiments. *Physical Review A*, 95(3):033407, mar 2017.

[61] Grahame Vittorini, Kenneth Wright, Kenneth R. Brown, Alexa W. Harter, and S. Charles Doret. Modular cryostat for ion trapping with surface-electrode ion traps. *Review of Scientific Instruments*, 84(4), 2013.

[62] J. Chiaverini and J. M. Sage. Insensitivity of the rate of ion motional heating to trap-electrode material over a large temperature range. *Physical Review A*, 89(1):012318, jan 2014.

[63] C. D. Bruzewicz, J. M. Sage, and J. Chiaverini. Measurement of ion motional heating rates over a range of trap frequencies and temperatures. *Physical Review A*, 91(4):041402, apr 2015.

[64] Emily Mount, So-Young Baek, Matthew Blain, Daniel Stick, Daniel Gaultney, Stephen Crain, Rachel Noek, Taehyun Kim, Peter Maunz, and Jungsang Kim. Single qubit manipulation in a microfabricated surface electrode ion trap. *New Journal of Physics*, 15(9):093018, sep 2013.

[65] Kenneth R. Brown, Aram W. Harrow, and Isaac L. Chuang. Arbitrarily accurate composite pulse sequences. *Physical Review A*, 70(5):052318, nov 2004.

[66] Nikolay V. Vitanov. Arbitrarily accurate narrowband composite pulse sequences. *Physical Review A - Atomic, Molecular, and Optical Physics*, 84(6):14–17, 2011.

[67] Shuoming An, Dingshun Lv, Adolfo del Campo, and Kihwan Kim. Shortcuts to adiabaticity by counterdiabatic driving for trapped-ion displacement in phase space. *Nature Communications*, 7:12999, 2016.

[68] C. K. Hong, Z. Y. Ou, and L. Mandel. Measurement of subpicosecond time intervals between two photons by interference. *Physical Review Letters*, 59(18):2044–2046, nov 1987.

[69] N. J. Cerf, C. Adami, and P. G. Kwiat. Optical simulation of quantum logic. *Physical Review A*, 57(3):R1477–R1480, mar 1998.

[70] Rodney Loudon. *Quantum Theory of Light.* Oxford University Press, 2000.

[71] M Gessner, M Ramm, T Pruttivarasin, A Buchleitner, H-P Breuer, and H Häffner. Local detection of quantum correlations with a single trapped ion. *Nature Physics*, 10(2):105–109, dec 2013.

[72] Dylan J. Gorman, Philipp Schindler, Sankaranarayanan Selvarajan, Nikos Daniilidis, and Hartmut Häffner. Two-mode coupling in a single-ion oscillator via parametric resonance. *Physical Review A*, 89(6):062332, jun 2014.

[73] Shiqian Ding, Gleb Maslennikov, Roland Hablutzel, Huanqian Loh, and Dzmitry Matsukevich. A quantum parametric oscillator with trapped ions. *arXiv*, pages 1–6, dec 2015.

[74] Shiqian Ding, Gleb Maslennikov, Roland Hablutzel, and Dzmitry Matsukevich. Cross-Kerr nonlinearity for phonon counting. *Arxiv*, pages 1–5, mar 2017.

[75] Kenji Toyoda, Ryoto Hiji, Atsushi Noguchi, and Shinji Urabe. HongOuMandel interference of two phonons in trapped ions. *Nature*, 527(7576):74–77, 2015.

[76] Hoi Kwan Lau and Daniel F V James. Proposal for a scalable universal bosonic simulator using individually trapped ions. *Physical Review A - Atomic, Molecular, and Optical Physics*, 85(6):1–11, 2012.

[77] W J Riley. Handbook of Frequency Stability Analysis. *NIST Special Publication*, 1065, feb 2008.

[78] Scott Aaronson and Alex Arkhipov. The computational complexity of linear optics. In *Proceedings of the 43rd annual ACM symposium on Theory of computing - STOC '11*, page 333, New York, New York, USA, 2011. ACM Press.

[79] E. W. Streed, T. J. Weinhold, and D. Kielpinski. Frequency stabilization of an ultraviolet laser to ions in a discharge. *Applied Physics Letters*, 93(7):5–8, 2008.

[80] S. C. Burd, P. J. W. du Toit, and Hermann Uys. Coupled optical resonance laser locking. *Optics Express*, 22(21):25043, oct 2014.

[81] Michael W Lee, Marie Claire Jarratt, Christian Marciniak, and Michael J Biercuk. Frequency Stabilization of a 369 nm Diode Laser by Nonlinear Spectroscopy of Ytterbium Ions in a Discharge. *ArXiv*, 759(2006):757–759, 2014.

[82] C P Pearman, C S Adams, S G Cox, P F Griffin, D A Smith, and I G Hughes. Polarization spectroscopy of a closed atomic transition: applications to laser frequency locking. *Journal of Physics B: Atomic and Molecular Physics*, 35(02):5141–5151, 2002.

[83] W. Z. Zhao, J. E. Simsarian, L. A. Orozco, and G. D. Sprouse. A computer-based digital feedback control of frequency drift of multiple lasers. *Review of Scientific Instruments*, 69(11):3737–3740, nov 1998.

[84] S. Uetake, K. Matsubara, H. Ito, K. Hayasaka, and M. Hosokawa. Frequency stability measurement of a transfer-cavity-stabilized diode laser by using an optical frequency comb. *Applied Physics B: Lasers and Optics*, 97(2):413–419, 2009.

[85] R. W. P. Drever, J. L. Hall, F. V. Kowalski, J. Hough, G. M. Ford, A. J. Munley, and H. Ward. Laser phase and frequency stabilization using an optical resonator. *Applied Physics B Photophysics and Laser Chemistry*, 31(2):97–105, jun 1983.

[86] Hui Wang, Yu-Ming He, Yu-Huai Li, Zu-en Su, Bo Li, He-liang Huang, Xing Ding, Ming-cheng Chen, Chang Liu, Jian Qin, Jin-peng Li, Yu-Ming He, Christian Schneider, Martin Kamp, Cheng-Zhi Peng, Sven Hoefling, Chao-Yang Lu, and Jian-Wei Pan. Multi-photon boson-sampling machines beating early classical computers. *ArXiv*, dec 2016.

[87] J. B. Spring, B. J. Metcalf, P. C. Humphreys, W. S. Kolthammer, X.-M. Jin, M. Barbieri, A. Datta, N. Thomas-Peter, N. K. Langford, D. Kundys, J. C. Gates, B. J. Smith, P. G. R. Smith, and I. A. Walmsley. Boson Sampling on a Photonic Chip. *Science*, 339(6121):798–801, feb 2013.

[88] Bryan T. Gard, Jonathan P. Olson, Robert M. Cross, Moochan B. Kim, Hwang Lee, and Jonathan P. Dowling. Inefficiency of classically simulating linear optical quantum computing with Fock-state inputs. *Physical Review A*, 89(2):022328, feb 2014.

[89] Scott Aaronson and Alex Arkhipov. BosonSampling Is Far From Uniform. sep 2013.

[90] Kai Liu, Austin Peter Lund, YongJian Gu, and Timothy Cameron Ralph. A certification scheme for the boson sampler. *Journal of the Optical Society of America B*, 33(9):1835, 2016.